UNIVERSITÀ DEGLI STUDI DI PAVIA

SCIENTIFICA ACTA

QUADERNI DEL DOTTORATO

VOLUME XVI ANNO XVI NUMERO 1

15 MARZO 2001

ISTITUTO NAZIONALE DI FISICA NUCLEARE

CENTRO STAMPA – DIPARTIMENTI FISICI
Via Bassi, 6 27100 Pavia

EDITORIALE

Il Dottorato di Ricerca in Fisica della Universita' di Pavia e' stato "internazionalizzato" dal Ministero per la Universita' e per la Ricerca Scientifica e Tecnologica (MURST).

A partire dall'Anno Accademico 2000/2001 sono state attivate convenzioni bilaterali con:

1- l'Universita' del Colorado, Boulder (Colorado);
2- l'Universita' dello Stato dell'Iowa, Ames (Iowa);
3- l' Universita' Jagiellonian di Cracovia (Polonia)
4- l'Universita' della Stato di Washington, Seattle (Washington).

Pertanto, a partire dal prossimo numero, la lingua ufficiale della rivista diventa la lingua inglese e la rivista assume una nuova numerazione. La stessa viene cosi' aperta al contriubuto da tutte le Istituzioni partecipanti; il Direttore viene affiancato da un comitato di direzione con rappresentanza degli Atenei inseriti nel progetto

EDITORIAL

The Graduate School in Physics of the University of Pavia has been given the status of "International School" by the Ministry for the University and the Scientific and Technological Research (MURST).

Starting with the Academic Year 2000/2001, bilateral agreements of collaboration have been activated with:

1- the University of Colorado at Boulder (Colorado);
2- the Iowa State University, Ames (Iowa);
3- the Jagiellonian University, Krakow (Poland);
4- the University of Washington, Seattle (Washington).

Thus, with the next issue, the official language of the journal will be english and the journal itself will assume a new numbering sequence. The latter will be open to contributions from all participating Institutions; the Director will be sided by an Editorial Board representing the Universities inserted into the project.

Il Direttore
Sergio P. Ratti

INDICE

1 - MAGNETIC CORRELATIONS AND SPIN DYNAMICS IN PURE AND DOPED HALDANE CHAINS: ^{89}Y NMR IN $Y_{2-y}Ca_yBaNi_{1-x}Mg_xO_5$ – F. Tedoldi pag. 1

2 - A FACILITY FOR THE STUDY OF PARTICLE-INDUCED INFRARED EMISSION IN NOBLE GASES – D. Iannuzzi pag. 93

Magnetic correlations and spin dynamics in pure and doped Haldane chains: ^{89}Y NMR in $Y_{2-y}Ca_yBaNi_{1-x}Mg_xO_5$

FABIO TEDOLDI

Department of Physics "A. Volta", Unita' INFM di Pavia-Via Bassi, 6 - 27100-I Pavia, Italy

Seminario tenuto il 14/01/2000 per il conseguimento del titolo di Dottore di Ricerca in Fisica

A Roberto, collega ed amico.

Table of contents

Introduction and overview 5

1 Quantum magnetism and AF spin chains 9
- 1.1 Transition metal oxides: from correlated electrons to a spin-only hamiltonian . . . 10
- 1.2 Magnetic hamiltonians . . . 13
- 1.3 Correlation, order and dimensionality . . . 14
- 1.4 Antiferromagnetic spin chains . . . 16
  - 1.4.1 Quantum disorder . . . 17
  - 1.4.2 Half-integer spins and integer spins: from Bethe ansatz to Haldane conjecture . . . 19
  - 1.4.3 Experimental evidences of a quantum spin gap in $S = 1$ compounds . . . 21
- 1.5 Spin liquids and doping . . . 22

2 Probing magnetic correlations by NMR 25
- 2.1 Hyperfine interactions in solids: basic aspects . . . 26
- 2.2 Local fields and NMR spectra . . . 27
- 2.3 Nuclear relaxation times . . . 29

3 ^{89}Y NMR study of the Haldane chain Y_2BaNiO_5 33
- 3.1 Structural and electronic properties . . . 34
- 3.2 Experimental results . . . 36
  - 3.2.1 Magnetic susceptibility . . . 36
  - 3.2.2 ^{89}Y NMR spectra . . . 38
  - 3.2.3 Spin-lattice relaxation rates . . . 40
- 3.3 Hyperfine coupling and NMR lineshape . . . 41
- 3.4 Haldane gap from ^{89}Y NMR shift . . . 45
- 3.5 Spin dynamics from ^{89}Y nuclear relaxation . . . 46

4 Staggered magnetization from spinless impurities: an imaging in $Y_2BaNi_{1-x}Mg_xO_5$ **53**
4.1 Finite $S = 1$ AF chains: basic theoretical aspects . 54
4.2 Nonmagnetic-impurity doping in Y_2BaNiO_5 58
4.3 Experimental results 59
4.3.1 Magnetic susceptibility 59
4.3.2 ^{89}Y NMR spectra 61
4.4 Local magnetization, edge spins and magnetic correlations 65
4.5 Models for "intermediate temperature": preliminary results 71
4.6 ^{89}Y NMR in $Y_2BaNi_{1-x}Mg_xO_5$ *vis a vis* to similar experiments 72

5 The hole-doped spin liquid $Y_{2-y}Ca_yBaNiO_5$ **73**
5.1 Introduction 74
5.2 Experimental results 75
5.3 Analysis and discussion 78

Appendix. Preparation and characterization of Y_2BaNiO_5-based samples **83**

Bibliography **85**

Acknowledgements **91**

Introduction and overview

Magnetism is certainly one of the most intriguing subjects in condensed matter physics. On one side important applications (such as storing of information) stimulate the interest of technology, on the other the strict quantum origins and the many-body character of microscopic magnetic phenomena are the realm of fundamental research.

The present work deals with some basic aspects of *one-dimensional Heisenberg quantum spin systems with antiferromagnetic interactions* (in the following $1D$-HAF's or HAF chains). According to quantum mechanical description, Heisenberg spins can never assume, not even at $T = 0$, a perfect antiparallel configuration, contrary to what expected from a classical analysis. This property becomes more evident as lower is the dimensionality of the exchange interaction and in $1D$ it is so dramatic that AF order is prevented at any temperature. But while for half-integer spins the ground state of the chain is "quasi-long-range ordered" (i.e., the magnetic correlation spatially decays according to a power law), integer spin chains are really "disordered" (the correlation decays exponentially), even at $T = 0$. Such surprising difference, predicted by Haldane in 1983 [Haldane 83], is nowadays strongly supported by numerical calculations and experimental results. However an exhaustive description of $1D$-HAF's, concerning finite temperature correlations, spin dynamics and doping-induced effects is far from being available.

With the aim of clarifying some of the main points of this subject, I have studied the spin-1 compound Y_2BaNiO_5, by ^{89}Y NMR and magnetic susceptibility. Y_2BaNiO_5 contains well separated chains of corner linked NiO_6 octahedra. The Ni^{2+} ($S = 1$) ions located in the centers of these octahedra strongly AF-interact along the chain axis, while coupling between different chains is almost

negligible. The marked one-dimensionality, together with the strong isotropy of the interaction makes of Y_2BaNiO_5 a prototype $S = 1$ $1D$-HAF. Moreover, ^{89}Y nuclei are ideal probes, naturally contained in this nickelate, which allows one to measure by resonance techniques internal fields and spin fluctuations.

In Y_2BaNiO_5 one can perform heterospin (Mg^{2+} ($S = 0$) $\rightarrow$ Ni^{2+}) and heterovalent ($Ca^{2+} \rightarrow Y^{3+}$) substitutions and investigate the modification in the magnetic properties of the system upon spin and charge doping. A partial substitution of magnetic ions for spinless ones is expected to induce, locally, non-zero staggered moments. By ^{89}Y NMR spectra the problem has been addressed in $Y_2BaNi_{1-x}Mg_xO_5$, looking for experimental evidence of modulated magnetization around Mg^{2+} impurities. The spin dynamics of hole-doped Y_2BaNiO_5 has been studied through nuclear relaxation. It is well known that injection of holes in a quasi-bidimensional AF matrix of Cu^{2+} ions leads to high-T_c superconductivity. The comprehension of this phenomenon still requires clarification of some important points, among those the motion of the charge-carriers in the normal phase, where strong local correlations survive. However the direct approach of the problem in high-T_c cuprates is complicated by the fact that one has to deal, simultaneously, with doping-induced magnetic disorder, holes-itinerancy and tendency to form Cooper-pair. The study of the dynamics of the holes is more easily addressed in systems where magnetic disorder occurs independently on the presence of doped-charge and no pairing effects are observed.

The manuscript is organized in five chapters.

In the first one some basic aspects of quantum magnetism are recalled. After having analyzed the origin of the exchange interaction and the role of dimensionality, the attention is focused on AF spin chains. The concept of "quantum disorder" is introduced, starting from the breakdown of the semi-classical spin-wave theory in $1D$. The Haldane's conjecture is discussed in the light of the experimental findings in quasi-$1D$ compounds. The problem of doping is illustrated in the context of quantum disordered systems.

Nuclear magnetic resonance (NMR) concepts are presented in Chapter 2, emphasizing the efficiency of this technique in probing

static and dynamic correlations. It is shown how the distribution of local fields revealed by the NMR spectra is connected to the expectation value of the electronic spin and how the nuclear relaxation rates provide information on the spin dynamics of the system.

In Chapter 3 the results obtained by magnetic susceptibility and ^{89}Y NMR in Y_2BaNiO_5 are reported. The value of the Haldane gap ($\Delta_H = 102K$), extracted from the temperature behavior of the NMR shift, is in agreement with the one deduced from inelastic neutron scattering. The low-energy spin dynamics, probed by ^{89}Y nuclear relaxation, is discussed in terms of multimagnon processes.

An ^{89}Y NMR study of the site-magnetization in Y_2BaNiO_5 doped by non-magnetic impurities (Mg^{2+}) is described in Chapter 4. A correspondence between resolved resonance lines in the ^{89}Y spectra and lattice positions is established, providing an image of the alternating magnetic moments which develop around the spinless-ions. The spatial modulation of these anomalous moments is shown to reflect the spin-spin correlation functions of the infinite chain. Comparisons with theories, numerical simulations and other experimental results are addressed.

Finally, in Chapter 5, the spin dynamics in hole-doped chain $Y_{2-y}Ca_yBaNiO_5$ is studied by ^{89}Y nuclear relaxation, showing that low-energy spin fluctuations are induced by the heterovalent substitution $Ca^{2+} \rightarrow Y^{3+}$. A phenomenological picture consistent with the experimental findings from spin-lattice and spin-spin relaxation rates and from magnetic susceptibility is discussed.

Chapter 1

Quantum magnetism and AF spin chains

Although spontaneous magnetism is one of the most manifest phenomena in condensed matter, a satisfactory explanation of its origin has been found only after the development of quantum mechanics. Maxwell electromagnetism in fact, cannot catch the real nature of magnetic cooperative phenomena, as it is easily proved by comparing the magnitude of "classical" dipolar interaction between electron moments (about 10^{-5}eV) to the magnetic transition temperatures ($10^2 - 10^3 K$ in transition metal and rare earth compounds, corresponding to energies around $10^{-2} - 10^{-1}$eV). The mechanism giving rise to magnetism in matter originates from Coulomb repulsion between electrons and from the requirement of antisymmetric wavefunctions (Pauli exclusion principle). In this Chapter, this topic is recalled with direct application to transition metal oxides. In a wide class of such compounds, electron-electron correlation induces insulating behavior and leads to low-energy properties that can be often described by effective spin-hamiltonians having a dominant antiferromagnetic (AF) character. The role played by the dimensionality of the magnetic interaction is analyzed in order to emphasize how, in one-dimensional AF systems, peculiar quantum phenomena occur, such as the absence of long-range order at $T = 0$ and the dramatic difference in the behavior of integer and half-integer spin chains. Theoretical predictions and experimental findings obtained in quasi-1D $S = 1$ compounds are discussed and the effects of doping is briefly addressed.

1.1 Transition metal oxides: from correlated electrons to a spin-only hamiltonian

Transition metal oxides (TMO's) have been object, in the last decades, of a great deal of interest, particularly because hole-doping of some of these compounds leads to high-T_c superconductivity [Bednorz 86]. On the other hand, the intrinsic electronic properties of TMO's are, themselves, a very rich field, in which many puzzling magnetic phenomena find their origin.

The key role in the physics of TMO's is played by the on-site Coulomb interaction, which is not negligible for $3d$ electrons, and which can even drive them to behaviors very different from the one expected in the framework of Bloch band theory (based on one-electron approximation). The effects of electron-electron correlation will be illustrated by first referring to NiO. Besides being a prototype of TM-salt, NiO is also the "magnetic ingredient" of many $S = 1$ compounds. A preliminary description of its basic properties will be useful for the analysis of the phenomena occurring in the chains studied in the present work.

In the ionic model picture NiO is written $Ni^{2+}O^{2-}$, with nickel-

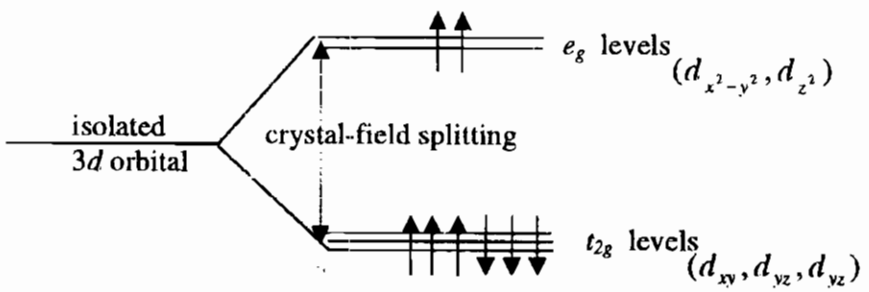

Figure 1.1: Energy levels and spin states for a $3d^8$ ion in a cubic crystalline field.

ion in the configuration (Ar)$3d^8$ and oxygen in the $1s^2 2s^2 2p^6$ one. The large overlap between $2p$ oxygen wavefunctions generates a broad $2p$-band, which does not contribute to the electric conduction because it is filled. As a consequence of the cubic symmetry of the crystal field, the Ni $3d$-orbitals are split in two groups of levels: the one with lower energy has t_{2g} symmetry and arranges six-electrons, while two-electrons occupy the e_g-orbitals at higher energy (Fig. 1.1). According to Hund's rule these last two electrons have aligned spins, and Ni^{2+} is a $S = 1$ magnetic ion. The band generated by the e_g-orbitals is half-filled and in a simple one-electron theory, NiO should be a metal, while actually it behaves as a good insulator.

The breakdown of the one-electron approximation is due to the fact that intra-atomic Coulomb repulsion U_{dd} between the Ni-$3d$ electrons is stronger than their delocalization energy ($3d$ bandwidth), thus suppressing the charge fluctuations occurring in metals [Mott 49, Hubbard 64] . Actually, in NiO as in others TMO's , U_{dd} is even bigger than the energy Δ required to transfer one electron from the ligand to the transition metal (Fig. 1.2). The conduction phenomena are thus controlled by an energy gap $\approx \Delta$ and the compounds classified as charge-transfer insulator.

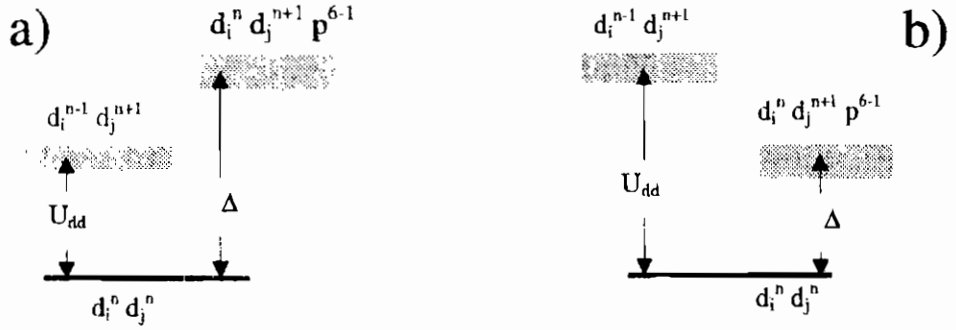

Figure 1.2: Energy level diagram showing the ground state and the lowest lying excitations for: **a)** Mott-Hubbard insulators; **b)** charge-transfer insulators [Zaanen 85, Sawatzky 90]. U_{dd} represents the energy required to move one d-electron from the site i to the site j, while Δ is the energy needed to transfer one electron from an oxygen ion ($p^6 \rightarrow p^{6-1}$) to the site j.

Suppression of charge fluctuations is the base for a description of the low-energy properties of magnetic insulator in terms of spin-only hamiltonians. This aspect was first addressed by Anderson [Anderson 59], for the case $U_{dd} << \Delta$ (Mott-Hubbard insulators). He observed that whenever the Coulomb on-site repulsion U_{dd} predominates, preventing metallic conduction, the opposite tendency of the electrons to delocalize causes an effective antiferromagnetic interaction. Antiparallel electrons can in fact gain energy by spreading into non-orthogonal overlapping orbitals, where parallel electrons can not. In perturbation theory this corresponds to an effective transfer interaction b connecting virtual excitations of the kind $d^n d^n \rightarrow d^{n+1} d^{n-1}$ (at an energy U_{dd} above the ground state) to the ground-state wavefunction, leading to an exchange coupling between spins on the TM ions (superexchange), of magnitude $J = 2b^2/U$. Zaanen and Sawatzky [Zaanen 87] have extended Anderson's theory to include charge-transfer insulator ($U_{dd} > \Delta$), obtaining for the superexchange coupling constant

$$J = 2b^2 \left(\frac{1}{U_{dd}} + \frac{1}{\Delta} \right) . \tag{1.1}$$

Anderson also pointed out that the most efficient superexchange path involves the anion between two TM ions [Anderson 63]. The transfer energy b is thus proportional to the TM-O-TM orbitals-overlapping and turns out to be maximum for TM-O-TM angles close to π. Away from this condition other effects become important in driving the magnetic behavior of TMO's [Mott], first of all *direct* (ferromagnetic) exchange between electrons on neighbor ions (i.e. inter-site Coulomb repulsion). Moreover, an effective ferromagnetic interaction can also occur in those situations where the highest occupied $3d$-band is completely filled. In such a kind of electronic configuration in fact, allowed by a break-down of the Hund's rule due to crystal field, the virtual hopping between adjacent sites takes place in empty orbitals and is thus favored if the spins involved are aligned [Anderson 59].

This introductory overview on TMO's can be summarized by saying that each time the Coulomb repulsion between electrons dominates on the delocalization energy, the low-energy dynamics of the system can be described in terms of a magnetic hamiltonian. Depending on the particular compound, the character of the magnetic interactions can be ferromagnetic or antiferromagnetic.

Quantitative comparison between the above mentioned exchange mechanisms [Anderson 59] shows that antiferromagnetism usually dominates. Actually only a few insulating TMO's are ferromagnetic.

1.2 Magnetic hamiltonians

As recalled in the previous Section, a suitable basis to derive the main properties of magnetic systems is the Heisenberg exchange hamiltonian

$$\mathcal{H} = \sum_{i,j} J_{ij} \vec{S}_i \cdot \vec{S}_j \tag{1.2}$$

where $\vec{S}_i$ and $\vec{S}_j$ are quantum spins, namely

$$[S^\alpha \; S^\beta] = i\epsilon^{\alpha\beta\gamma} S^\gamma \qquad S^2 = s(s+1)\,, \tag{1.3}$$

localized at the sites i, j. The coupling constant J_{ij} keeps track of the details of the electronic problem, and can describe ferromagnetic ($J_{ij} \leq 0$) or antiferromagnetic ($J_{ij} \geq 0$) interactions.

Since exchange interaction requires spatial overlapping of the atomic wavefunctions, Eq. (1.2) is usually dominated by nearest-neighbor (nn) terms, thus reducing to the form

$$\mathcal{H}_{ex} = J \sum_{<i,j>} \vec{S}_i \cdot \vec{S}_j \tag{1.4}$$

where $< i, j >$ indicates a pair of nn sites on some regular, d-dimensional lattice. The Heisenberg hamiltonian (1.4) is SO(3)-invariant, and hence commutes with the total spin $\mathcal{S}^2 = (\sum_i \vec{S}_i)^2$ and with its z-component $\mathcal{S}^z = \sum_i \vec{S}_i^z$ [Kittel]. The eigenvalues of $\mathcal{S}^2$ and $\mathcal{S}^z$ are thus good quantum numbers for the eigenstates of $\mathcal{H}_{ex}$.

A description given only in terms of exchange hamiltonians of the type (1.2) and (1.4) disregards the role played by the orbital moment through the spin-orbit coupling. This effect is usually small for TMO's and can be taken into account perturbatively, by adding to $\mathcal{H}_{ex}$ one or more single-ion anisotropy terms of the form

$$\mathcal{H}_D^\alpha = D^\alpha \sum_i (S_i^\alpha)^2 \,. \tag{1.5}$$

When the magnetic anisotropy is *uniaxial* ($\mathcal{H}_D = D\sum_i (S_i^z)^2$), the symmetry of the total interaction $\mathcal{H}_e = \mathcal{H}_{ex} + \mathcal{H}_D$ is lowered to SO(2) and the degeneracy between spin-multiplets typical of SO(3)-invariant systems partially removed.

1.3 Correlation, order and dimensionality

Despite its simple appearance, the magnetic hamiltonian (1.4) can hardly be solved to obtain eigenstates and eigenvalues. Exact calculations have been successfully performed only in a few cases. Due to the many-body character of the exchange interaction, even perturbative approaches are often inefficient. However, a certain number of general rigorous results are available, which define the bounds of the phenomenology described by the (1.4). In particular, a neat picture of the different regions of the space (J, T, d, S) in which magnetic order can/cannot occur can be given.

In general, the order properties of a macroscopic magnetic system ($\mathcal{H}_e$) are classified on the base of the pair correlation function

$$\langle \vec{S}_i \cdot \vec{S}_j \rangle \equiv \lim_{\mathcal{N}\to\infty} \frac{1}{\mathcal{N}\mathcal{Z}} Tr[e^{-\frac{\mathcal{H}_e}{K_B T}} (\vec{S}_i \cdot \vec{S}_j)] \,, \tag{1.6}$$

where $\mathcal{N}$ is the number of sites, K_B the Boltzman constant and $\mathcal{Z} = Tr\left(e^{-\frac{\mathcal{H}_e}{K_B T}}\right)$. One has *long range order* when

$$\lim_{|\vec{x}_i - \vec{x}_j|\to\infty} \langle \vec{S}_i \cdot \vec{S}_j \rangle \neq 0 \tag{1.7}$$

(with $|\vec{x}_i - \vec{x}_j|$ = distance between sites i and j). When instead the correlations decay as a power law at long distance,

$$\lim_{|\vec{x}_i - \vec{x}_j|\to\infty} \langle \vec{S}_i \cdot \vec{S}_j \rangle \propto |\vec{x}_i - \vec{x}_j|^{-\alpha} \,, \tag{1.8}$$

the system is said to be *quasi long-range ordered.* Finally the term *disordered* is used to indicate exponential decay of the correlation, namely

$$\lim_{|\vec{x}_i - \vec{x}_j|\to\infty} \langle \vec{S}_i \cdot \vec{S}_j \rangle \propto e^{-\frac{|\vec{x}_i - \vec{x}_j|}{\xi}} \,, \tag{1.9}$$

with ξ correlation length.

It can be shown [Auerbach] that the occurrence of quasi long range order implies *spontaneously symmetry breaking* in correspondence to a given wave vector $\vec{q}$, i.e. a finite, $\vec{q}$-modulated, magnetization even when the external ordering field H is taken to zero. Formally

$$\lim_{H\to 0^+}\lim_{\mathcal{N}\to\infty}\langle S^z_{\vec{q}}\rangle \equiv \lim_{H\to 0^+}\lim_{\mathcal{N}\to\infty}\frac{1}{N\mathcal{Z}_H}Tr[e^{-\frac{\mathcal{H}_H}{K_BT}}S^z_{\vec{q}}] \neq 0 \quad , \qquad (1.10)$$

with $S^z_{\vec{q}} = \sum_i e^{i\vec{q}\cdot\vec{x}_i}S^z_i$ and $\mathcal{H}_H = \mathcal{H}_e - (\gamma_e\hbar H S^z_{\vec{q}})$. In Eq. (1.10) the partition function is calculated in presence of field, i.e. $\mathcal{Z}_H = Tr[e^{-\frac{\mathcal{H}_H}{K_BT}}]$.

The occurrence of long range order in systems described by the isotropic Heisenberg hamiltonian (1.4) is prevented at any finite temperature when $d \leq 2$ [Mermin 66]. This theorem, which follows the same approach used to prove the absence of superfluidity in one and two dimension [Hoenberg], actually holds for all the models with at least one *continuous symmetry* and *short range interaction.* The hamiltonian (1.4) belongs to this class and thus the correspondent systems can undergo a finite-temperature phase transition to an ordered state only in the $3D$-case.

Mermin and Wagner's theorem does not apply at $T = 0$, so that one could have in principle a long range ordered ground state even for $d \leq 2$. This is actually the case for $1D$ and $2D$ ferromagnets, since the *fully ferromagnetic state*

$$|\Psi_{FM}\rangle \equiv \prod_i |s_i, s_i\rangle = |s, s, ...s, ...\rangle \qquad (1.11)$$

(Fig. 1.3 a)) belongs to the ground state multiplet of the Heisenberg hamiltonian with $J < 0$. The proof of this statement consists in showing that $|\Psi_{FM}\rangle$ is an eigenstate and that it has the lowest energy. By rewriting the hamiltonian (1.4) in terms of raising and lowering spin operator $S^{\pm} \equiv S^x \pm S^y$:

$$\mathcal{H}_{ex} = J\sum_{<i,j>}[\frac{1}{2}(S^+_iS^-_j + S^-_iS^+_j) + S^z_iS^z_j] \, , \qquad (1.12)$$

it's easy to verify that

$$\mathcal{H}_{ex}|\Psi_{FM}\rangle = \frac{JzNs(s+1)}{2}|\Psi_{FM}\rangle \, , \qquad (1.13)$$

with z = number of nearest neighbors. Then, since $s(s+1) \geq \langle \vec{S}_i \cdot \vec{S}_j \rangle$, one also proves that $|\Psi_{FM}\rangle$ is associated to the lowest eigenvalue of $\mathcal{H}_{ex}$.

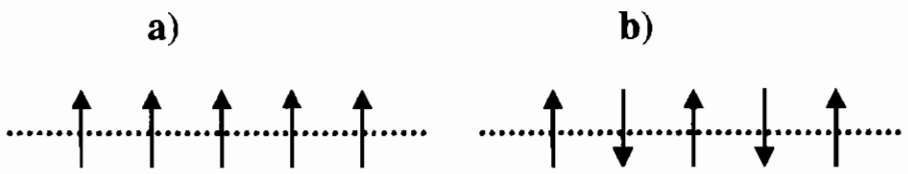

Figure 1.3: Schematic representations of: a) *fully ferromagnetic state* $\Psi_N \equiv \prod_i |s_i, s_i\rangle$; b) *classical Néel configuration* $\Psi_N \equiv \prod_i |s_i, (-1)^i s_i\rangle$.

The case of the antiferromagnets is quite different, since the *classical Néel configuration*

$$\Psi_N \equiv \prod_i |s_i, (-1)^i s_i\rangle \equiv |s, -s, ...s, -s....\rangle \qquad (1.14)$$

(Fig. 1.3 b)) is not an eigenstate of the Heisenberg hamiltonian with $J > 0$. The spin flip terms $S_i^+ S_j^-$ in the first part of the (1.4) connect in fact Ψ_N to different spin configurations. Thus, in the quantum HAF, the "ordered" moment $\langle S_i^z \rangle$ is always less than the classical value s. Nevertheless for $d = 2$ and $d = 3$ the reduction of $\langle S_i^z \rangle$ is finite at $T = 0$ (actually for $d = 3$ even at $T \neq 0$) and can be calculated by different techniques [Auerbach]. Instead, a more exotic behavior characterizes $1D$-HAF systems, as discussed in the next Section.

1.4 Antiferromagnetic spin chains

The attention is now focused on the system described by the hamiltonian (1.4) for $J > 0$ and $d = 1$, in other words to the HAF *spin chain*. It is curious to observe how this apparently simple subject (which for $S = 1/2$ has a remarkable exact solution going back to 1931 [Bethe 31]) is still today a lively field of research. The main

reason lies in the absence of spontaneously symmetry breaking in the ground state (*quantum disorder*), which makes each type of *spin-wave*-like approach [Anderson 52, Kubo 52, Mattis] unappropriated.

1.4.1 Quantum disorder

The usual way to derive the low-energy properties of the HAF's begins with the assumption that the ground state is given by Ψ_N plus *quantum fluctuations*. This corresponds a picture of zero point motion about the classical Néel configuration (1.14), due to the action of the terms $S_i^+ S_j^-$. We will see how the assumption of small fluctuations breaks down in one dimension.

The conventional approach makes use of the Holstein-Primakov transformation [Holstein 40]. The system is divided in two sublattices "A" and "B", with adjacent sites on separate sublattices. On "A" one defines

$$\begin{aligned} S_i^z &= s - a_i^\dagger a_i \\ S_i^+ &= \left(\sqrt{2s - a_i^\dagger a_i}\right) a_i \\ S_i^- &= a_i^\dagger \left(\sqrt{2s - a_i^\dagger a_i}\right) \end{aligned} \tag{1.15}$$

while on sublattice "B":

$$\begin{aligned} S_i^z &= s - b_i^\dagger b_i \\ S_i^- &= \left(\sqrt{2s - b_i^\dagger b_i}\right) b_i \\ S_i^+ &= b_i^\dagger \left(\sqrt{2s - b_i^\dagger b_i}\right) \quad , \end{aligned} \tag{1.16}$$

with a and b bosonic operators with commutation relations

$$[a^\dagger . a] = [b, b^\dagger] = 1 \ , \qquad [a, a] = [b, b] = 0 \ . \tag{1.17}$$

Eq. (1.15) and (1.16) preserve the correct spin commutation rules and the constraint given by Eq.'s (1.3). The Holstein-Primakov's

is an exact transformation and by itself can not simplify the terms of the problem. The usual approximation consists in perturb away from the limit $s \to \infty$, where quantum spins become classical and Ψ_N is the exact ground state. By expanding Eq.'s (1.15) and (1.16) to the lowest order and introducing Fourier representation for the bosonic operators,

$$o_{\vec{k}} = \frac{1}{N} \sum_i e^{i\vec{k}\cdot\vec{x}_i} o_i \qquad (o_i = a, a^\dagger, b, b^\dagger) \;, \tag{1.18}$$

the Heisenberg hamiltonian takes the form

$$\mathcal{H}_{ex} = Jsz \sum_{\vec{k}} \gamma_{\vec{k}} (a_{\vec{k}} b_{-\vec{k}} + a^\dagger_{\vec{k}} b^\dagger_{-\vec{k}} + 1) + (a^\dagger_{\vec{k}} a_{\vec{k}} + b^\dagger_{\vec{k}} b_{\vec{k}}) \tag{1.19}$$

where $\gamma_{\vec{k}} \equiv \sum_{\vec{\pi}} e^{i\vec{k}\cdot\vec{\pi}}$, z is the number of nearest neighbours and $\vec{\pi}$ is the translational vectors to the neighbouring sites. The Bogoliubov transformation

$$c_{\vec{k}} = u_{\vec{k}} a_{\vec{k}} - v_{\vec{k}} b^\dagger_{-\vec{k}} \tag{1.20}$$

$$d_{\vec{k}} = u_{\vec{k}} b_{-\vec{k}} - v_{\vec{k}} a^\dagger_{\vec{k}} \tag{1.21}$$

with the normalization constraint

$$|u|^2 - |v|^2 = 1 \tag{1.22}$$

and the condition

$$\gamma(|u|^2 + |v|^2) + 2|u||v| = 1 \tag{1.23}$$

diagonalyze Eq. (1.19), which takes the form of a non-interacting bosonic hamiltonian:

$$\mathcal{H}_{ex} = -2NzJs(s+1) + Jsz \sum_{\vec{k}} \sqrt{1 - \gamma^2_{\vec{k}}} \, (c^\dagger_{\vec{k}} c_{\vec{k}} + d^\dagger_{\vec{k}} d_{\vec{k}} + 1) \;. \tag{1.24}$$

The excitations created by c and d are known as spin-waves. For $c^\dagger_{\vec{k}} c_{\vec{k}} = d^\dagger_{\vec{k}} d_{\vec{k}} = 0$ one has the zero-point energy of the HAF (in the semi-classical limit $s \to \infty$):

$$E_0 = -2NzJs(s+1) + Jsz \sum_{\vec{k}} \sqrt{1 - \gamma^2_{\vec{k}}} \;. \tag{1.25}$$

The departure of the $T = 0$ sublattice magnetization $\langle S^z_{totA}\rangle = \sum_{i\in A}\langle S^z_i\rangle$ from the value Ns (corresponding to the Néel configuration) can be evaluated by using the inverses of the (1.20) and (1.21), obtaining [Kittel]

$$\langle S^z_{totA}\rangle = Ns - \sum_{\vec{k}}\langle a^+_{\vec{k}} a_{\vec{k}}\rangle = Ns\left(1 - \frac{1}{2Ns}\sum_{\vec{k}}\frac{1}{\sqrt{1-\gamma^2_{\vec{k}}}} - 1\right) . \tag{1.26}$$

The reduction in $\langle S^z_{totA}\rangle$ due to quantum fluctuations, in spin-waves approximation, turns out

$$\Delta\langle S^z_{totA}\rangle \equiv Ns - \langle S^z_{totA}\rangle = \frac{1}{2}\left(\sum_{\vec{k}}\frac{1}{\sqrt{1-\gamma^2_{\vec{k}}}} - 1\right) . \tag{1.27}$$

Then, in the continuous limit ($\frac{1}{N}\sum_{\vec{k}} \to \frac{1}{(2\pi)^d}\int d\vec{k}$) the ground state expectation value of the local spin operator S^z_i differs from the classical value s (or $-s$) by a factor

$$\Delta\langle S^z_i\rangle = -\frac{1}{2(2\pi)^d}\int d\vec{k}\ \left(\frac{1}{\sqrt{1-\gamma^2_{\vec{k}}}} - 1\right) . \tag{1.28}$$

As anticipated, for $d \geq 2$ the reduction in the magnetization given by (1.28) is finite and the ground state is ordered. For d=1 Eq. (1.28) implies a non-physical divergence due to long-wavelength quantum fluctuations, that clearly points out the failure of standard spin-wave theory and the absence of long-range order in the ground state ("quantum disorder"). It can be shown [Auerbach] that the breakdown of the picture of a Néel-like ground state in the $1D$ *quantum* model arises from the Mermin and Wagner theorem applied to the correspondent *classical* model in $1+1$ dimensions at finite temperature. Thus, in order to describe the low energy properties of the HAF spin chains, *ad hoc* approaches must be developed.

1.4.2 Half-integer spins and integer spins: from Bethe ansatz to Haldane conjecture

On the basis of what recalled in the previous Section, two situations can be expected for the ground state of the HAF chain:

a) *quasi long-range order*, i.e. correlation function of the form (1.8);

b) *disorder*, i.e. correlation function decaying as in Eq. (1.9).

The ground state of the $S = 1/2$ chain has been exactly calculated by Bethe [Bethe 31] and shown to be quasi long range ordered. Later on Lieb, Schultz and Mattis rigorously proved that condition a) applies in general to any half-integer ($S = 1/2, S = 3/2, ...$) spin chain [Lieb 61]. Therefore it seemed quite natural to expect that the same correlation function (1.8) could describe all the $1D$-HAF's at $T = 0$.

In 1983 however, Haldane conjectured that a finite gap occurs in the excitation spectrum of the integer spin chains and that the ground state is, in this case, disordered. Haldane original argument (reviewed in [Affleck 89, Affleck 90b, Auerbach, Fradkin]) is based on mapping the quantum, d-dimensional, HAF onto the *Nonlinear Sigma Model* in $(d+1)$ dimensions, a field theory well known in particle physics and statistical mechanics [Zinn-Justin]. Although such approach turned out not fully rigorous for small values of the spins, the Haldane prediction has been subsequently confirmed by other theoretical analysis [Affleck 87, Gómez 89, Kennedy 92], numerical simulations [Takahashi 88, Takahashi 89, White 92, White 93] and experiments in spin-1 compounds (see section 1.4.3).

From the theoretical point of view, a crucial argument supporting Haldane idea comes from the exact solvable model, known as "AKLT", proposed by Affleck, Kennedy, Lieb and Tasaki [Affleck 87]. For $d = 1$ and $S = 1$, the AKLT hamiltonian is written

$$\mathcal{H}_{AKLT} = \sum_i [\vec{S}_i \cdot \vec{S}_{i+1} + \frac{1}{3}(\vec{S}_i \cdot \vec{S}_{i+1})^2] \,. \qquad (1.29)$$

If each $S = 1$ spin is viewed as two $S = 1/2$ spins in the symmetric triplet state, the ground state $|\psi_{VBS}\rangle$ of $\mathcal{H}_{AKLT}$ corresponds to combine into a singlet each of the two $S = 1/2$ spins at one site with one $S = 1/2$ on the adjacent sites[1]. When periodic boundary conditions are imposed, $|\psi_{VBS}\rangle$ is a non-degenerate singlet, with exponentially decaying magnetic correlations ($\xi_{AKLT} \simeq 0.9$) and a gap $\Delta_{AKLT} \simeq 0.3J$ to the first excited state. The hamiltonian

[1]The analytical definition of the *valence bond solid* state $|\psi_{VBS}\rangle$ and the prove that it is the ground state of the hamiltonian (1.29) is given in [Affleck 87].

(1.29) can be generalized to include a variable weight β to the biquadratic term

$$\mathcal{H}_\beta = \sum_i [\vec{S}_i \cdot \vec{S}_{i+1} - \beta(\vec{S}_i \cdot \vec{S}_{i+1})^2] \,. \qquad (1.30)$$

In the range $-1<\beta<1$ (which includes either the Heisenberg ($\beta = 0$) and the AKLT ($\beta = -1/3$) models), the ground state of $\mathcal{H}_\beta$ describes a unique quantum phase [Kennedy 92]. In this sense $|\psi_{VBS}\rangle$ is considered a suitable qualitative picture of the $S = 1$ HAF chain ground state.

1.4.3 Experimental evidences of a quantum spin gap in $S = 1$ compounds

The opening of a gap in the magnetic excitation spectrum can be experimentally detected by Inelastic Neutron Scattering (INS) and by Nuclear Magnetic Resonance (NMR).

The first evidences of the occurrence of a gap in $S = 1$ HAF compounds (that could not be simply ascribed to magnetic anisotropy) were found in $CsNiCl_3$ [Buyers 86]. However $CsNiCl_3$ is far from being the best candidate for a clear experimental test of Haldane theory, since the relatively large interchain/intrachain coupling ratio ($|J'/J| \simeq 10^{-2}$), induces long range order at $T = 4.85K$.

A better one-dimensional behavior characterizes the compound $Ni(C_2H_8N_2)_2NO_2(ClO_4)$, usually abbreviated as NENP, in which $|J'/J| \approx 10^{-4}$ [Renard 87, Regnault 94], and no long range order has been observed at any temperature. INS in NENP [Renard 87, Renard 88, Regnault 94, Regnault 95] revealed the occurrence, at momentum $q \simeq \pi$, of three gapped excitations, at energy $\Delta_1 = 12K$ and $\Delta_2 = 14K$ and $\Delta_3 = 29K$. One one side these experimental findings support the Haldane conjecture. At the same time they point out the strong anisotropy in the magnetic hamiltonian of NENP, thus preventing a quantitative comparison with the theoretical predictions for the "pure" Heisenberg model (1.4).

More isotropic $1D$ $S = 1$ compounds, such as $AgVP_2S_6$ and Y_2BaNiO_5, have been recently synthesized. The latter nickelate in particular, in view of the strong one-dimensionality of the spin-coupling and of the weak anisotropy, is believed to be a nearly ideal Heisenberg chain with AF interactions. The gapped, almost-degenerate excitations observed in Y_2BaNiO_5 (see Chapter 3) seals

the validity of the mentioned theories for integer-spin HAF chains. Furthermore, in Y_2BaNiO_5 one can performe *non-magnetic* substitutions of magnetic ions and/or charge injections, and to approach experimentally the problem mentioned in the next Section, namely the issue of doped spin liquids.

1.5 Spin liquids and doping

The term "spin liquid" is often used to designate systems that, because of quantum fluctuations, preserve rotational invariance in the ground state in spite of the strong magnetic interactions. However, since there is no rigorous definition of this locution, it may have, for different authors, different meanings (see for instance [Emery 97]). Here will be called "spin liquids" those systems having a gap between the non-degenerate ground state and the first excited level, and therefore exponentially decaying magnetic correlation at $T = 0$. The HAF spin-1 chain belongs to this class, as well as the even-leg spin-1/2 ladder and the dimerized spin-1/2 chain. Even if the hamiltonians describing these systems are different, the low-energy magnetic properties turn out to be very similar, since they are dominated by the singlet-triplet gap.

Exotic behaviors are expected when a spin liquid is doped by localized spinless impurities or by mobile holes.

Let us illustrate the effect of non-magnetic substitutions by first referring to $CuGeO_3$, a compound which, for the richness of its phase diagram, is probably the most studied $1D$ AF (see [Fabrizio 99] and references therein). As a consequence of the dimerization taking place at $T_{SP} \simeq 14K$, the ground state of undoped $CuGeO_3$ is disordered. This is clearly evidenced by the exponential decrease of the uniform spin susceptibility for $T \to 0$. When a small fraction of Cu^{2+} ($S = 1/2$) is substituted by non-magnetic ($S = 0$) ions (Zn^{2+}, Mg^{2+}), the low-temperature susceptibility is strongly enhanced and a second transition is detected at $T_N < T_{SP}$. The phase occurring below T_N is identified as a *Néel-like* state. Analogous order phenomena driven by spin-vacancies have been recently observed in the spin-1/2 two-leg ladder compound $Sr(Cu_{1-x}Zn_x)_2O_3$ [Azuma 97] and in the $S = 1$ chain $Pb(Ni_{1-x}Ng_x)_2V_2O_8$ [Uchiyama 99], confirming the striking prediction by Shender and Kivelson [Shender 91] that, in gapped systems,

quenched disorder in form of dilution can induce order in form of a broken symmetry phase. This is in contrast with what happens in $3D$ AF's, where dilution leads to a reduction of the ordered phase [Feng 92, Corti 97].

The temperature T_N at which the order-transition takes place in the doped spin liquids is proportional to the interchain coupling constant J' [Shender 91, Fabrizio 99]. $CuGeO_3$ and $Pb(Ni_{1-x}Ng_x)_2V_2O_8$, which are rather poor one-dimensional systems ($|J'/J| \approx 10^{-2} \div 10^{-1}$), undergo the transition at a temperature as low as a few Kelvin. So, in highly $1D$ compounds (like Y_2BaNiO_5) the Néel phase, if any, should be restricted to much lower temperatures. However, according to several authors [Fukuyama 96, Fabrizio 97, Laukamp 98], the "magnetic objects" giving rise to the enhancement of AF correlations already exist in absence of any $3D$-coupling, and are identified as localized moments induced in the chain by the impurities. In Chapter 4 it will be shown that such "objects" can be imaged by ^{89}Y NMR in $Y_2BaNi_{1-x}Mg_xO_5$.

Another important issue is the effect of hole-doping in spin liquids, particularly in view of the possible connections with high-T_c superconductivity. Theoretical studies have predicted that the spin gap survives in presence of holes and that the spin-gapped phase is favorable to superconductivity [Dagotto 92, Fabrizio 93]. Actually, there are several experimental indications of gapped-like behavior in underdoped high-T_c cuprates (for a review see [Rigamonti 98]), but the subject is still controversial. Hence, it should be useful to study first how hole-doping affects the spin dynamics of a well-established gapped system. This will be the goal of the ^{89}Y NMR study of Ca-doped Y_2BaNiO_5, described in Chapter 5.

Chapter 2

Probing magnetic correlations by NMR

Nuclear magnetic resonance (NMR) is a powerful technique to investigate static magnetic correlation and low-energy spin dynamics in condensed matter. Through electron-nucleus hyperfine interaction the expectation value of the electron spin affects the nuclear resonance frequency, while the spin fluctuations induce transitions between different nuclear levels. Thus, from the distribution of NMR frequencies and from nuclear relaxation rates, information on the static and dynamic spin-spin correlation function of the electron system are obtained. In this chapter, after having recalled the hyperfine interaction hamiltonian in a form appropriate to the cases discussed later on, the relationship between NMR quantities and electron magnetic properties are discussed.

2.1 Hyperfine interactions in solids: basic aspects

For an isolated nuclear magnetic moment $\vec{\mu} = \gamma\hbar\vec{I}$ in a magnetic field $\vec{H}_0$, the interaction hamiltonian $\mathcal{H}_Z = -\vec{\mu}\cdot\vec{H}_0$ has eigenvalues $E_m = -\gamma\hbar H_0 m$, with $m = -I, -I+1, \ldots\ldots I-1, I$. As a consequence, a system of non-interacting nuclear spins can absorb photons with circular polarization in the $x-y$ plane and angular frequency $\omega_0 = E_{m+1} - E_m = \gamma\, H_0$.

For a nucleus (j) in a solid, the relevant hamiltonian can be written at least as sum of the three terms,

$$\mathcal{H}(j) = \mathcal{H}_Z + \mathcal{H}_{nn}(j) + \mathcal{H}_{ne}(j)\ , \tag{2.1}$$

where

$$\mathcal{H}_{nn}(j) = \sum_k \gamma\gamma_k\hbar^2\vec{I}_j\cdot\left[\frac{\vec{I}_k}{r_{jk}^3} - 3\left(\frac{\vec{r}_{jk}(\vec{I}_k\cdot\vec{r}_{jk})}{r_{jk}^5}\right)\right]\ , \tag{2.2}$$

(with k running over all the nuclei and $\vec{r}_{jk}$ connecting two different sites) is the dipole-dipole nuclear hamiltonian and

$$\mathcal{H}_{ne}(j) = \sum_i \vec{I}_j\,\hat{A}_{ji}\,\vec{S}_i \tag{2.3}$$

describes the electron-nucleus interaction. The hyperfine tensor $\hat{A}_{ji}$ is given by a *classical* dipolar term plus a contact scalar one (A'_{ji}), i.e.

$$A_{ji}^{\alpha\beta} = -\gamma\gamma_e\hbar^2\left[\left(A'_{ji} + \frac{1}{r_{ji}^3}\right)\delta_{\alpha\beta} - \frac{3}{r_{ji}^5}r_{ji}^{\alpha}r_{ji}^{\beta}\right] \tag{2.4}$$

where γ_e is the electron gyromagnetic ratio and r_{ji}^{α} the components of the vector $\vec{r}_{ji}$ connecting the electron i to the nucleus j.

It is immediately evident that the energy correction associated the interaction (2.2) is negligible when compared with the one related to the (2.3). The ratio between the two dipolar terms is in fact of the order of $\gamma/\gamma_e \approx 10^{-3}$. This means that in magnetic systems ($S_i \neq 0$) the nucleus-nucleus interaction produces only second order effects with respect to the hyperfine one.

By introducing the hyperfine field $\vec{h}_j = (-1/\gamma\hbar)\sum_i \hat{A}_{ji}\,\vec{S}_i$, generated by the electrons at the nuclear sites, Eq.(2.3) can be put in the form of an effective Zeeman interaction

$$\mathcal{H}_{ne}(j) = -\gamma\hbar\vec{I}_j \cdot \vec{h}_j \ . \tag{2.5}$$

It is worth to mention that, for $I > 1/2$, a nucleus has a non-zero quadrupolar moment, which couples to the local electric field gradients. In this thesis however, I will deal only with ^{89}Y ($I = 1/2$) nuclei and thus only the magnetic interactions described by Eq.s (2.1)-(2.4) are considered.

2.2 Local fields and NMR spectra

By neglecting the nucleus-nucleus interaction, the total field at the site j is given by $\vec{H}_o + \langle\vec{h}_j\rangle$, and the resonance condition takes the form

$$\omega = \gamma\,|\vec{H}_o + \langle\vec{h}_j\rangle| \ . \tag{2.6}$$

The brackets $\langle\ \rangle$ indicate the statistical average, defined for a generic operator "o" as

$$\langle o\rangle = \frac{1}{N\mathcal{Z}_{\mathcal{H}}} Tr[e^{-\frac{\mathcal{H}_H}{K_B T}}\, o] \ , \tag{2.7}$$

where $\mathcal{H}_H$ and $\mathcal{Z}_H$ are the electronic hamiltonian and the partition function in presence of the external field.

In quantum spin chains, where no spontaneous order occurs at any temperature, $\langle h_j\rangle$ is in general a small fraction of H_0, and hence

$$\omega = \gamma\,(H_o + \langle h_j^z\rangle) = \gamma(H_0 + \sum_i \sum_\alpha A_{ji}^{z\alpha}\,\langle S_i^\alpha\rangle) \ . \tag{2.8}$$

Eq.(2.8) links the resonance frequency to the hyperfine field at the nuclear site and hence to the local expectation values of the electron spin components $\langle S_i^\alpha\rangle$.

The NMR spectrum is obtained experimentally by irradiating the system at different frequencies ω (or equivalently by sweeping H_0) and by measuring the absorption signal. The spectrum is thus a function proportional to the number of nuclei obeying the condition (2.8) and hence contains information on $\langle S_i^\alpha\rangle$. A site-dependence

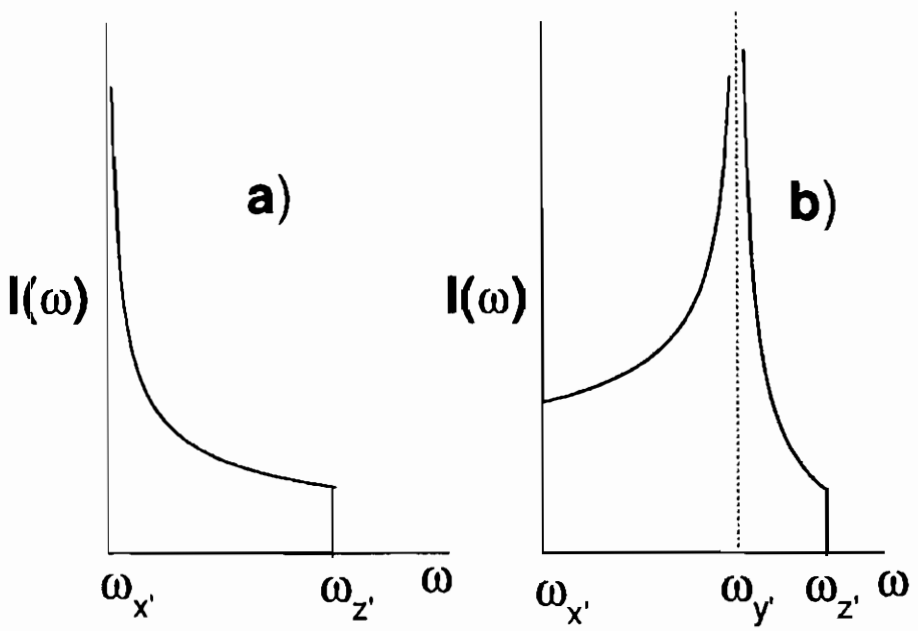

Figure 2.1: Typical NMR line shape for axially symmetric (**a**) and orthorhombic (**b**) hyperfine coupling tensor (from Ref. [Slichter]).

of $\langle S_i^\alpha \rangle$, for instance, can be detected (see Chapter 4) through the spread of resonance frequencies expected from Eq. (2.8).

In polycrystalline samples measurements one has to consider that a distribution of ω arises from the anisotropies in the hyperfine coupling tensor and/or in the susceptibility, which result in a variable alignment of the internal fields $\vec{h}_j$ with respect to H_0. For systems with isotropic magnetic susceptibility, the shape of the distribution functions $I(\omega)$ resulting from different symmetry-type of $\hat{A}_{ji}$ is derived from an angular average [Slichter]. The result for axial symmetry will be recalled here. In this case two diagonal terms of $\hat{A}_{ji}$ (in the basis of its principal axis x', y', z'), and thus two components of the hyperfine field $\vec{h}_j$, are the same. Without any loss of generality, one can fix $h_j^{x'} = h_j^{y'} \neq h_j^{z'}$ and the normalized powder spectrum takes the form

$$I(\omega) = \frac{1}{2\sqrt{(\omega - \omega_{x'})(\omega_{z'} - \omega_{x'})}}, \tag{2.9}$$

where $\omega_{z'} \equiv \gamma(H_0 + h_j^{z'})$ and $\omega_{x'} \equiv \gamma(H_0 + h_j^{x'})$ are the reso-

nance frequencies at those sites where $H_0//h_j^{z'}$ and $H_0 \perp h_j^{z'}$ respectively. Eq. (2.9) holds for ω between $\omega_{x'}$ and $\omega_{z'}$ and has a square root singularity for $\omega = \omega_{x'}$. In any real situation, the infinity is smeared out as a consequence of additional broadening due to nucleus-nucleus interaction (Eq. (2.2)), external field inhomogeneities and/or magnetic impurities. The situation described by Eq. (2.9) is schematically represented in Fig. 2.1, together with the more general case of orthorombic symmetry ($h_j^{x'} \neq h_j^{y'} \neq h_j^{z'}$).

2.3 Nuclear relaxation times

After a radiofrequency pulse at the resonance condition (inducing a non-equilibrium occupation of the Zeeman levels), a system of all-equivalent $I = 1/2$ nuclei recovers exponentially the equilibrium configuration, with a characteristic time T_1 called *spin-lattice relaxation time*. T_1 is related to the transition probabilities $W_{\pm\to\mp}$ between the states $|+> \equiv |I^z = +1/2>$ and $|-> \equiv |I^z = -1/2>$ through the expression [Bloembergen 48]

$$\frac{1}{T_1} = (W_{-\to+} + W_{+\to-}) \,. \tag{2.10}$$

The hyperfine interaction $\mathcal{H}_{ne}$ is the only efficient mechanism in coupling $I = 1/2$ nuclei to the external environment (lattice), and thus the relaxation process is driven by the exchange of energy between the nuclear and the electronic spin systems.

An expression linking $1/T_1$ to the electronic spin-spin correlation functions is now derived in the framework of time-dependent perturbation theory. The probability per unit time to have a nuclear spin flip $|-> \to |+>$, accompanied by a transition of the electron system ($\mathcal{H}_H$) between the states $|\epsilon>$ and $|\epsilon'>$, is given by the Fermi's Golden Rule

$$W_{(-,\epsilon)\to(+,\epsilon')} = \frac{2\pi}{\hbar} |<+,\epsilon'|\mathcal{H}_{ne}|-,\epsilon>|^2 \delta(E_{\epsilon'} - E_\epsilon - \hbar\omega) \frac{e^{-E_\epsilon/K_B T}}{\mathcal{Z}_H} \,, \tag{2.11}$$

in which E_ϵ is the energy of the state $|\epsilon>$. The hyperfine coupling can be conveniently rewritten in terms of creation and annihilation

operators to put in evidence those terms contributing to the nuclear relaxation

$$\mathcal{H}_{ne} = \sum_{i,\alpha} \frac{1}{2} \left(I_j^+ A_{ji}^{-\alpha} S_i^\alpha + I_j^- A_{ji}^{+\alpha} S_i^\alpha \right) + I_j^z A_{ji}^{z\alpha} S_i^\alpha \,, \tag{2.12}$$

where $I_j^\pm \equiv I_j^x \pm I_j^y$ and $A_{ji}^{\pm\alpha} \equiv A_{ji}^{x\alpha} \pm A_{ji}^{y\alpha}$. For the transition $|- > \rightarrow |+ >$ the only nonvanishing matrix-elements are the ones involving the operators $I_j^+ A_{ji}^{-\alpha} S_i^\alpha$, and thus

$$W_{(-,\epsilon)\rightarrow(+,\epsilon')} = \frac{\pi}{2\hbar} |\sum_{i,\alpha} A_{ji}^{-\alpha} < \epsilon' | S_i^\alpha | \epsilon > |^2 \delta(E_{\epsilon'} - E_\epsilon - \hbar\omega) \frac{e^{-E_\epsilon / K_B T}}{\mathcal{Z}_H} \,. \tag{2.13}$$

The analogous expression for $W_{(+,\epsilon')\rightarrow(-,\epsilon)}$ is

$$W_{(+,\epsilon')\rightarrow(-,\epsilon)} = \frac{\pi}{2\hbar} |\sum_{i,\alpha} A_{ji}^{+\alpha} < \epsilon | S_i^\alpha | \epsilon' > |^2 \delta(E_\epsilon - E_{\epsilon'} - \hbar\omega) \frac{e^{-E_{\epsilon'} / K_B T}}{\mathcal{Z}_H} \,. \tag{2.14}$$

Since $A_{ji}^{+\alpha} = (A_{ji}^{-\alpha})^*$, one obtains

$$\left(\frac{1}{T_1} \right)_{\epsilon \leftrightarrow \epsilon'} = \frac{\pi}{2\hbar} |\sum_{i,\alpha} A_{ji}^{-\alpha} < \epsilon' | S_i^\alpha | \epsilon > |^2 \cdot \cdot \delta(E_{\epsilon'} - E_\epsilon - \hbar\omega) \frac{(e^{-E_\epsilon / K_B T} + e^{-E_{\epsilon'} / K_B T})}{\mathcal{Z}_H} \,, \tag{2.15}$$

and by summing over all the possible transitions of the electron spin system

$$\frac{1}{T_1} = \frac{\pi}{2\hbar} \sum_{\epsilon,\epsilon'} |\sum_{i,\alpha} A_{ji}^{-\alpha} < \epsilon' | S_i^\alpha | \epsilon > |^2 \cdot \cdot \delta(E_{\epsilon'} - E_\epsilon - \hbar\omega) \frac{(e^{-E_\epsilon / K_B T} + e^{-E_{\epsilon'} / K_B T})}{\mathcal{Z}_H} \,. \tag{2.16}$$

Expression (2.16) can be rewritten, by using the integral representation of the Dirac-deltafunction and time-dependent spin operators $S_i^{\alpha}(t) = e^{i\mathcal{H}_e t/\hbar} S_i^{\alpha} e^{-i\mathcal{H}_e t/\hbar}$, in the form [Moriya 56]

$$\frac{1}{T_1} = \frac{1}{2\hbar^2} \int_{-\infty}^{+\infty} dt e^{-i\omega t} \langle \left\{ \sum_{i,\alpha} A_{ji}^{-\alpha} S_i^{\alpha}(t) \, , \sum_{l,\beta} A_{jl}^{+\beta} S_l^{\beta}(0) \right\} \rangle \qquad (2.17)$$

where, for two generic operators o and p, $\{o,p\} \equiv \frac{1}{2}(op+po)$ and $<>$ denotes the thermal average defined by Eq. (2.7). As anticipated, $1/T_1$ probes the dynamic (field-dependent) correlation function of the electron spin system at the nuclear Larmor frequency.

When the excitations of the system are studied in reciprocal space, Eq.(2.17) can be reformulated in terms of Fourier components of the spin operators

$$S_i^{\alpha} = \mathcal{N}^{-1/2} \sum_{\vec{q}} S_{\vec{q}}^{\alpha} e^{i\vec{q}\cdot\vec{r}_j}, \qquad (2.18)$$

and of dynamic structure factor

$$S^{\alpha\beta}(\vec{q},\omega) = \mathcal{N}^{-1} \int_{-\infty}^{+\infty} dt e^{-i\omega t} < \left\{ S_{\vec{q}}^{\alpha}(t) \, , \, S_{-\vec{q}}^{\beta}(0) \right\} > , \qquad (2.19)$$

the relaxation rate tacking the form

$$\frac{1}{T_1} = \frac{1}{2\hbar} \sum_{\alpha,\beta} \sum_{\vec{q}} A_{\vec{q}}^{-\alpha} A_{-\vec{q}}^{+\beta} \, S^{\alpha\beta}(\vec{q},\omega) \qquad (2.20)$$

where $A_{\vec{q}} = \sum_i A_{ji} e^{i\vec{q}\cdot\vec{r}_{ji}}$. Moreover, from the fluctuation - dissipation theorem

$$S(\vec{q},\omega) = \frac{2}{1 - e^{-\hbar\omega/T}} \chi''(\vec{q},\omega) \, , \qquad (2.21)$$

an expression connecting $1/T_1$ to the imaginary part of dynamic susceptibility $\chi''(\vec{q},\omega)$ is obtained [Moriya 63] in the limit $\hbar\omega << K_B T$

$$\frac{1}{T_1} = \frac{K_B T}{\hbar^2} \sum_{\alpha,\beta} \sum_{\vec{q}} A_{\vec{q}}^{-\alpha} A_{-\vec{q}}^{+\beta} \, \frac{\chi''_{\alpha\beta}(\vec{q},\omega)}{\omega} \, . \qquad (2.22)$$

Chapter 3

^{89}Y NMR study of the Haldane chain Y_2BaNiO_5

The compound Y_2BaNiO_5 is close to the ideal realization of the $S = 1$ Heisenberg chain with antiferromagnetic interactions. In this Chapter, after a brief review of its structural and electronic properties, the experimental results obtained in this system by ^{89}Y NMR spectra and relaxation (and complementary magnetic susceptibility measurements) are presented. The typical shape of the resonance line is shown to arise from the compensation between the difference in the components of the hyperfine tensor (at orthorombic symmetry) and the anisotropy in the single-ion susceptibility, yielding a local field at axial symmetry. The value of the Haldane gap Δ_H, deduced from the low-temperature behavior of the NMR line-shift, turns out in good agreement with the estimation from inelastic neutron scattering. On the other hand, the spin-lattice relaxation rate $1/T_1$ decreases, on decreasing temperature, with an exponential law leading to a gap $\Delta_{dyn} \approx 2\Delta_H$. This finding is discussed in term of the multimagnon processes contributing to the dynamical structure factor.

3.1 Structural and electronic properties

Ln_2BaNiO_5 compounds crystallize in two different structural types depending on the size of the rare earth element (Ln) [Schiffler 86a, Schiffler 86b, Schiffler 87, Muller 88, Muller 89]. For the smallest ones (Ln = Yb, Lu), the crystallographic structure is isostructural to the Ln_2BaCuO_5 series, in which the transition metal ions are located in a distorted square based pyramidal environment [Michel 82, Michel 84]. On the contrary, for Ln: Nd $\rightarrow$ Tm and Y, the nickel occupies the centers of NiO_6 octahedra sharing the apical oxygens an forming linear chains [Schiffler 86a, Schiffler 87, Buttrey 90].

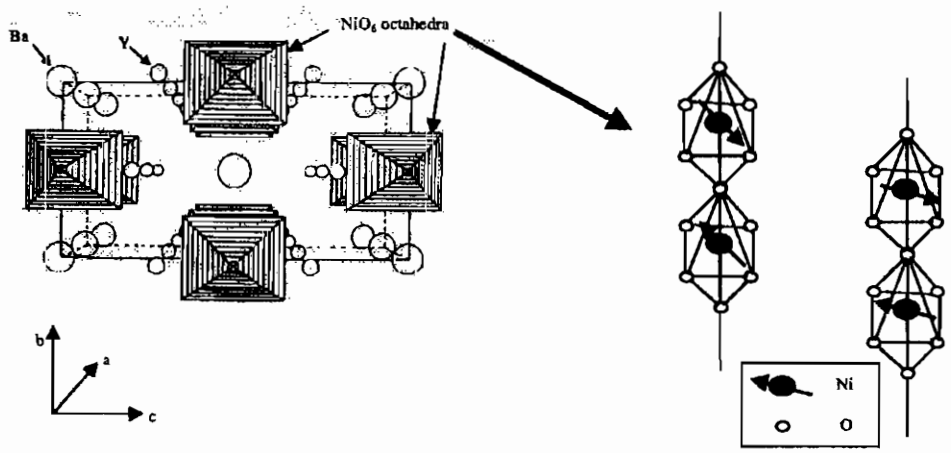

Figure 3.1: Crystal structure of Y_2BaNiO_5 with indication of the main axis and a blow-up of the Ni-O-Ni chains contained in the corner-shared NiO_6 octahedra. The prospective view on the left side is from Ref. [Darriet 93].

A schematic view of the crystal structure of Y_2BaNiO_5 is given in Fig. 3.1. The intrachain distance a between Ni^{2+} ($S = 1$) ions is 3.76Å. Ni-$3d_{(3a^2-r^2)}$ and O-$2p_a$ orbitals overlap along the

chain direction, by forming a 180^0 Ni-O-Ni angle and giving rise to a superexchange path strongly efficient in producing effective AF coupling J [Anderson 59]. On the other hand, the superposition of Ni-3d orbitals centered on different chains is rather small, due to the distance separating nearest neighour Ni^{2+} ions (about 6.6Å) and to the unfavorable direction of the connecting axis, which does not belong to any of the 3d-orientations.

The occurrence of $1D$-AF correlation in Y_2BaNiO_5 is clearly evidenced by the broad maximum at $T \approx 410K$ in the magnetic susceptibility [Darriet 93], from which the value of the intrachain coupling constant $J = 285K$ is derived. A straightforward confirm of the excellent one-dimensionality comes from Muon Spin Rotation (μSR) measurements, which show absence of long range order down

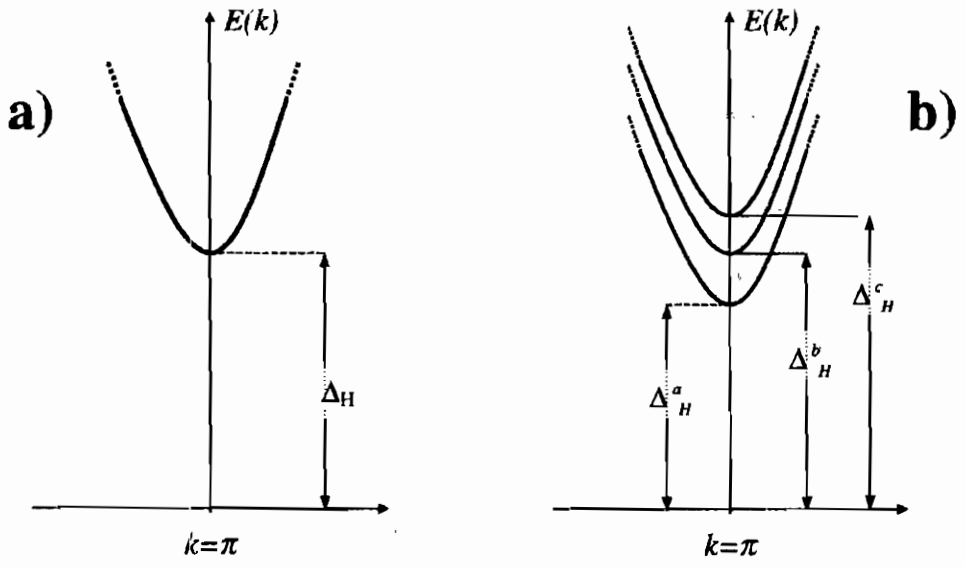

Figure 3.2: Low-energy magnetic levels for **a)** fully-isotropic $S = 1$ AF chain; **b)** the compound Y_2BaNiO_5, as derived by INS [Sakaguchi 96, Xu 96]. The anisotropy terms D and E in the hamiltonian (3.1) separate the three component of the degenerate gapped triplet.

to $100mK$.

From the experiments performed in Y_2BaNiO_5 strong support to the Haldane conjecture [Haldane 83] has been found. INS measurements [Sakaguchi 96, Xu 96] reveal the existence of a finite gap Δ_H in the magnetic excitation spectrum, having its minimum value at $k = \pi$ (in inverse lattice units a^{-1}) and a weak dependence on the polarization direction. Along $\vec{a}$, $\vec{b}$ and $\vec{c}$ (see Fig. 3.1), one has respectively $\Delta_H^a = 89K$, $\Delta_H^b = 102K$ and $\Delta_H^c = 112K$ (Fig. 3.2).

The small differences between Δ_H^a, Δ_H^b, and Δ_H^c implicate the presence of weak single ion anisotropy terms in the magnetic hamiltonian [Golinelli 92]. This last, by neglecting the interchain interaction, takes the form [Sakaguchi 96]

$$\mathcal{H}_e = J \sum_i \vec{S}_i \cdot \vec{S}_{i+1} + D \sum_i (S_i^a)^2 + E \sum_i [(S_i^b)^2 - (S_i^c)^2] \quad (3.1)$$

with $D = -8K$ and $E = 3K$. INS also provided an upper limit estimation for the inter/intrachain coupling ratio: $|J'/J| \leq 1 \div 5 \times 10^{-4}$. These values are more than one order of magnitude smaller than the critical ratio required to induce a magnetically ordered ground state [Kosevich 86, Sakai 90].

3.2 Experimental results

3.2.1 Magnetic susceptibility

Magnetization measurements has been performed on polycrystalline Y_2BaNiO_5 by SQUID (Superconducting Quantum Interference Device) magnetometer[1]. Synthesis and characterization of the sample are described in Appendix.

The magnetization curves $M(H_0)$ appear almost linear up to $\simeq 7T$ (Fig. 3.3), and no appreciable difference has been found in magnetic susceptibility $\chi \equiv M/H_0$ between field cooled (FC) and zero field cooled (ZFC) conditions.

The temperature behavior of χ, reported in Fig. 3.4 a), is in good agreement with data previously reported by other authors [Darriet 93, Yokoo 95, Shimizu 95]. At low temperature ($T \leq$

[1]METRONIQUE INGEGNERIE SQUID M03, equipped by 8T magnet and operating in the range 2 - 300K, installed at the *Department of Chemistry - University of Firenze.*

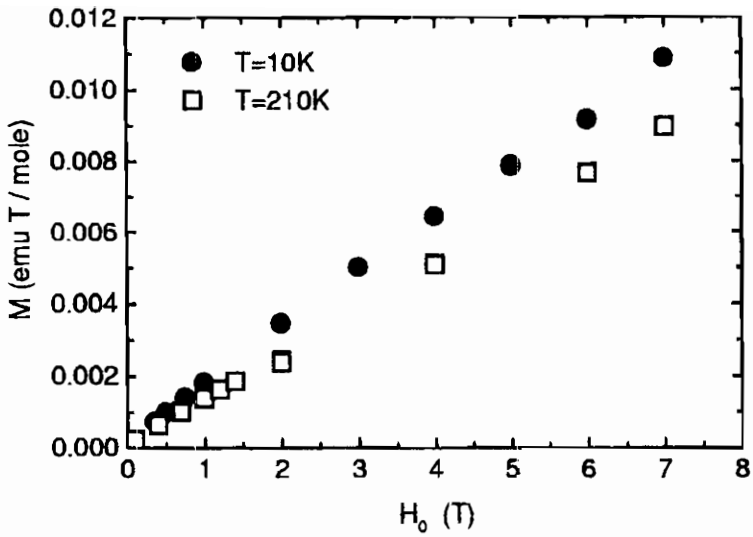

Figure 3.3: Typical magnetization curves in Y_2BaNiO_5.

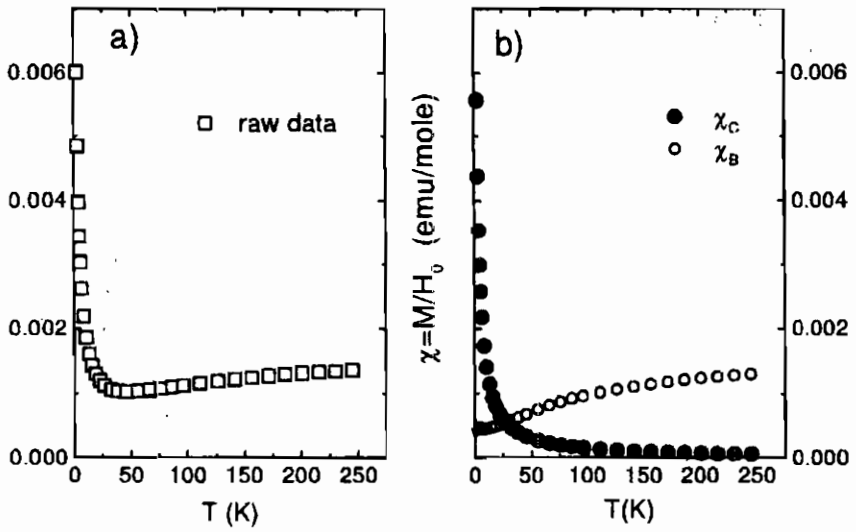

Figure 3.4: **a)** Y_2BaNiO_5 magnetic susceptibility in $H_0 = 0.1T$; **b)** Contributions to the susceptibility: χ_C is the Curie term related to the chain's boundaries, while χ_B is the susceptibility pertaining to the bulk of the chains (from Ref. [Tedoldi 98]).

$20K$), a Curie-like divergence is observable, in contrast to the decrease of χ that is expected for an ideal (infinite) HAF $S = 1$ chain, when the temperature is lowered [Affleck 90a, Jolicœur 94]. In the next chapter it will be shown how this discrepancy can be related to the occurrence of an extra-magnetization localized at the boundaries of the chains, which in any real compound have finite length. In order to study the properties of the "bulk" (central part of the chains) we have first derived the magnitude of this Curie term χ_C from a fitting of the data at very low temperature ($T \leq 10K$), and then subtract it from the raw data shown in Fig. 3.4. The result χ_B, is reported together with χ_C in Fig. 3.4b).

3.2.2 ^{89}Y NMR spectra

^{89}Y NMR spectra have been measured in Y_2BaNiO_5 for different values of the external magnetic field[2]. For $T > 20K$ the distribution of resonance frequencies was achieved by a single Fourier Transform (FT) of the NMR echo signal. At lower temperature, a convolution of the FT's of the signals detected, at fixed field, in correspondence of different irradiation frequency, has been performed.

Representative spectra are shown in Fig. 3.5a). The normalized shift of the maximum K with respect to the ^{89}Y reference signal (see caption), is much larger than the spectral frequency distribution around K. This means that the spread of local fields $\langle h_j^z \rangle$ at the ^{89}Y nuclear sites is small compared to the j-averaged value of $\langle h_j^z \rangle$. In other words, each nucleus experiences almost the same local field, independently on the orientation of the powder grain to which it belongs, pointing out that the scalar transferred hyperfine coupling dominates over the dipolar term. The latter indeed is responsible of the typical asymmetric shape of the spectra, which is well observable at $T = 293K$ and tends to disappear when the temperature is lowered. An additional source of broadening is the anomalous magnetization occurring at the chain-edge's producing the Curie-divergence in the macroscopic susceptibility (see Section 3.2.1). These boundary effects, which smooth the shape of the pow-

[2]The NMR data presented in this Chapter have been collected by a BRUKER spectrometer MSL200 equipped with a 5.9 T OXFORD superconducting magnet (installed at the *Department of Physics "A. Volta" - University of Pavia*) and by a BRUKER spectrometer AMX400 equipped with a 9.4 T OXFORD superconducting magnet (installed at the *Centro grandi strumenti - University of Pavia*).

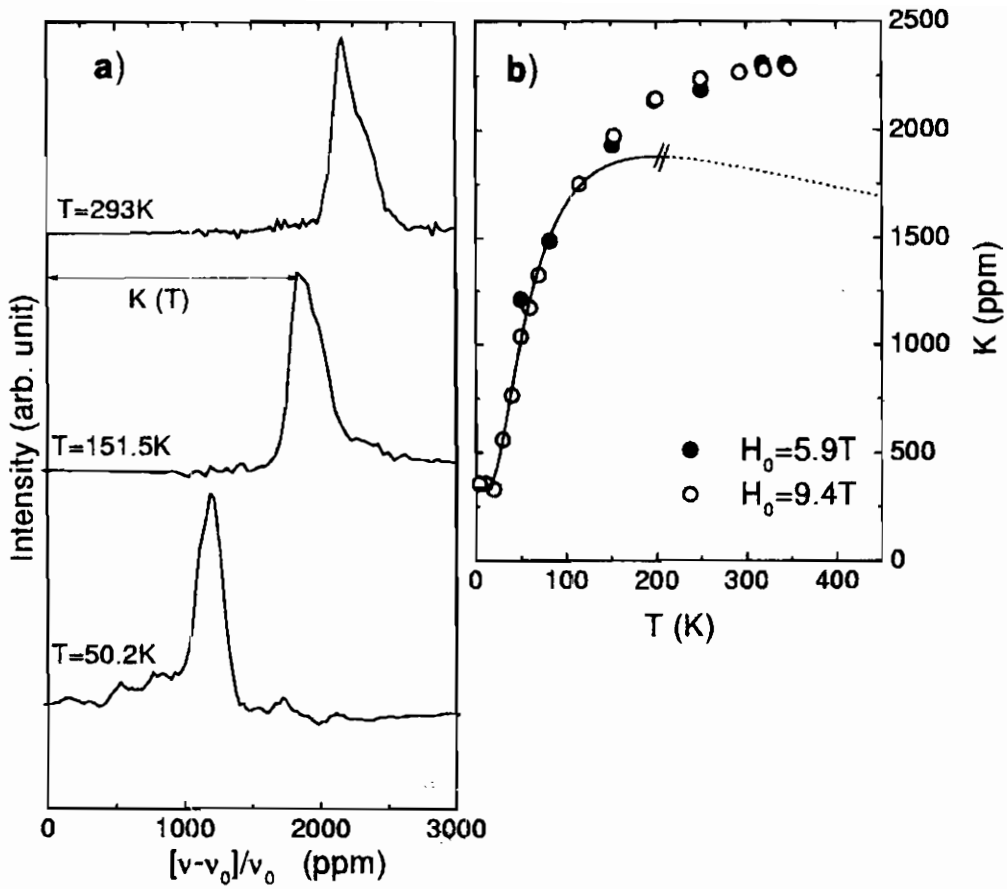

Figure 3.5: **a)** Representative ^{89}Y NMR spectra in Y_2BaNiO_5 obtained, at $H_0 = 5.9T$, by sweeping the irradiation frequency ν. On the x-scale the relative difference between ν and the ^{89}Y signal measured, in the same field, in a YCl_3 solution (ν_0) is reported in parts per million; **b)** temperature behavior of the shift $K(T)$ of the NMR line for different values of the external field. The solid line is the best fit of the data, for $T < 150K$, according to Eq. (3.8).

der patters at high temperature, become dominant in determining the linewidth at $T < 20$. However most of the nuclei are close to Ni^{2+} ions belonging to central parts of the chains and therefore are not affected by such perturbation. Their shifts ($\sim K$) directly reproduce the susceptibility of the bulk and thus of the ideal infinite

system. The temperature behavior of K (Fig. 3.5b)) becomes, in this way, a powerful test to verify the existence of a gap in the magnetic excitation spectrum. A gap which will be quantitatively estimated later on, but that, from the independence of K on H_0, can be expected to be much larger than the Zeeman energy $g\mu_B H_0$ ($\approx 10K$).

3.2.3 Spin-lattice relaxation rates

The evolution of the ^{89}Y nuclear magnetization $M_z(\tau)$ after a sequence of saturating pulses at the central frequency ω_N of the correspondent spectrum has been measured in Y_2BaNiO_5 by using standard echo sequences. Typical recovery plots are shown in Fig.

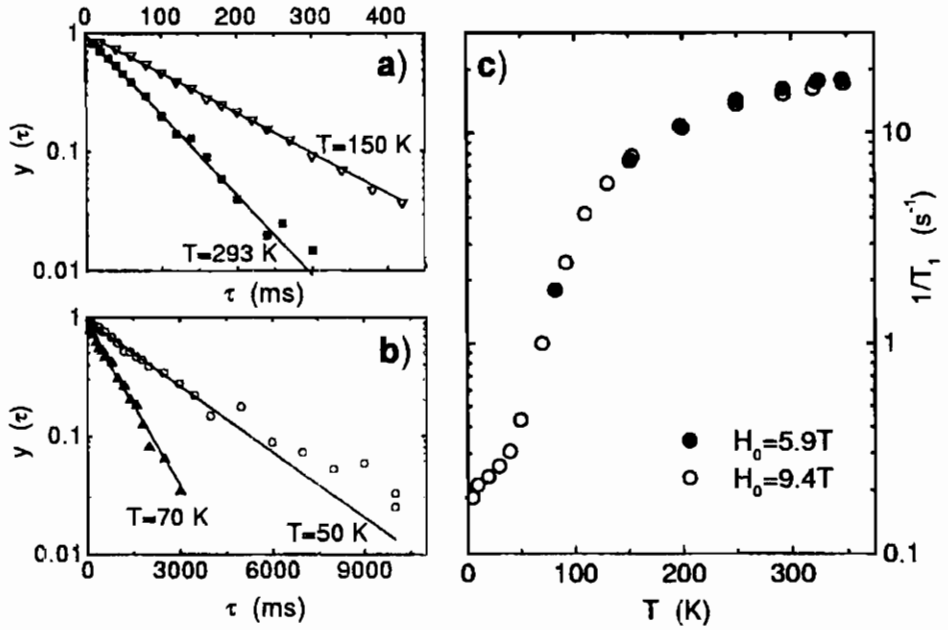

Figure 3.6: **a)** and **b)** Recovery plots $y(\tau) \equiv [M_z(\infty) - M_z(\tau)]/M_z(\infty)$ of the ^{89}Y nuclear magnetization along $z(//H_0)$ in Y_2BaNiO_5. Results at selected temperatures in $H_0 = 9.4T$ are reported. The spin-lattice relaxation rate $1/T_1$ has been extracted by fitting the data according to Eq. (3.2) in the text. At $T = 50K$, a departure from a single exponential behavior begins to appear, indicating impurities-contributions to the relaxation. **c)** Spin lattice relaxation rate as a function of temperature, for different fields H_0.

3.6a) and 3.6b).

In the high temperature range, $M_z(\tau)$ recovers exponentially towards its equilibrium value $M_z(\infty)$ according to the law

$$y(\tau) \equiv \frac{M_z(\infty) - M_z(\tau)}{M_z(\infty)} = e^{-\tau/T_1} , \qquad (3.2)$$

which directly provides the relaxation rates $1/T_1$ (Fig. 3.6c)). For $T \leq 50K$, $y(\tau)$ starts to deviate from a single-exponential behavior, indicating the occurrence of site dependent relaxation processes. Later on it will be pointed out how "local" contributions to $1/T_1$ can arise from the fluctuations of the extra-spins located at the chain's boundaries. Here the data of $M_z(\tau)$ have been fitted to Eq. (3.2) even for $T \leq 50K$, where the extracted values of $1/T_1$ have to be considered average relaxation rates.

Analogously to the the shift (Fig. 3.5c)), $1/T_1$ decreases on decreasing temperature without any dependence from the external field up to $H_0 = 9.4T$ (Fig. 3.6c)).

3.3 Hyperfine coupling and NMR lineshape

In order to extract from the NMR data insights on the magnetic correlations in Y_2BaNiO_5, the properties of the hyperfine tensor $\hat{A}_{ji}$ coupling Ni^{2+} ions to ^{89}Y nuclei must first be discussed.

$\hat{A}_{ji}$ (Eq. (2.4)) is given by a scalar contact term A'_{ji}, due to transferred hyperfine interaction, and by a dipolar part. This latter induces tensorial character to $\hat{A}_{ji}$ and in NMR powder spectra it causes a broadening of the line. As remarked in section 3.2.2, the ^{89}Y linewidth in Y_2BaNiO_5 is in general much smaller than the shift K, pointing out that the hyperfine coupling is dominated by the scalar term A'_{ji}.

The magnitude of A'_{ji} can be derived by the analysis of the shift $K(T)$ versus the chain susceptibility $\chi_B(T)$. The extrapolated values of these two quantities at $T = 0$ are non-zero (Fig.s 3.4 and 3.5) in contrast with the theoretical expectations for the $S = 1$ chain [Affleck 90a, Jolicœur 94]. The residual terms $K(0)$ and $\chi_B(0)$ are related to temperature-independent orbital contributions (Van Vleck susceptibility) in the magnetic response and must be

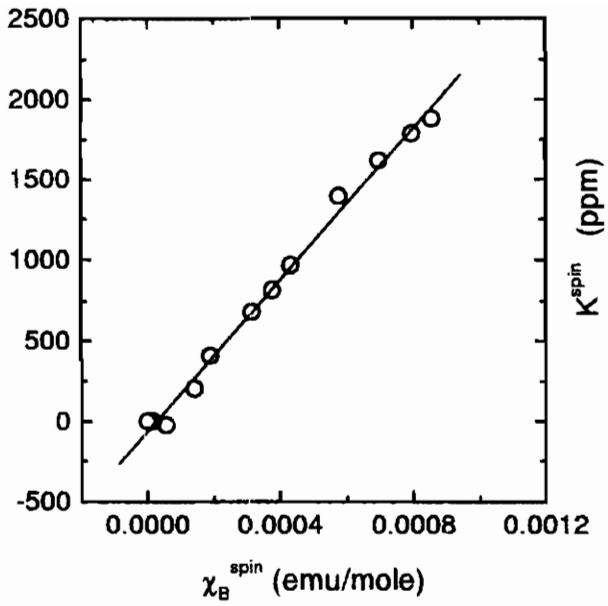

Figure 3.7: T-dependent part of the ^{89}Y NMR shift in $H_0 = 9.4T$ plotted as a function the spin susceptibility χ_B^{spin}, with temperature as intrinsic parameter. The solid line is a linear interpolation of the data according to Eq. (3.3.)

subtracted in order to deduce the spin components $K^{spin}(T) = K(T) - K(0)$ and $\chi_B^{spin}(T) = \chi_B(T) - \chi_B(0)$. Then one has

$$K^{spin}(T) = \frac{\langle h^z \rangle}{H_0} \simeq \frac{\sum_i A'_{ji} \langle S_i^z \rangle}{\gamma \hbar H_0} = \frac{\sum_i A'_{ji} \chi_B^{spin}}{N_A \gamma \gamma_e \hbar^2} \qquad (3.3)$$

where N_A is the Avogadro's number and $\langle h^z \rangle$ the hyperfine field at the ^{89}Y site (neglecting for the moment the dipolar interactions). From the plot of $K^{spin}(T)$ as a function of χ_B^{spin} (Fig. 3.7) one obtains, by means of Eq. (3.3), $A_T \equiv \sum_i A'_{ji}/\gamma\hbar = 26\, KGauss$.

Transferred hyperfine interaction requires extension of the Ni^{2+}–$3d$ orbitals at the ^{89}Y site and thus only ions close enough can couple to a given nucleus. In Y_2BaNiO_5, each ^{89}Y has two nearest neighbor (nn) Ni^{2+} on a same chain and two next nearest neighbors

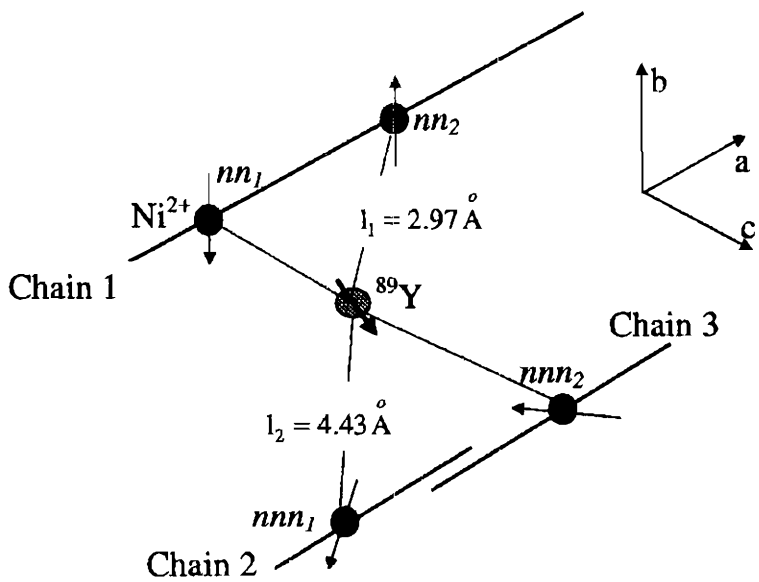

Figure 3.8: Schematic representation of the magnetic structure around a given ^{89}Y nucleus in Y_2BaNiO_5. The Ni^{2+} which are nearest neighbors to the nuclear probe are indicated as *nn*, while the next nearest neighbor ions are labelled as *nnn*.

(*nnn*) on different chains (Fig. 3.8). However, the Y lattice position belongs neither to magnetic-chain-axis (along which the $3d_{(3a^2-r^2)}$ are directed), nor to the bases of the NiO_6 octahedra where the $3d_{(b^2-c^2)}$ orbitals of *nn* - Ni^{2+} lies. Thus the contribution of *nn* ions to A_T is expected to be weak, as noted also by Shimizu et al. [Shimizu 95]. On the other hand, the bases of *nnn* octahedra overlap the Y-site, suggesting that A_T is essentially due to *nnn* ions. Hence we will have

$$A \equiv \frac{A'_{ji}}{\gamma\hbar} \simeq 13kGauss \quad \text{if } (j) \text{ and } (i) \text{ are } nnn\,, \qquad (3.4)$$

while

$$\frac{A'_{ji}}{\gamma\hbar} \simeq 0 \qquad \text{if } (j) \text{ and } (i) \text{ are not } nnn\ . \qquad (3.5)$$

Let us discuss now the shape of the NMR spectra. As it appears from Fig. 3.9, the lineshape is rather well described by the angular distribution of a local field at cylindrical symmetry, after taking into account a proper smoothing factor (see Sec. 2.2). This evidence could seem surprising [Shimizu 95], since the Y-site point symmetry is lower than axial. It is noted, however, that also the anisotropy in the spin susceptibility must be considered in order to derive the NMR lineshape. Measurements performed on single crystal of Y_2BaNiO_5 [Yokoo 95] indicate that χ is not a *pure* scalar (as implicitly assumed until now), but rather a tensor with weak differences in its diagonal components. By using the data of $\hat{\chi}$ reported in Ref. [Yokoo 95], the expectation value of the electronic spin has been calculated and the hyperfine field $\langle \vec{h}_{dip} \rangle$ at the Y-site due to *nn* dipolar interactions derived. The differences in the components of $\langle \vec{h}_{dip} \rangle$ along the crystal axis turn out, at $T = 293K$,

$$\frac{\langle h^a_{dip} \rangle - \langle h^b_{dip} \rangle}{H_0} \simeq 366ppm \qquad \text{and} \qquad \frac{\langle h^c_{dip} \rangle - \langle h^b_{dip} \rangle}{H_0} \simeq 8ppm\ . \qquad (3.6)$$

The separation between $\langle h^b_{dip} \rangle$ is $\langle h^c_{dip} \rangle$ is almost negligible, justifying the axial symmetry in the ^{89}Y spectrum. At the same time the difference $\langle h^a_{dip} \rangle - \langle h^b_{dip} \rangle$ accounts for the line-broadening (see Fig. 3.9).

On cooling the dipolar broadening decreases, as well as the average shift (Fig. 3.5), tracking the behavior of the chain susceptibility. The linewidth has a minimum around $40K$. Then, below this temperature, the NMR spectrum turns out homogeneously broadened, with no signature of dipolar structure. This homogeneous broadening becomes dramatic below $20K$, suggesting that it is due the localized chain defects causing the Curie-like term in the macroscopic susceptibility. This issue will be discussed in the next Chapter, where the effects related to the finite size of the chains will be studied systematically. For the moment one notes that, at high temperature (where $\chi_C << \chi_B$), this additional broadening justify the "smoothing" of the powder patters (Fig. 3.9).

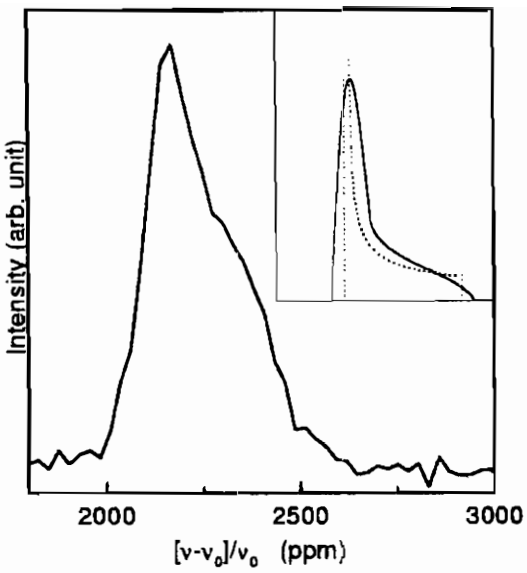

Figure 3.9: ^{89}Y NMR spectrum at $T = 293K$ and $H_0 = 5.9T$, compared to a theoretical powder distribution at axial symmetry (dotted line in the inset). The introduction of a "smoothing" factor (solid line in the inset) evidences the analogy between the theoretical function and the experimental findings.

3.4 Haldane gap from ^{89}Y NMR shift

The spin susceptibility of the Haldane chain has been calculated in the framework of the "Free Boson Model" [Affleck 90a] and more recently through Nonlinear σ Model [Jolicœur 94]. In the low temperature limit ($T < \Delta_H$), the following behavior is predicted

$$\chi_B^{spin}(T) = \chi^* \sqrt{\frac{\Delta_H}{T}}\, e^{-\frac{\Delta_H}{T}} , \qquad (3.7)$$

with χ^* constant.

The data for χ_B reported in Fig. 3.4b), after subtraction of the orbital contribution $\chi_B(0)$, can be fitted rather well by Eq. (3.7)

for $T \leq 100K$, providing the value $\Delta_H = 92 \pm 10K$ for the Haldane gap [Tedoldi 98]. This estimate, however, is somewhat affected by the procedure used to deduct the Curie-like contribution χ_C.

A more accurate result is obtained by the analysis of the shift K, which directly probes χ_B^{spin}. By fitting $K(T)$ (Fig. 3.5b)) according to the expression

$$K(T) = K(0) + K^* \sqrt{\frac{\Delta_H}{T}}\, e^{-\frac{\Delta_H}{T}} , \tag{3.8}$$

one derives $\Delta_H = 102 \pm 5K$ [Tedoldi 99b], consistent with the value from macroscopic susceptibility and in good agreement with the average gap $\overline{\Delta}_H = (\Delta_H^a + \Delta_H^a + \Delta_H^a)/3 = 101K$ measured by inelastic neutron scattering [Sakaguchi 96, Xu 96].

It is noted that, if one assumes $J = 285K$ [Darriet 93], the ratio Δ_H/J turns out only 15% smaller than the value numerically evaluated [White 93] for the HAF $S = 1$ model ($\Delta_H^{th} = 0.4105J$). This can be assumed as an estimate of the approximation that one introduce in describing Y_2BaNiO_5 as an isotropic Heisenberg chain.

3.5 Spin dynamics from ^{89}Y nuclear relaxation

^{89}Y spin-lattice relaxation rates, measured in Y_2BaNiO_5 at $H_0 = 9.4T$, are plotted in Fig. 3.10 as a function of $1000/T$. For $50K \leq T \leq 350K$ the experimental data are well described by the law

$$\frac{1}{T_1} = w\, e^{-\frac{\Delta_{dyn}}{T}} \tag{3.9}$$

with $\Delta_{dyn} = 228 \pm 5K$ (solid line). Below $50K$, $1/T_1$ becomes practically temperature-independent and a noticeable deviation from the single-exponential behavior is observed in the recovery laws (Fig. 3.6). In general this fact indicates the occurrence of a distribution of relaxation rates and thus site-dependent spin fluctuations (see [Corti 97, Tedoldi 99a]). In the $S = 1$ compound $Ni(C_2H_8N_2)_2NO_2(ClO_4)$, the low-$T$ multi-exponential character of the recovery-laws has been attributed to the effect of $S = 1/2$ fractional spins localized in correspondence of chain's defects [Goto 97]. According to this observation, one can conveniently analyze the bulk properties of the system by considering only the temperature range in which

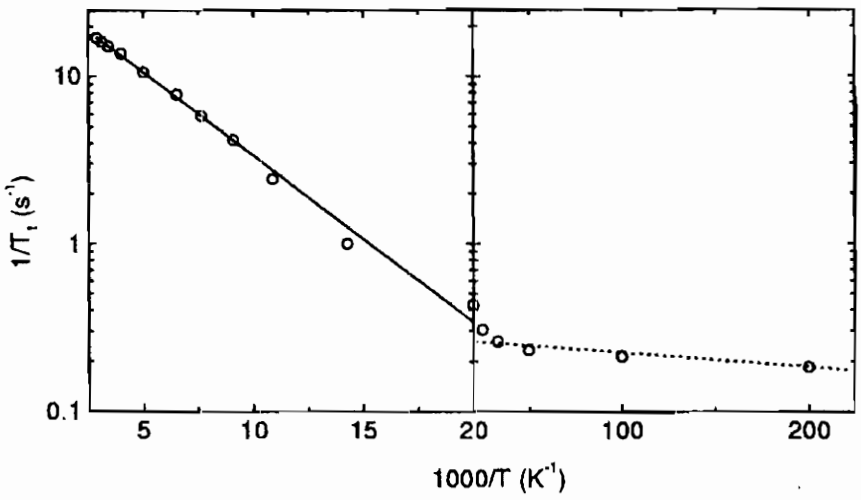

Figure 3.10: ^{89}Y $1/T_1$ in Y_2BaNiO_5 (circles) reported as a function of $1000/T$, for $H_0 = 9.4T$. The exponential decrease (on cooling) indicates the gapped-character of the low-energy spin fluctuations. Fitting of the data at $T \geq 50K$ according to Eq. (3.9) (solid line) provides the value of the "dynamical gap" $\Delta_{dyn} = 228 \pm 5K$. For $T < 50K$ the relaxation mechanism is controlled by "impurities" (see text) and $1/T_1$ becomes practically T-independent (note the change in the x-scale).

the recovery laws are exponential (i.e., in Y_2BaNiO_5, the range $T \geq 50K$).

Let us look for the effective relaxation mechanisms, in the light of excitation spectrum for the $S = 1$ HAF chain (Fig. 3.11), as derived from Monte Carlo calculations [Takahashi 88, Takahashi 89]. According to these estimates, the single magnon[3] dispersion curves have a minimum at $k = \pi$ (with energy $\epsilon = \Delta_H$) and increase on moving towards the center of the Brillouin-zone. For $k < 0.3\pi$ the single magnon energy is larger than the one of two magnons having the same total momentum. Thus, in this k-range, the low-lying excitations belongs to a two magnon-continuum with mini-

[3]While in classical AF the term "magnon" is used to indicate spin-wave excitations (true Goldstone-modes), in quantum disordered systems it is generically employed for low-lying one-particle excited states.

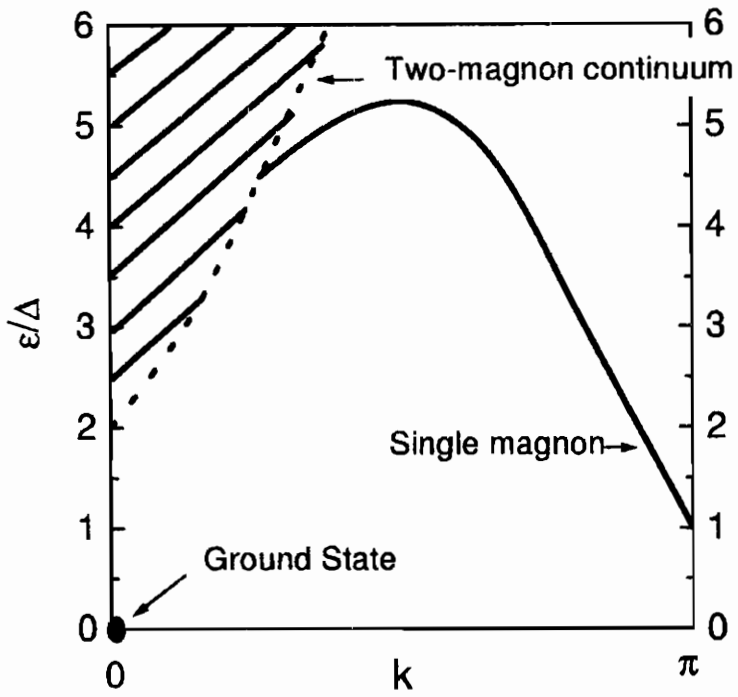

Figure 3.11: Schematic spectrum of low-lying states for the $S = 1$ HAF chain. The shape of the three degenerate single-magnon dispersion curves is based on Monte Carlo calculations [Takahashi 88, Takahashi 89]. The continuum is derived by considering the two-particle states formed by pairs of non-interacting one-magnon excitations.

mum energy $\epsilon = 2\Delta_H$ (neglecting interactions) at $k = 0$ [4]. Single-ion anisotropy (and external field) slightly modify this picture in Y_2BaNiO_5, by introducing a splitting between the levels of the order of $D \approx 10K$ ($\approx g\mu_B H_0$) [5]. These effects will be neglected here, since the energy corrections that they introduce are much smaller than the Haldane gap.

Only transition between states whose energy difference is close to the nuclear Zeeman splitting $\hbar\omega_N$ are involved in the nuclear

[4] n-magnons states with $n > 2$ [White 93] are not considered here. Their contribution to the spin dynamics is expected to be relevant only at energies larger than $3\Delta_H$.

[5] The effect of single-ion anisotropy in Y_2BaNiO_5 around $k = \pi$ is sketched in Fig. 3.2.

relaxation (Eq. (2.16)). Since $\Delta_H \approx 10^5 \hbar\omega_N$, direct process (creation/annihilation of one magnon) cannot produce nuclear spin flips. Then higher-order processes must be considered. In Fig. 3.12 the simplest multimagnon scattering events, involving almost-zero energy transfer are illustrated[6]. The number of these transitions taking place per time unit controls the intensity of the dynamical structure factor $S^{\alpha\beta}(q,\omega_N)$ at the nuclear Larmor frequency.

The spin-lattice relaxation rate $1/T_1$ is related to $S^{\alpha\beta}(q,\omega_N)$ by the form factor $\hat{A}_q$ (Eq. (2.21)). In Y_2BaNiO_5, $\hat{A}_q$ is well approximated by the scalar interaction $\hbar\gamma A$ defined by Eq. (3.4), that is q-independent since arises from *nnn*-ions which are uncorrelated. Then expression (2.21) can be rewritten

$$\frac{1}{T_1} = \hbar\gamma^2 A^2 \sum_q S^{\pm}(q,\omega_N)\,, \tag{3.10}$$

where $S^{\pm}(q,\omega_N) = \mathcal{N}^{-1} \int_{-\infty}^{+\infty} dt e^{-i\omega_N t} < \{S_q^+(t)\ ,\ S_{-q}^-(0)\} >$ is the part of the dynamical structure factor involving only $\Delta(\mathcal{S}^z) = \pm 1$ transitions. By comparing the experimental data in Y_2BaNiO_5 (Eq. (3.9)) to Eq. (3.10), one deduce that

$$\sum_q S^{\pm}(q,\omega_N) \propto e^{-\frac{\Delta_{dyn}}{T}} \tag{3.11}$$

in the temperature range $\Delta_H/2 \leq T \leq 3.5\Delta_H$. The processes bringing the dominant contribution to $\sum_q S^{\pm}(q,\omega_N)$ are easily identified in the $\Delta(\mathcal{S}^z) = \pm 1$ transitions occurring between the bottom of the two-magnons continuum and the single magnon dispersion curves (three-magnon scattering), and in the ones occurring inside the two-magnon continuum (four-magnon scattering). Both these mechanisms require in fact a minimal thermal activated energy $\Delta_{dyn} \approx 2\Delta_H$.

Relation (3.11) is believed to express a general condition for spin liquids. The NMR results obtained in the gapped spin ladder $Cu_2(C_5H_{12}N_2)_2Cl_4$ [Chaboussant 97, Chaboussant 98] support

[6]Two- and three-magnons processes have been considered in discussing nuclear relaxation in classical ($3D$) antiferromagnets with anisotropy-gaps [Moriya 56, Beeman 68], and in the analysis of the same problem in $S = 1$ chains [Jolicœur 94, Sagi 96] and two-leg ladders [Troyer 94, Sandvik 96, Ivanov 99, Melzi 99, Naef 99]. Four-magnons processes are mentioned by Chaboussant et al. in the review paper [Chaboussant 98].

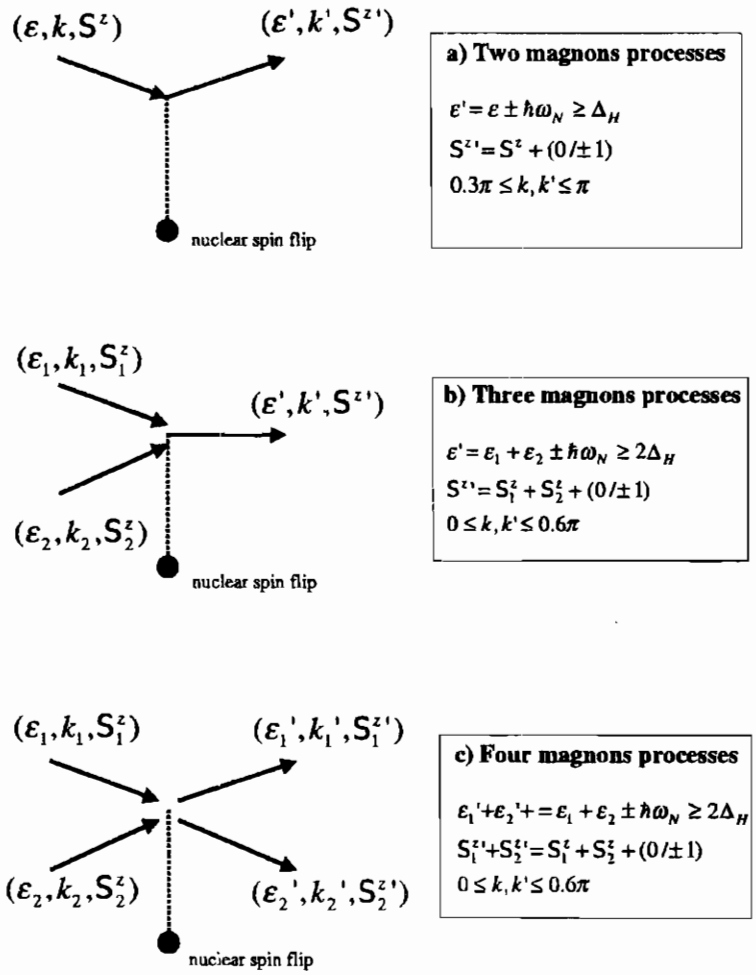

Figure 3.12: Multimagnon-scattering processes contributing to nuclear relaxation. The energy differences between incoming and outcoming magnons corresponds to the nuclear Zeeman splitting. The value of the total exchanged momentum $q = |k' - k|$ is limited by the k-crossover-points between n-particle and $(n+1)$-particle states (see [White 93]. It is noted that, strictly, $\mathcal{S}^z$ is not a good quantum number for the eigenstates of the hamiltonian (3.1) when $E \neq 0$. However, since in Y_2BaNiO_5 $E \simeq 10^{-3}J$, $\mathcal{S}^z$ can still be used, with good approximation, to label the magnetic levels.

this idea, even if the conclusions about $S^{\pm}(q,\omega_N)$ reached by the authors are somewhat less general. In $Cu_2(C_5H_{12}N_2)_2Cl_4$, the contributions to $S^{\alpha\beta}(q,\omega_N)$ coming from fluctuations parallel and orthogonal to the direction of the external field have been resolved, by measuring T_1 at two proton sites characterized by different form factors. Both turn out to be thermally activated, the first one with a gap $\Delta_{dyn} \approx \Delta_H$ and the latter with $\Delta_{dyn} \approx 2\Delta_H$, according to Eq. (3.11). However in the experiment reported in [Chaboussant 97], the two-magnons processes with $\Delta(\mathcal{S}^z) = \pm 1$ are depressed by the application of an external field comparable to Δ_H. From ^{89}Y $1/T_1$ in Y_2BaNiO_5 one deduces that, even when the different one-magnons branches overlap in the energy spectrum, the $\Delta(\mathcal{S}^z) = \pm 1$ two-magnons scattering contributions to $S^{\pm}(q,\omega_N)$ are negligible compared to the ones involving the continuum of states at $k \simeq 0$. This is similar to what occurs in $3D$-ordered AF's with a gap induced by single-ion anisotropy [Beeman 68].

In conclusion it is observed that, even if in general the spin-lattice relaxation rates in quantum disordered AF's roughly follow a temperature activated behavior (see [Gaveau 90, Fujiwara 93, Shimizu 95, Takigawa 96, Reyes 97, Tedoldi 99b] for $S = 1$ chains and [Azuma 94, Chaboussant 97, Carretta98, Imai 98] for two-leg ladders), the value of the gap extracted from $1/T_1$ is connected to the energy separation between the lowest lying states in a complicated way. The nuclear relaxation rates provides important insights about the electronic mechanisms which dominates the low energy spin dynamics, but can hardly be used, by themselves, to obtain the value of the energy gaps occurring in quantum spin systems.

Chapter 4

Staggered magnetization from spinless impurities: an imaging in $Y_2BaNi_{1-x}Mg_xO_5$

Partial substitution of magnetic ions by nonmagnetic impurities breaks an ideal Haldane system in a collection of $S = 1$ AF chains of finite length. In this Chapter the main properties of finite-chain models, obtained from analytical and computational analysis, are first recalled. It is shown how a non-uniform magnetization, reflecting the correlation properties of the system, is expected to take place. Experimental evidences confirming this prediction, based on magnetic susceptibility and ^{89}Y NMR spectra in $Y_2BaNi_{1-x}Mg_xO_5$ are then reported. In particular, a mapping between resolved NMR lines and lattice positions is established, providing an "image" of the staggered moments that develop at the chain boundaries (namely around Mg impurities). The most relevant conclusions derived from this analysis are the following. *a)* While the magnetization at sites far from the boundaries behaves as in typical gapped systems, the edge spins exhibit a $S = 1/2$ *Curie-like* deviation. *b)* The amplitude of induced moments decreases exponentially away from the edges, with a characteristic decay distance close to the magnetic correlation length of the infinite chain. These study highlights the potentialities of NMR in accessing the local response of low-dimensional AF spin systems doped by nonmagnetic impurities.

4.1 Finite $S = 1$ AF chains: basic theoretical aspects

An intuitive way to understand how boundaries modify the magnetic properties of the $S = 1$ chain starts from the $AKLT$ model. As mentioned in Section 1.4.2, the eigenspace of a spin-1 (at a given site) can be written as a symmetric combination of the eigenfunctions associated with two spin-1/2. Then the ground state $|\psi_{VBS}\rangle$ of the hamiltonian (1.29) (the "Valence Bond Solid") is expressed as a superposition of local singlets formed by two $S = 1/2$ states on adjacent sites (Fig. 4.1). With periodic boundary conditions, all the spin-1/2 are involved in dimers and $|\psi_{VBS}\rangle$ is a nondegenerate singlet. Instead, the chain with open boundary conditions (in the following "open chain") has a fourfold degenerate ground-state consisting of a singlet ($|0\rangle_o$) and a triplet ($|1, \mathcal{S}^z\rangle_o$). This can be understood by observing that the open chain is equivalent to the periodic one with one coupling removed (Fig. 4.1). Hence, an open chain has two additional spin-1/2 degrees of freedom (one at each

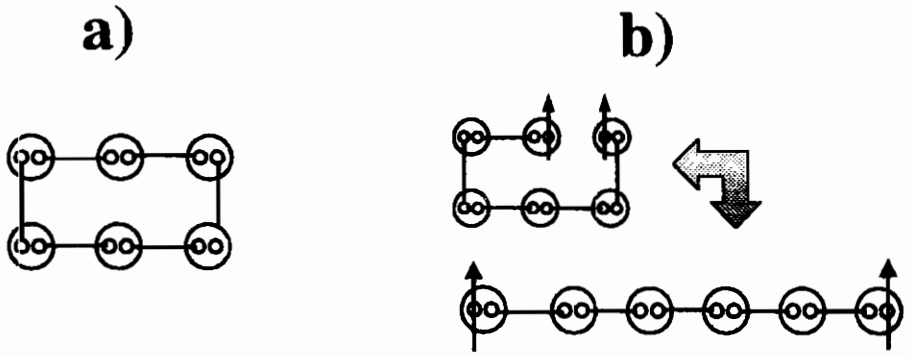

Figure 4.1: Schematic illustration of the Valence Bond Solid state for: **a)** periodic boundary conditions; **b)** open boundaries. Small circles correspond to spin-1/2 states, while the large ones denote spin-1 sites. The links between spin-1/2 on adjacent sites indicate the singlet-bonds. The equivalence between the periodic chain with one broken bond and the open one is illustrated. The additional spin-1/2 degrees of freedom characterizing the open chain are represented by arrows.

end), which combine to give a singlet and a triplet [Kennedy 90].

Let us now leave the $AKLT$ for the Heisenberg model. Formally this corresponds to vary β in the hamiltonian (1.30) from $\beta = -1/3$ to $\beta = 0$. The states $|0\rangle_o$ and $|1, S^z\rangle_o$ are no longer degenerate for $\beta \neq -1/3$: the energy separation between them increases for

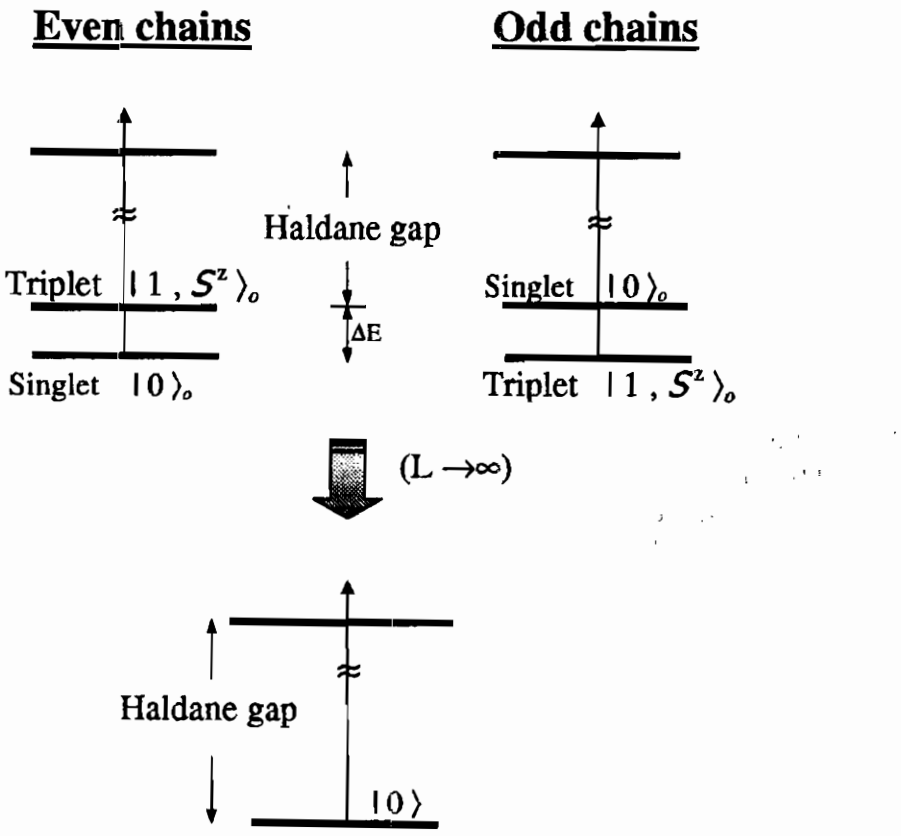

Figure 4.2: Structure of the low-energy eigenvalues for the $1D$-HAF with open boundary conditions. The difference between chains with even and odd number of spins and the evolution towards the thermodynamic limit are illustrated.

$\beta \to 0^-$ [1]. The respective positions of $|0\rangle_o$ and $|1, \mathcal{S}^z\rangle_o$ in the energy scale are fixed by the even or odd number of spins in the magnetic system: for an Heisenberg open chain with even number of spins, $|0\rangle_o$ remains the unique ground state while $|1, \mathcal{S}^z\rangle_o$ becomes the first excited level, and *vice versa* for a chain with odd number of spins [Lieb 62] (see Fig. 4.2).

The energy separation ΔE between singlet and triplet states vanishes exponentially as a function of chain length L. As observed in [Kennedy 90], this picture does not contradict Haldane's prediction of a *nondegenerate* ground state and gapped excitations for the infinite-L chain, but rather suggests to define the Haldane gap for the open chain as the difference between the second and the third energy eigenvalues (Fig. 4.2). The four states ($|0\rangle_o$; $|1, \mathcal{S}^z\rangle_o$), in fact, are the same except for boundary effects, and are thus expected to yield the same ground state for $L \to \infty$.

The difference between the four low-lying states shows up in the expectation value $\langle S_i^z \rangle_o$ of the local spin operator: $\langle S_i^z \rangle_o$ is zero (at all sites) in the states $|0\rangle_o$ and $|1, 0\rangle_o$, while it takes non-zero and site-dependent values in $|1, 1\rangle_o$ and $|1, -1\rangle_o$. According to Quantum Monte Carlo [Miyashita93] and Density Matrix Renormalization Group results [White 92, Sorensen 94, Polizzi 98], one has $\langle S_{i=1}^z \rangle_o = \langle S_{i=L}^z \rangle_o \simeq 1/2$ in the state $|1, 1\rangle_o$. Then, going towards the center of the chain, $\langle S_i^z \rangle_o \to 0$ with sign alternating from site to site (Fig. 4.3). Due to the arbitrary choice of the z-axis in the Heisenberg model, it must be $\langle 1, -1 | S_i^z | 1, -1 \rangle_o = -\langle 1, 1 | S_i^z | 1, 1 \rangle_o$.

Fitting $|\langle S_i^z \rangle_o|$ to an exponential function, provides the characteristic decay length $\xi \simeq 6$ of the boundary "anomaly"[2]. This value is remarkably close to the correlation length ξ_∞ of the infinite Haldane chain at zero-temperature, suggesting that the behavior of S_i^z in the state $|1, 1\rangle_o$ (and in $|1, -1\rangle_o$) reflects the decay of the cor-

[1] Actually, for $\beta \to 0^-$, not only the energies are changed, but also the state $|0\rangle_o$ and $|1, \mathcal{S}^z\rangle_o$ themselves are progressively modified. However they still remain singlet and triplet eigenfunctions of the total spin $\mathcal{S}$. For this reason, the same notation used above is retained.

[2] It is worth to remark that the decay of $|\langle S_i^z \rangle_o|$ in the state $|1, 1\rangle_o$ observed in the numerical data (Fig. 4.3) *is not* strictly exponential. $|\langle S_i^z \rangle_o|$ is somewhat larger than the interpolating exponential at odd sites and smaller at even sites, as can be noted in the logarithmic plots reported in [White 92, Miyashita93, Sorensen 94]. These deviations ensure that the total spin on half chain is $\sum_i \langle S_i^z \rangle_o = 1/2$, as it must be in a $\mathcal{S}^z = 1$ state. Instead, for a pure staggered-exponential decay ($\langle S_i^z \rangle_o = \langle S_1^z \rangle_o (-1)^{(i-1)} e^{-(i-1)/\xi}$, with $\langle S_1^z \rangle_o = 1/2$ and $\xi = 6$), one would have $\sum_i \langle S_i^z \rangle_o \simeq 0.25$ for each half-chain, that is clearly inconsistent in the state $|1, 1\rangle_o$.

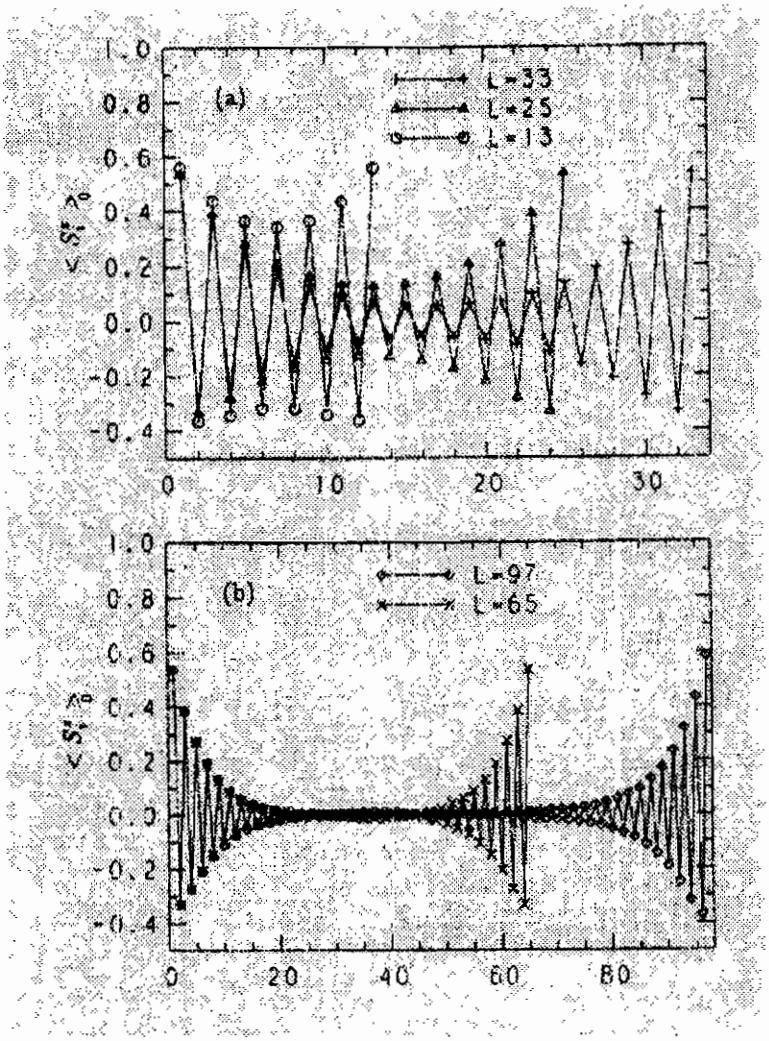

Figure 4.3: S_i^z expectation value in the state $|1,1\rangle_o$, for open chains with different length L (from Ref. [Miyashita93]).

relation function in the Haldane phase. Analogous conclusion has been reached by Sorensen and Affleck in a field theory approach [Sorensen 94].

The expectation value of the local spin operator S_i^z in the state

$|1,1\rangle_o$ is often defined in literature as "local magnetization", or "on-site magnetization". However such definition is rigorous only at zero-temperature, if $|1,1\rangle_o$ is the unique ground state. This occurs for odd chains in a small uniform field, as well as for even chains when the field is strong enough to induce a Zeeman splitting of the triplet larger than $\Delta E(L)$. In general, at finite temperature, the local magnetization $\langle S_i^z \rangle$ is defined as the statistical average of the S_i^z operator (Eq. (2.7)). In the limit $T << \Delta_H$, only the four lowest lying states are involved in the average, but at higher temperature one has to take into account also the states above the Haldane gap and the calculation of the local magnetization becomes much more complicated. We will come back to this issue in the last Section, after having presented a direct experimental determination of $\langle S_i^z \rangle$.

4.2 Nonmagnetic-impurity doping in Y_2BaNiO_5

In order to carry out experimental studies on the local magnetization $\langle S_i^z \rangle$ occurring in finite $S = 1$ chains, polycrystalline samples of $Y_2BaNi_{1-x}Mg_xO_5$ at $x = 0.05$ and $x = 0.10$, have been prepared as described in Appendix. X-Ray diffraction shows that the Mg-doped compounds preserve the original symmetry of Y_2BaNiO_5 (without significative changes in the lattice constants), and that Mg ions substitute Ni in peer positions, for an amount practically equal to the nominal doping.

The nonmagnetic ($S = 0$) Mg^{2+} ions are equivalent to spin-vacancies along the Ni-O-Ni chains (Fig. 4.4). Although one cannot exclude, in principle, that a small interaction between Ni ions separated by a Mg-impurity could survive, this is expected to be very small compared to J and will be neglected. Thus, the compound $Y_2BaNi_{1-x}Mg_xO_5$ is considered as a sequence of open chains, with average length proportional to the inverse of the doping x. For a random arrangement of defects, the distribution $P(L)$ of chain-lengths in the sample is given by the probability of finding one Mg-ion *and* L non-substituted Ni sites, i.e.

$$P(L) = x(1-x)^L \ . \tag{4.1}$$

The average length of the chains in a x-doped sample is thus

$$\langle L \rangle = \sum_0^\infty L\, x(1-x)^L = \frac{1}{x} - 1 \ , \tag{4.2}$$

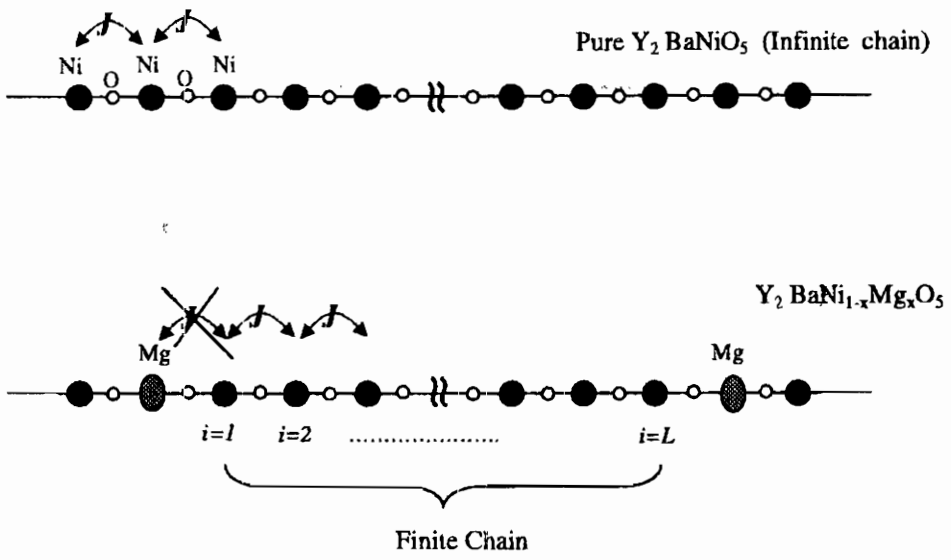

Figure 4.4: Schematic picture of the Ni-O-Ni chains in Y_2BaNiO_5, before and after Mg-doping.

as expected. For $x = 0.05$ and $x = 0.10$ (the samples studied here), one can assume $\langle L \rangle \simeq 1/x$.

It is noted that, since $P(L)$ decreases monotonically as a function of L, the short chains play a non negligible role in the L-averaged quantities, even at low doping.

4.3 Experimental results

4.3.1 Magnetic susceptibility

$Y_2BaNi_{1-x}Mg_xO_5$ magnetization have been measured by SQUID magnetometer[3]. As for the pure compound, the magnetization curves are linear up to $\simeq 7T$ and no difference between field-cooled and zero-field-cooled conditions has been detected down to $T = 2K$

[3]QUANTUM DESIGN SQUID (type MPMS-XL7), equipped by 7T magnet and operating in the range 1.8 - 800 K, installed at the *Department of Physics "A. Volta" - University of Pavia.*

(Fig. 4.5).

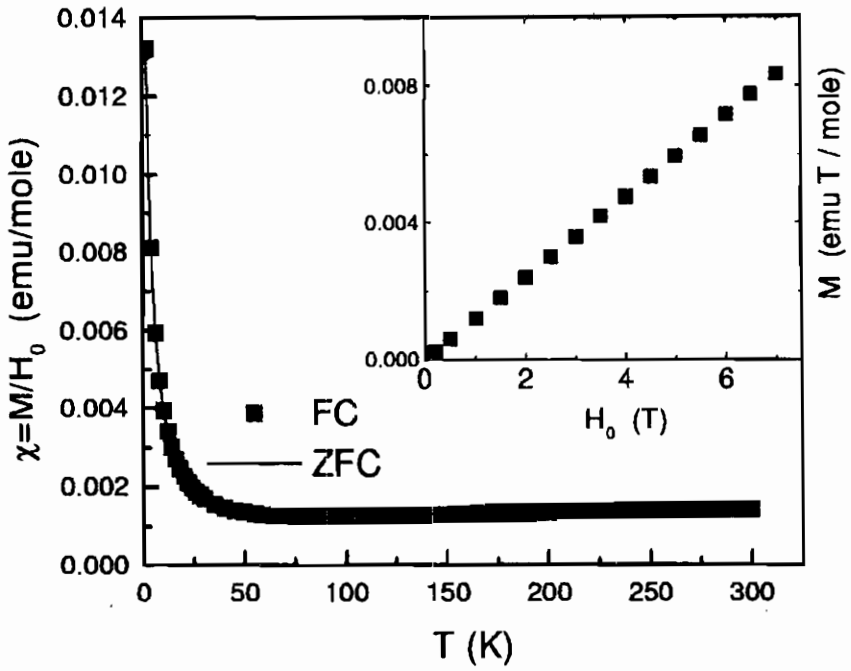

Figure 4.5: Field-cooled (FC) and zero-field-cooled (ZFC) magnetic susceptibility in $Y_2BaNi_{0.95}Mg_{0.05}O_5$. In the inset a typical magnetization curve is reported (T=300K).

The susceptibility $\chi(T) = M/H_0$ is reported as a function of temperature in Fig. 4.6, for both $x = 0.05$ and $x = 0.10$ samples, and compared with nominally pure Y_2BaNiO_5 ($x = 0$). χ increases on increasing the Mg amount, indicating that spinless impurities induce extra magnetic moments in the Haldane system, in agreement with the theoretical predictions discussed above. This also suggests that the Curie-like contribution observed in the pure compound can actually be attributed to the finite size of the Ni-O-Ni chains arising from naturally occurring defects.

However, macroscopic susceptibility is not the ideal tool in order to investigate "modulated" effects, like those expected in open chains, since it probes uniform ($q = 0$) contributions. χ measures the total magnetic moment which aligns along the external field ($\chi \propto \sum_i \langle S_i^z \rangle$), but cannot clarify how $\langle S_i^z \rangle$ depends on the position along the chain. Only a local probe sensitive to spatial oscillations of $\langle S_i^z \rangle$, such ^{89}Y NMR, can provide a direct picture of the on-site magnetization.

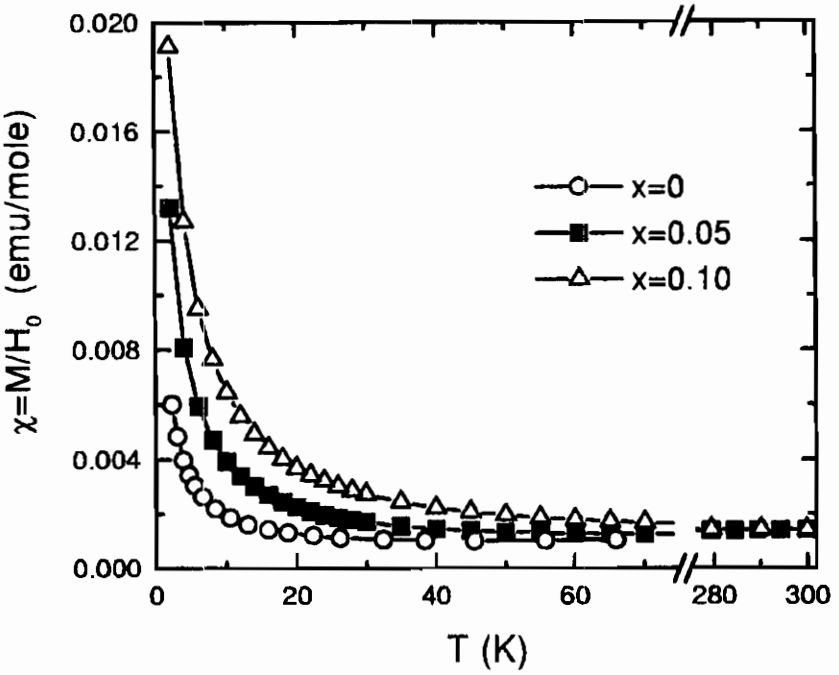

Figure 4.6: Magnetic susceptibility in $Y_2BaNi_{1-x}Mg_xO_5$.

4.3.2 ^{89}Y NMR spectra

^{89}Y NMR spectra have been measured in $Y_2BaNi_{1-x}Mg_xO_5$ at fixed frequency ν_{RF} by sweeping the magnetic field H_0 [4]. This procedure is equivalent (when small changes in H_0 do not modify the intrinsic properties of the system, which is the case here), to vary step by step the irradiation frequency at fixed field. However, it turns out more efficient in measuring complex distribution of resonance frequencies, since it does not require any retuning of the NMR setup during the acquisition of the spectrum.

In Fig. 4.7 representative spectra for the $x = 0.05$ sample are shown. At $T \geq 100K$, several peaks are observed, their shift from the central line increasing with decreasing temperature. In order to resolve the multipeak structure, each spectrum has been obtained by summing the Fourier transforms of the echo signals recorded at about $50 \div 100$ different values of H_0. The peaks p_I are labelled by an index I according to the decreasing magnitude of their

[4]Experiments performed at GHMFL (Grenoble High Magnetic Field Laboratory), by a home-made 1 GHz spectrometer equipped with variable-field 17 T OXFORD superconducting magnet.

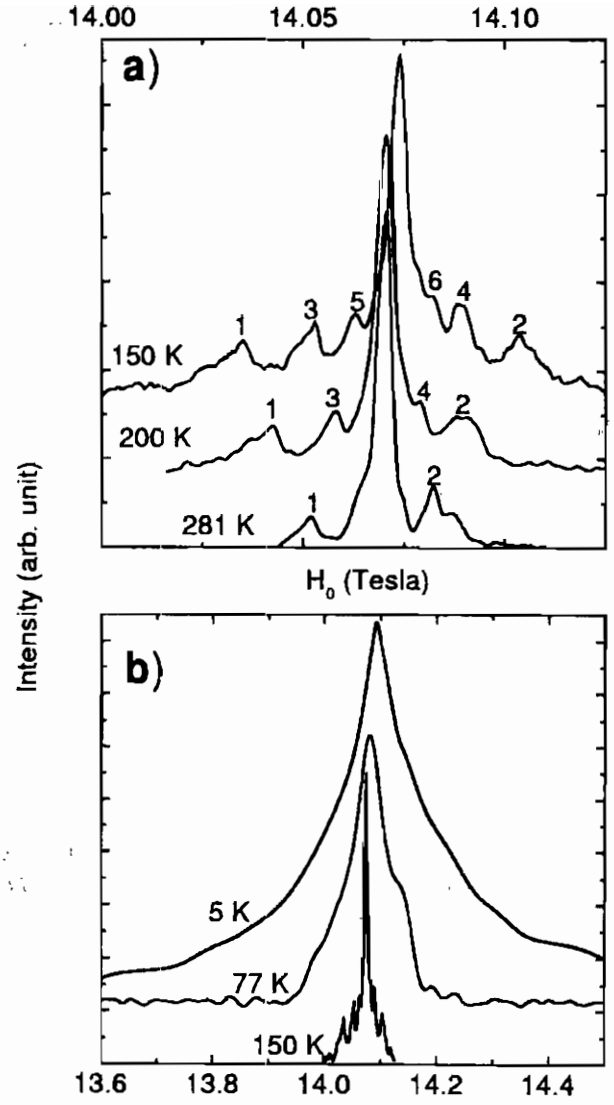

Figure 4.7: ^{89}Y NMR spectra in $Y_2BaNi_{0.95}Mg_{0.05}O_5$ recorded at fixed frequency $\nu_{RF} = 29.4MHz$ upon sweeping the magnetic field H_0 (from Ref. [Tedoldi 99c]). **a)** For $T > 100K$ resolved satellite peaks are labelled with an index I, following the decreasing magnitude of their shifts from the central line (see text). **b)** Below $T \simeq 100K$, the different peaks are no longer resolved. The spectra consist in single broad lines (the spectrum at $T = 150K$ is plotted again for comparison).

that the relative shifts $\Delta(p_I)$ scale linearly with ν_{RF} and thus with

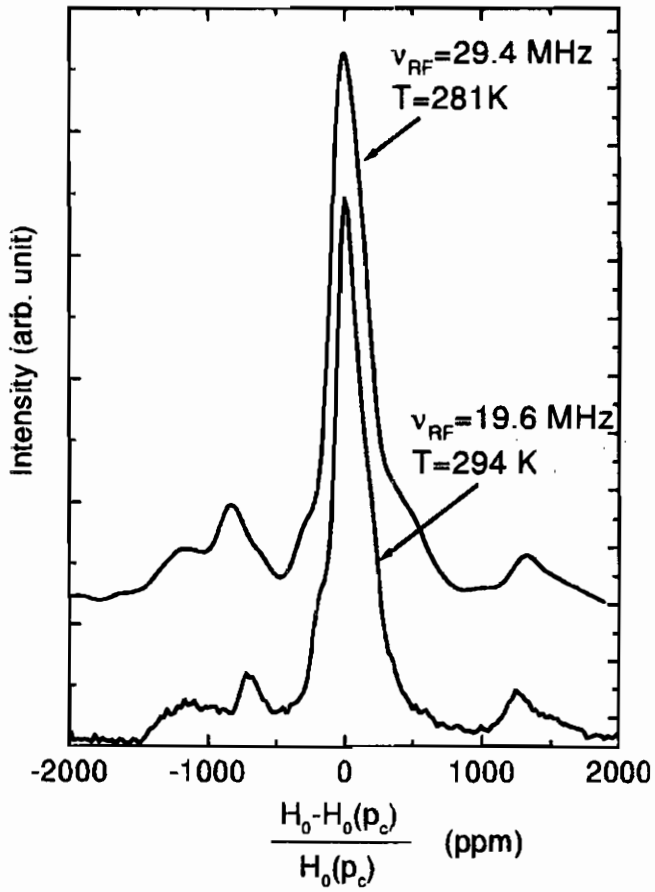

Figure 4.8: Spectra in $Y_2BaNi_{0.95}Mg_{0.05}O_5$ at $T \approx J(= 285K)$, for two values of the irradiation frequency. The almost-unchanged position of the satellites peaks indicates that the relative shifts $\Delta(p_I)$ scale linearly with ν_{RF} and thus with the external field H_0 (the small variation is due to the $13K$-difference between the two spectra).

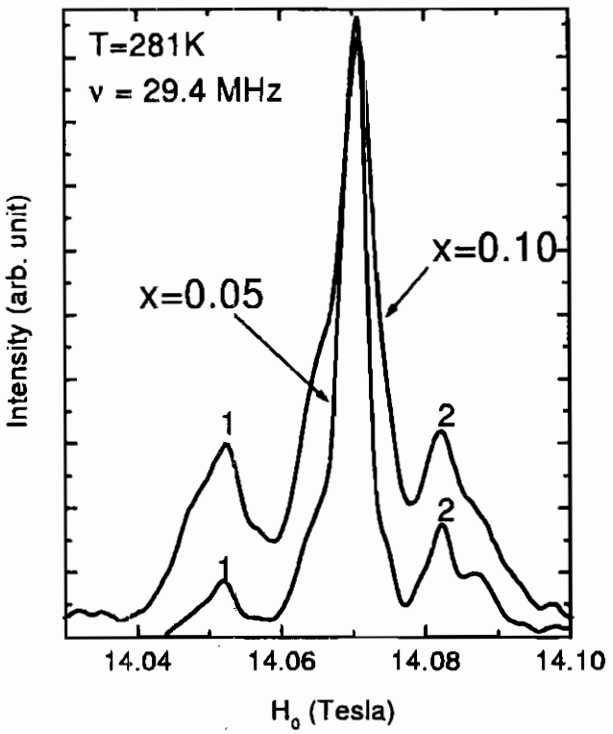

Figure 4.9: Comparison, at $T \simeq J$, of the ^{89}Y spectra in the $x = 0.05$ and $x = 0.10$ samples, corresponding to $\langle L \rangle \simeq 20$ and $\langle L \rangle \simeq 10$ (from Ref. [Tedoldi 99c]).

the external field H_0. A comparison between samples at different doping (Fig. 4.9) proves that, for $T \simeq J$, the peak positions are independent on $\langle L \rangle$.

Finally, in Fig. 4.10, the shift K of the central peak p_c with respect to the ^{89}Y reference signal is reported. K has been determined from the difference between the resonance frequency correspondent to the maximal intensity in p_c and the ^{89}Y frequency in YCl_3 solution, at fixed H_0 [5]. Possible errors resulting from the estimate of the absolute value of H_0 are, in this way, avoided.

[5]High-resolution 9.4 T superconducting magnet in permanent-mode (Centro Grandi Strumenti - University of Pavia) has been used.

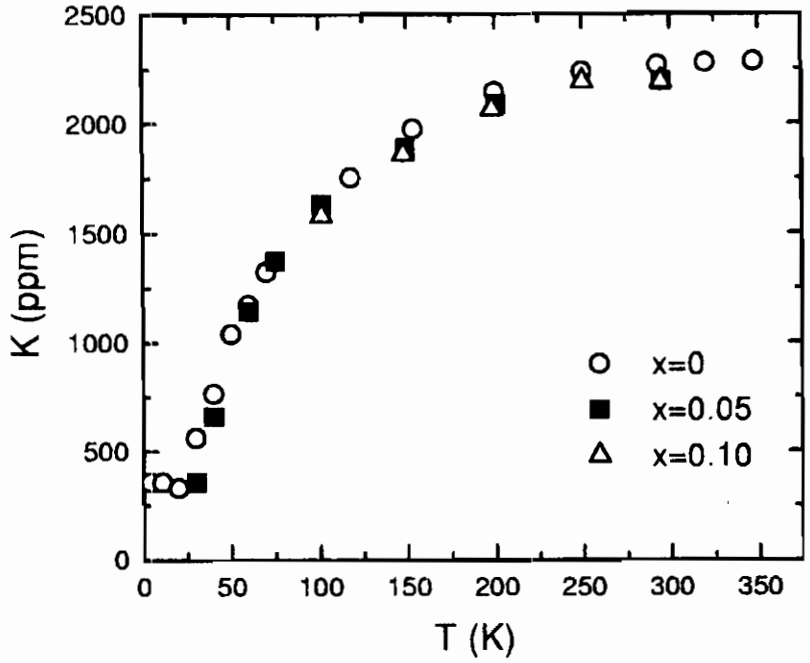

Figure 4.10: Shift of the central peak p_c in the $Y_2BaNi_{1-x}Mg_xO_5$ spectra, with respect to the reference ^{89}Y signal in a YCl_3 solution.

4.4 Local magnetization, edge spins and magnetic correlations

According to the expressions (3.4) and (3.5), the hyperfine field at a given ^{89}Y site in $Y_2BaNi_{1-x}Mg_xO_5$ is proportional to the local magnetization of the two next nearest neighbor (nnn) Ni^{2+} ions (see Fig. 3.8). Thus, for a fixed frequency ν_{RF}, the resonance condition is

$$\nu_{RF} = \frac{\gamma}{2\pi}\left[H_0 + A\left(\langle S_i^z\rangle + \langle S_{i'}^z\rangle\right)\right] \quad , \tag{4.3}$$

where $A = 13KG$ and the indexes i, i' indicate the position of the two nnn in the correspondent finite chains limited by two Mg impurities. The high temperature spectra shown in Fig. 4.7a) find an immediate interpretation in the light of Eq. (4.3). The central peak p_c corresponds to ^{89}Y nuclei resonating at almost the same field, indicating that most of the Ni^{2+} spins have approximately the same expectation value $\langle S_c^z\rangle$. On the other hand, the occurrence

of small satellites peaks p_I points out that, for a certain number of Ni^{2+} ions, $\langle S_i^z \rangle$ and/or $\langle S_{i'}^z \rangle$ are different from $\langle S_c^z \rangle$.

The small interchain coupling J' allows us to consider the thermal expectation values of the nnn spins (which belong to different chains) completely uncorrelated. The most probable random combinations of $\langle S_i^z \rangle$ and $\langle S_{i'}^z \rangle$, a part for the one in which both are equal to $\langle S_c^z \rangle$, are those with $\langle S_i^z \rangle = \langle S_c^z \rangle$ and $\langle S_{i'}^z \rangle \neq \langle S_c^z \rangle$ (and *vice versa*). Thus the peaks p_I in the ^{89}Y spectra must be related to these latter situations, each of them identifying a defined value of $\langle S_i^z \rangle$.

The explicit form of the mapping between the site-index i and the peak-label I is suggested by the evolution of the spectra as a function of the impurity concentration x. The satellites peaks are reduced on increasing x (Fig. 4.9), and disappear for $x = 0$, while the central line p_c remain almost the same. This indicates that the peaks p_I are associated to spins at the boundaries of the chains, while p_c reflects the properties of the "bulk". At this point, it is logical to relate the magnitude of the shift $\Delta(p_I)$ in the spectra to the distance of the ions from the center of the chain and to assign the peaks p_I to the positions $i = I$ and $(i = L - I + 1)$ following the decreasing strength of $\Delta(p_I)$ (Fig. 4.11). According to this mapping, the magnetization induced by impurities is

$$\Delta\langle S_I^z \rangle \equiv \langle S_I^z \rangle - \langle S_c^z \rangle = \frac{\Delta(p_I)}{A} , \tag{4.4}$$

with $I = 1, \ldots . L/2$. The regular alternation of the sign of $\Delta(p_I)$ as a function of I points out the staggered nature of induced magnetization, which reflects the AF character of the exchange coupling.

Let's go now to study the temperature evolution of the induced magnetization at the first (and last) site of the chain. As shown in Fig. 4.12, the values of $\Delta\langle S_{I=1}^z \rangle$, extracted by the experimental data at $H_0 \simeq 14.1T$ (Fig. 4.7a)) through Eq. (4.4), are well accounted for by the law

$$|\Delta\langle S_{I=1}^z \rangle| = \frac{g\mu_B H_0 S(S+1)}{3k_B T} \tag{4.5}$$

with $S = 1/2$, $g = 2$. This means that, for $\Delta_H \leq T \leq J$ (where $\Delta_H \approx 100\,\mathrm{K}$ is the Haldane gap for pure Y_2BaNiO_5), the non-uniform magnetization associated to the extreme sites of the chain is close to the one corresponding to "free" $S = 1/2$ spins. The

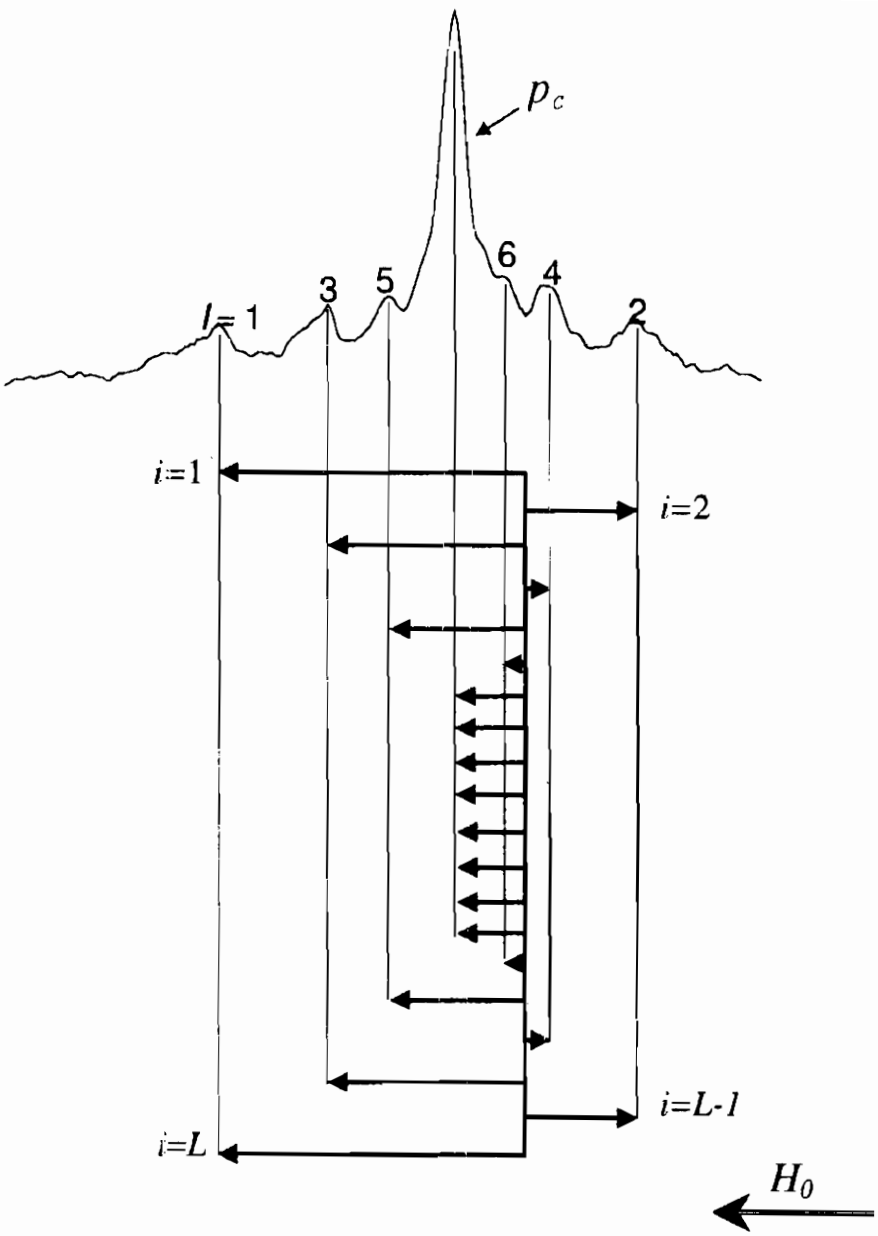

Figure 4.11: Schematic illustration of the mapping between NMR peaks and chain's sites described in the text.

linear scaling of $\Delta\langle S^z_{I=1}\rangle$ (and thus of $\Delta(p_I)$) as a function of H_0, predicted by Eq. (4.5), has been verified at room temperature (Fig. 4.8). Moreover, still at room temperature, no doping (*i.e.*, $\langle L\rangle$-) dependence of $\Delta(p_1)$ have been found (Fig. 4.9), indicating that, for $T \simeq J(= 285K)$, Eq. (4.5) holds independently on the chain-length up to $\langle L\rangle \geq 10$.

The behavior of $\Delta\langle S^z_{I=1}\rangle$ given by Eq.(4.5) could be obtained by extrapolating at high temperature the expectation value of the edge spins calculated by using only the lowest energy states (singlet and triplet) of the finite chain, provided they are degenerate. This suggests that the excited states above the Haldane gap do not play

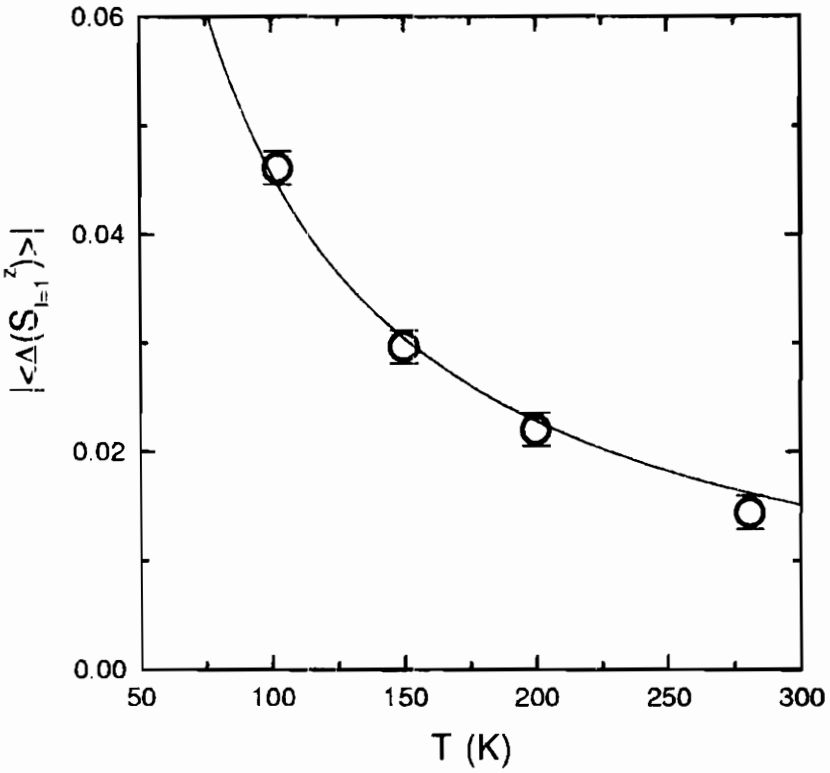

Figure 4.12: Temperature dependence of the impurity-induced magnetization at the edge sites ($I = 1$), as deduced by the shift of the peak $p_{I=1}$ in Fig. 4.7, through Eq. (4.4). The solid line is a Curie function for $S = 1/2$ spins in $H_0 = 14.1T$ (Eq. (4.5) in the text).

an important role in the staggered magnetization at sites $I = 1$. Instead, as it appears from the analysis of the spin-spin correlation reported in the following, the levels above Δ_H substantially affect $\Delta\langle S_I^z\rangle$ for $I \neq 1$.

Fig. 4.13 a) reports the I-dependence of $|\Delta\langle S_I^z\rangle|$ extracted from the shifts $\Delta(p_I)$ in $Y_2BaNi_{0.95}Mg_{0.05}O_5$, at $T > 100K$. $|\Delta\langle S_I^z\rangle|$ is well fitted, at all temperature, by the exponential law

$$|\Delta\langle S_I^z\rangle(T)| = |\Delta\langle S_{I=1}^z\rangle(T)|\, e^{-(I-1)/\xi(T)}\,, \qquad (4.6)$$

which provides the characteristic decay length $\xi(T)$ of the impurity-induced magnetization. As shown in Fig. 4.13 b), $\xi(T)$ obtained in this way is very close to the values of the infinite-chain correlation length ξ_∞ calculated by Kim *et al.* [Kim 98]. This indicates that the picture of boundary defects, which reflects the bulk correlation of an infinite chain, holds not only in the Haldane phase ($T < \Delta_H$) [Polizzi 98], but also for $\Delta_H \leq T \leq J$.

At low temperature the progressive increase of the width of the NMR peaks (see Fig. 4.7) prevents a meaningful analysis of the boundary magnetization through the direct method used for $T \geq$ 100 K. However, the characteristic shape of the NMR spectra clearly indicates the persistence of field-induced staggered magnetization. The origin of the broadening, which lead the multipeak structure to merge into a broad line on decreasing temperature, is likely related to the distribution of chain lengths around the average value $\langle L\rangle$, as discussed in the next Section.

Let us finally observe how the magnetization at sites far from the edges is practically unaffected by the finite size in the $x = 0.05$ compound (Fig. 4.10). This indicate that the Haldane gap (defined for the open chain in Section 4.1) already takes for $\langle L\rangle \simeq 20$ its thermodynamic value $\Delta_H \simeq 100K$. In a sense, such conclusion is not surprising. The correspondence $\xi \leftrightarrow \xi_\infty$ established above in fact, suggests that the extension of boundary-defects is always less the $\xi_\infty(T = 0) \simeq 6$. So, in a chain of about 20 sites, there are a number of central ions which "never know that the system is finite". In the same spirit, one expects that $K(T)$ in the $x = 0.10$ sample tracks the temperature behavior of the lineshift in pure Y_2BaNiO_5 down to $T \simeq 100K$, where $\xi(T) \simeq \langle L\rangle/2 \simeq 5$. This is indeed the case, as shown in Fig. 4.10. Further studies are necessary to clarify the situation when $\xi(T)$ becomes larger than $\langle L\rangle/2$.

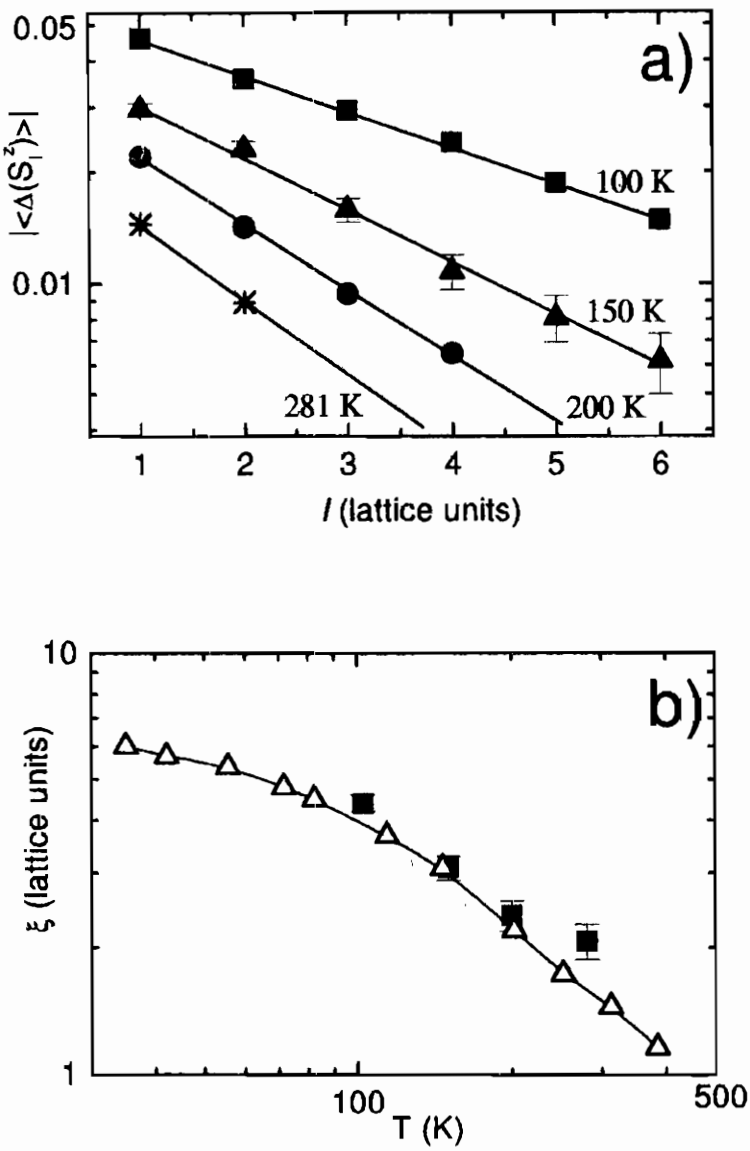

Figure 4.13: **a)** Site dependence of the staggered magnetization deduced by the shift of the satellites from the central peak in $Y_2BaNi_{0.95}Mg_{0.05}O_5$ spectra taken at $\nu_{RF} = 29.4$ MHz. Solid lines are fits (Eq. (4.6) in the text), defining the decay length $\xi(T)$ of the boundary magnetization. **b)** Comparison of the experimental $\xi(T)$ value (full squares) and the infinite chain correlation length $\xi_\infty(T)$ (up triangles) as calculated in Ref. [Kim 98].

4.5 Models for "intermediate temperature": preliminary results

The correspondence between ξ and ξ_∞ deduced from the NMR data in $Y_2BaNi_{1-x}Mg_xO_5$
has an intuitive justification. Since translational invariance is broken by impurities, it is natural to expect that the edge-spin magnetization will differ from the "bulk" value $\langle S_c^z \rangle$. Once assumed this, it seems very reasonable that $\langle S_i^z \rangle$ recovers $\langle S_c^z \rangle$ on a typical length-scale fixed by the spin-spin correlation function of the unperturbed system. However, from a formal point of view the equivalence $\xi \leftrightarrow \xi_\infty$ is hard to prove, particularly for $\Delta_H \leq T \leq J$. In this temperature range in fact, one cannot use high-temperature expansions, being too far from the paramagnetic limit $T >> J$. At the same time, low-temperature approaches neglecting the states above the Haldane gap are clearly inappropriate.

A phenomenological model, suitable to reproduce the experimental findings reported in this Chapter, has been recently proposed [Santachiara 99]. Following the idea of Sorensen and Affleck [Sorensen 94], Santachiara uses an effective field theory description for the Heisenberg hamiltonian and replaces open boundaries by an additional $S = 1/2$ degree of freedom at each end of the chain. Then the response of the system to an external magnetic field is calculated for $T \geq \Delta_H$. The interaction of the edge spins with the effective field describing the chain is shown to induce staggered magnetization, localized at the boundaries and exponentially decaying on the length-scale ξ_∞.

Another possible way to approach the problem is based on the observation that, for $T \geq \Delta_H$, the correlation properties of classical and quantum spin chains should merge [Kim 98]. Monte Carlo simulations of Heisenberg chains with open boundary conditions are in progress to evaluate site and temperature dependence of $\langle S_i^z \rangle$ in the limit $S \to \infty$ [Botti 99]. Although very preliminary, these numerical results provide a picture rather close to the one obtained from NMR in $Y_2BaNi_{1-x}Mg_xO_5$. Moreover, this computational analysis allows us to attribute the broadening observed in the peaks in Fig. 4.7, (which leads to loose the spectral resolution below $T = 100K$), to the distribution of chain lengths around the average value $\langle L \rangle$. The spread of hyperfine fields due to the L-dependence of $\langle S_i^z \rangle$, in fact, turns out of the same order of the observed linewidths.

4.6 ^{89}Y NMR in $Y_2BaNi_{1-x}Mg_xO_5$ *vis a vis* to similar experiments

Several experimental evidences of "edge states" in Haldane compounds have been reported in literature. In particular, the signal coming from impurity spins has been observed by low-temperature ESR [Hagiwara 90, Granroth 98, Kimura 98], and suggested to correspond to $S = 1/2$ degrees of freedom. Also the Schottky-like anomaly in specific heat, which at first was interpreted as due to $S = 1$ states [Ramirez 94], turns out to be explainable in terms of $S = 1/2$ excitations [Batista 98a]. However, ESR and specific heat results prove the existence of extra-levels induced by spinless impurity without resolving the site dependence of $\langle S_i^z \rangle$. By the ^{89}Y NMR study in $Y_2BaNi_{1-x}Mg_xO_5$ presented here instead, $\langle S_i^z \rangle$ has been imaged *site by site*, and its temperature evolution has been probed in a wide temperature range.

Recent studies of various low-dimensional HAF's, such as $S = 1/2$ spin chains [Takigawa 97], spin ladders [Fujiwara 98] and $2D$-cuprates [Bobroff 97, Julien 99], showed that nonmagnetic impurities induce a considerable broadening of the NMR spectra. This broadening has been attributed to the hyperfine field caused by staggered moments on sites around spinless ions. However none of these studies led to resolved spectra. Therefore, in order to obtain information on the correlation length, specific models of the spin susceptibility have been used. In the best cases, useful insights are obtained in such way, but often *model dependent*. In the present work, the real-space dependence of the spin polarization have been simply deduced by the shift of resolved satellites peaks in the NMR spectra, providing a *model independent* picture of the impurity screening, and thus giving a direct access to ξ. The power of NMR in probing the local response of low-dimensional HAF's turns out enforced by this study.

Chapter 5

The hole-doped spin liquid $Y_{2-y}Ca_yBaNiO_5$

Considerable interest has recently arisen in regards of the modifications occurring in spin liquid systems upon carrier injections. In the present Chapter this subject is investigated by magnetic susceptibility and ^{89}Y relaxation measurements in $Y_{2-y}Ca_yBaNiO_5$. Novel spin excitations, induced in the $S = 1$ chain through the heterovalent substitution $Ca^{2+} \rightarrow Y^{3+}$, are evidenced. The results from spin-lattice relaxation are consistent with a phenomenological picture of mobile holes which tend to localize, on cooling, generating effective magnetic moments in the AF-correlated background. The occurrence of these extra-moments is also detected at low temperature by homogeneous susceptibility, and the slowing down of their local fluctuations is argued to cause the dramatic enhancement in the spin-spin relaxation rate observed below $T \approx 120$K.

5.1 Introduction

The nature of the charge-defects introduced in Y_2BaNiO_5 by Ca-doping has been investigated by polarized X-ray absorption spectroscopy [DiTusa 94]. The holes are found to have mainly O-$2p_a$ character, i.e. they reside in the oxygen orbitals directed along the chain-axis a. Electric resistivity in the a-direction is strongly reduced upon Ca-doping [DiTusa 94], pointing out that extra-holes can move on the $S = 1$ chains. Then, a great deal of interest has arisen in regards of the spin dynamics associated to hole hopping.

Starting from a multiband hamiltonian including nickel and oxygen orbitals, Dagotto et al. [Dagotto 96] have derived an effective one band model for $Y_{2-y}Ca_yBaNiO_5$, using an approach similar to that proposed by Zhang and Rice to reduce the two-dimensional multiband Hubbard hamiltonian to the $t-J$ model [Zhang 88]. In Ref. [Dagotto 96], holes are described as $S = 1/2$ states at the Ni-sites propagating along the $S = 1$ chain. The magnetic structure factor evaluated in the framework of this simplified picture reveals excitations inside the Haldane gap. Batista and collaborators [Batista 98b] have somewhat criticized the model used in [Dagotto 96], and proposed a different approach starting from a 1D reduction of the van Elp Hamiltonian for NiO_6 clusters [van Elp 92]. This leads to a dynamical structure factor characterized by several peaks inside the Haldane gap, including excitations at almost zero energy.

Recent studies in Li-substituted 3D-AF NiO [Corti 97] have shown that low-energy components in the Ni^{2+} spin dynamics, induced by injected holes, can be readily detected by NMR relaxation. In particular, two maxima in ^{7}Li spin-lattice relaxation rate $1/T_1$ have been found as a function of temperature, superimposed to the background due to magnon-scattering. The peak at higher temperature was interpreted as a signature of *charge freezing*, i.e. of the slowing down, on cooling, of magnetic excitations accompanying the hole-hopping. The lower temperature peak was instead related to the local fluctuations of the effective magnetic moments induced in the AF matrix by charge-localization. Muon relaxation experiments confirmed this picture, pointing out a broad distribution of decay rates as typical in spin-glass-like systems [Tedoldi 99a].

In the light of these previous studies, ^{89}Y NMR relaxation has been used in the search of low-frequency components in the dynam-

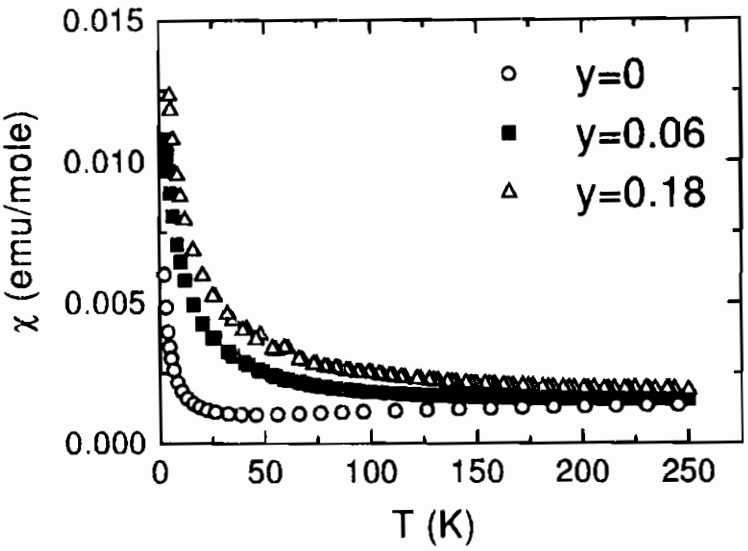

Figure 5.2: Magnetic susceptibility in $Y_{2-y}Ca_yBaNiO_5$ for different Ca-concentrations (from Ref. [Tedoldi 98]).

Standard pulse NMR techniques have been used to measure ^{89}Y relaxation times in $Y_{2-y}Ca_yBaNiO_5$[4]. The recovery of the nuclear magnetization $M_z(\tau)$ along $z//H_0$ is exponential at high temperature and turns to a multi-exponential behavior on cooling (Fig. 5.3 a) and 5.3 b)). A phenomenological stretched-exponential function of the form

$$y(\tau) \equiv \frac{M_z(\infty) - M_z(\tau)}{M_z(\infty)} = e^{-(\tau/T_1)^\beta} \tag{5.1}$$

has been used to fit the experimental data and to deduce an effective value of the spin-lattice relaxation rate (Fig. 5.3 c)).

In Ca-doped Y_2BaNiO_5, the intensity of the NMR signal is strongly reduced on decreasing temperature, preventing accurate measurements of T_1 below 100 K. This effect is due to a drastic shortening of the spin-spin relaxation time T_2 upon Ca-substitution (Fig. 5.4). T_2 represents the typical irreversible-decay time of the nuclear magnetization in the plane perpendicular to H_0 [Slichter].

[4]BRUKER spectrometers MSL200 and AMX400 equipped with 5.9 T and 9.4 T OXFORD superconducting magnets have been employed.

ical structure factor of $Y_{2-y}Ca_yBaNiO_5$. As shown in the following, ^{89}Y $1/T_1$ is increased by Ca-doping, with a maximal difference with respect to pure Y_2BaNiO_5 around 150 K. In addition ^{89}Y spin-spin relaxation rate $1/T_2$, shows a dramatic enhancement below $T \approx 120$ K. These findings indicate the onset of doping-induced spin fluctuations at very low frequency, in agreement with theoretical predictions [Batista 98b]. Magnetic susceptibility measurements have been also carried out, showing the occurrence of effective Curie-like moments at low temperature, sign of hole-localization.

5.2 Experimental results

Magnetic susceptibility (χ) has been measured by a SQUID[1] on $x = 0.06$ and $x = 0.018$ powder samples[2] of $Y_{2-y}Ca_yBaNiO_5$ between 3.5 K and 250 K.

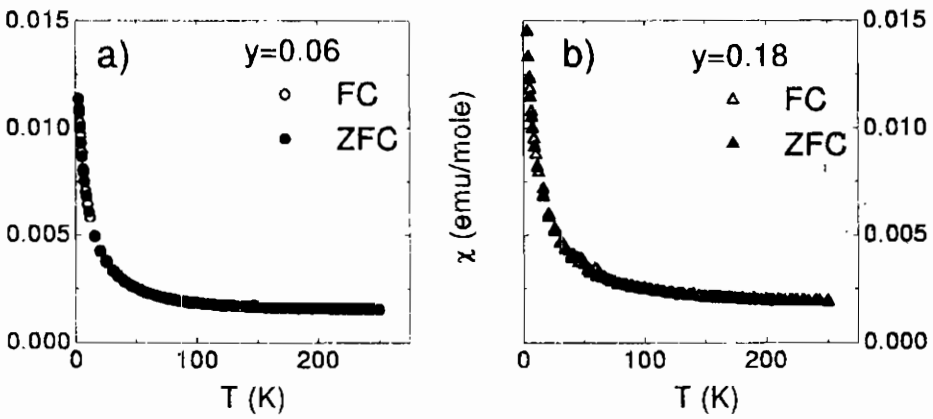

Figure 5.1: Magnetic susceptibility in $Y_{2-y}Ca_yBaNiO_5$: comparison between field-cooled (FC) and zero-field-cooled (ZFC) conditions.

χ is insensitive to the magnetic field strength at least up to 0.5T and no difference between field cooled and zero field cooled data has been detected[3] (Fig. 5.1). The susceptibility of Ca-doped compounds and of nominally pure Y_2BaNiO_5 are compared in Fig. 5.2.

[1] METRONIQUE INGEGNERIE SQUID M03.

[2] For synthesis and characterization of the samples see Appendix.

[3] History dependent susceptibility has been observed only below 3 K [Kojima 95].

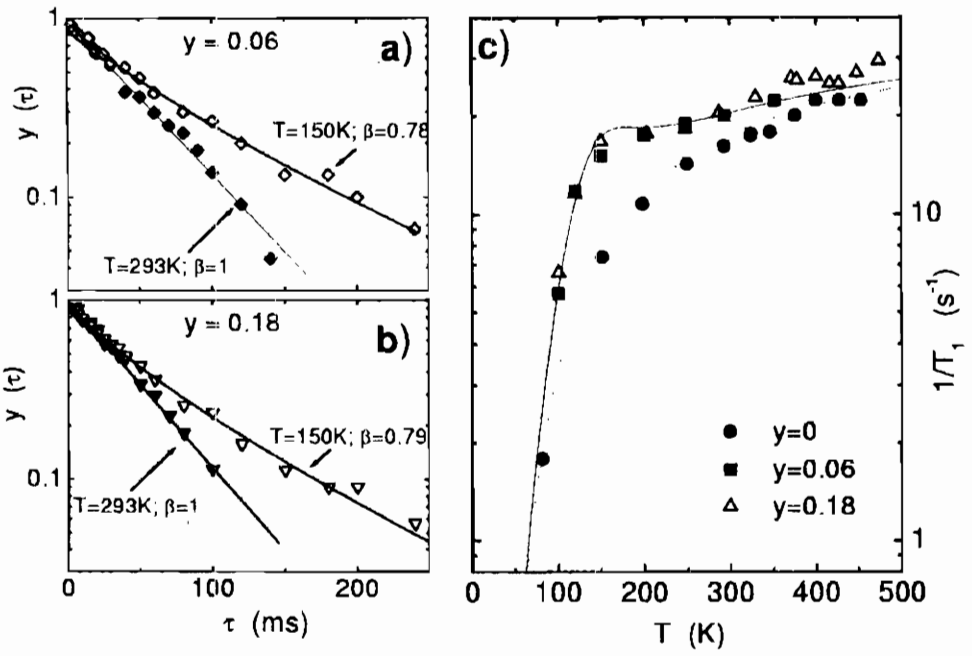

Figure 5.3: **a)** and **b)** Typical recovery plots $y(\tau) \equiv [M_z(\infty) - M_z(\tau)]/M_z(\infty)$ of the ^{89}Y nuclear magnetization along in $Y_{2-y}Ca_yBaNiO_5$. Results at selected temperatures in H_0= 5.9 T are reported. On decreasing temperature, one has a clear departure from single exponential behavior, suggestive of the progressive onset of static disorder. The spin-lattice relaxation rate $1/T_1$ has been extracted by fitting the data according to Eq. (5.1) in the text (solid lines). **c)** Spin lattice relaxation rate as a function of temperature, for different Ca-concentrations, in H_0 =5.9 T (from [Tedoldi 98]). Dotted line corresponds to the exponential function (3.9), fitting the data in pure Y_2BaNiO_5. Solid line is the best fit of the results for $y \neq 0$ according to the phenomenological model (5.2).

Besides justifying the vanishing of the NMR signal at low temperature, the observed enhancement in $1/T_2$ provides, as discussed later on, important insights on the spin dynamics at frequency $\omega \approx 0$.

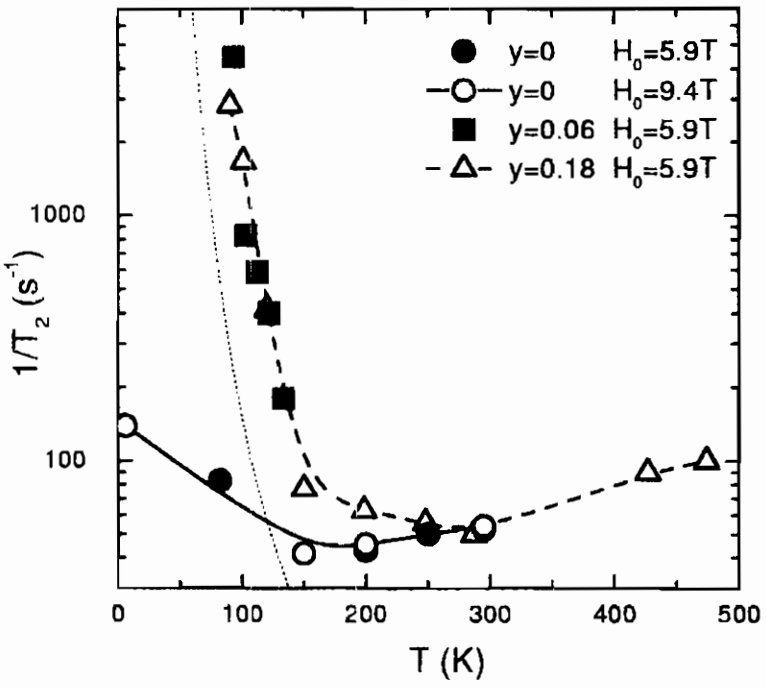

Figure 5.4: ^{89}Y spin-spin relaxation rates in $Y_{2-y}Ca_yBaNiO_5$. T_2 has been defined as the time at which the nuclear spin-echo amplitude is reduced to a factor $1/e$ of its maximal value. The dotted line represents the behavior expected for the spin-spin relaxation rate on the base of a crude extension at $\omega = 0$ of the phenomenological model accounting for $1/T_1$ (Eq. (5.2)).

5.3 Analysis and discussion

Let us start by comparing ^{89}Y spin-lattice relaxation in pure and doped Y_2BaNiO_5. As shown in Fig. 5.3 c), $1/T_1$ is increased by Ca-doping, particularly around 150 K, pointing out an enhancement of low-frequency spin fluctuations. A possible explanation for this effect is suggested by the temperature behavior of the recovery laws (Fig.s 5.3 a) and b)). The evolution of $M_z(\tau)$ towards the equilibrium is single-exponential at room temperature, indicating that ^{89}Y nuclei probes magnetic fluctuations which are the

same all over the system on the timescale of the nuclear Larmor frequency $\omega_N \approx 10^7 s^{-1}$. On cooling, the recovery of $M_z(\tau)$ turns to a multi-exponential behavior, typical of spatially-inhomogeneous relaxation. These features suggests a scenario in which the low-energy spin dynamics is sensitive to hole-hopping processes, having a characteristic frequency ω_h that decreases on decreasing temperature. In such a picture, the changeover from single- to multi-exponential behavior in the recovery laws is the sign of the slowing down, on cooling, of the hole-motion towards frequency of the order of ω_N, accompanied by the onset of site dependent spin fluctuations. Then one can try to describe phenomenologically the spin-lattice relaxation rate in $Y_{2-y}Ca_yBaNiO_5$, by adding to the function $1/T_1(T, y = 0)$ (reproducing the temperature behavior of the relaxation rate in Y_2BaNiO_5), an extracontribution accounting for the effect of hole-diffusion. Following for simplicity the treatments developed for other charge-doped AF's [Carretta93, Carretta94, Corti 97], I will tentatively describe hole-induced spin fluctuations by a q-integrated structure factor of Lorentzian form, involving an effective thermally activated hopping-time $\tau_h(T) = \tau_0 e^{E_g/T}$. Then the total spin lattice relaxation rate can be written

$$\frac{1}{T_1}(T, y) = \frac{1}{T_1}(T, y = 0) + A_h \frac{\tau_h(T)}{1 + \omega_N^2 \tau_h^2(T)}, \qquad (5.2)$$

with the term $1/T_1(T, y = 0)$ given by Eq. (3.9). As shown in Fig. 5.3, the model (5.2), with $\tau_0 = 3 \cdot 10^{-10} s$ and $E_g = 580K$, reproduces the experimental findings for $y = 0.06$ and $y = 0.18$ (solid line). At variance with the results in Li-doped NiO [Corti 97], one does not observe an increase in $1/T_1$ passing from $y = 0.06$ to $y = 0.18$. The reasons for this behavior can be searched in the abatement of single-hole mobility upon increasing doping, due to reduced dimensionality.

As anticipated, relaxation measurements in $Y_{2-y}Ca_yBaNiO_5$ below $T \approx 100K$ are made difficult by the fast decay of the echo-signal. Two mechanisms contribute in general to the echo decay. The first one is related to nucleus-nucleus dipolar interaction. This term is expected to be only slightly doping- and temperature-dependent and thus cannot explain the divergence of $1/T_2$ observed in Ca-doped samples (Fig. 5.4). A second contribution is instead related to zero frequency components of the $q-$ integrated dynam-

ical structure factor, namely

$$\frac{1}{T_2} \propto \sum_q S(q, \omega = 0) \ . \tag{5.3}$$

Thus, the dramatic enhancement in $1/T_2$ below $\approx$ 120 K is another signature of significative low-energy spectral weight in $S(q, \omega)$. The data in Fig. 5.4, on the other hand, cannot be simply justified by the extrapolation at $\omega = 0$ of the "charge-freezing" picture accounting for the temperature behavior of $1/T_1$ (see dotted line in Fig. 5.4). Thus, an additional doping-induced process seems to take place, with a characteristic frequency $\omega_\mu << \omega_N$. This could be possibly related to a cooperative slowing down of the local fluctuations involving effective magnetic moments induced by hole-localization.

The occurrence of low-temperature "localized" defects induced by Ca-doping in Y_2BaNiO_5 is clearly evidenced by magnetic susceptibility (Fig. 5.2). $\chi(T, y)$ is enhanced at low temperature, while the difference $\chi(T, x) - \chi(T, 0)$ tends to vanish for $T \to \infty$. In the framework of the model sketched above, one can describe the effects of doping on the low temperature susceptibility in terms of an effective "Curie-Weiss" extra-contribution superimposed to the AF-correlated background. Thus $\chi(T, y)$ below 150 K has been fitted by the law

$$\chi(T, y) = \chi_B(T, 0) + \frac{C(y)}{T - \Theta(y)} \ , \tag{5.4}$$

using for χ_B the chain susceptibility of pure Y_2BaNiO_5 (see Sec. 3.4). The values of C and Θ obtained in this way are reported in Tab. 5.1. In the last column of the table, the number of $S = 1/2$ spins per Ca-ion which would give a paramagnetic contribution of weight C are reported. For $y = 0.06$, one has $n \simeq 3$. This evidence can be explained by a model in which each O-type injected hole interacts antiferromagnetically with the background, forming a singlet with one hole on a neighboring Ni^{2+} and leaving an effective $S = 1/2$ spin on this latter and two on the adjacent "chain ends". Such a picture breaks down for $x = 0.18$, where one founds $n = 1.7$. This however is not surprising. In fact, due to the small distance between two defects in the sample ($\langle L \rangle \simeq 1/x \simeq 5$), one expects

y	C (emu K/mole)	θ (K)	n
0.06	$1.0 \cdot 10^{-1}$	-6.5	3.3
0.18	$1.6 \cdot 10^{-1}$	-9.1	1.7

Table 5.1: Curie constants and Curie-Weiss temperatures extracted from the best fit of the data in Fig. 5.2. n is the number of $= 1/2$ spins per Ca-impurity giving a paramagnetic term of weight C.

strong interaction between edge spins on the same chain and thus significative departure from a simple Curie-like behavior.

Appendix. Preparation and characterization of Y_2BaNiO_5-based samples

The powder samples studied in the present work have been synthesized at the *Chemistry Physics Department of the University of Pavia.*

Pure Y_2BaNiO_5 was prepared starting from a stoichiometric mixture of Y_2O_3, NiO and $BaCO_3$. After a pre-treatment up to 1373 K to decompose the carbonate, the sample was fired up to 1473 K for about 48 h and then to 1523 K for about 60 h. The structure of Y_2BaNiO_5 has been determined from X-ray powder diffraction Rietveld analysis at room temperature, after the last thermal treatment at $T = 1523$K [Massarotti 99]. The compound turns out orthorombic (spatial group *Immm*), with lattice parameters $a = 3.759$ Å, $b = 5.759$ Å and $c = 11.327$ Å, in full agreement with previous determinations [Buttrey 90].

$x = 0.05$ and $x = 0.10$ samples of $Y_2BaNi_{1-x}Mg_xO_5$ have been obtained from the reactive system $Y_2O_3/BaCO_3/NiO/MgCO_3$ (in molar ratio 1:1:(1-x):x), through the thermal treatment used for Y_2BaNiO_5. X-Ray diffraction indicates the formation of single phase compounds with the same lattice parameters of pure Y_2BaNiO_5 and provides an estimate of the real amount of Mg-doping, which turns out practically coincident with the nominal concentration x. It is worth to mention that the same magnetic perturbation induced by Mg-substitutions in Y_2BaNiO_5 (i.e. the chain-breaking) could be expected to arise also from $Zn^{2+} \rightarrow Ni^{2+}$

substitution. The presence of Zn at the Ni sites, however, tends to give rise to NiO_5 coordination instead of the usual NiO_6 octahedral coordination, so affecting the peculiar one-dimensional character of the system [Bini 99].

$Y_{2-y}Ca_yBaNiO_5$ samples were prepared starting from the mixture $Y_2O_3/CaCO_3/$ $/BaCO_3/NiO/$ in molar ratio (0.9):0.1:1:1 and (0.8):0.2:1:1. X-ray powder patterns show that Ca^{2+} ions substitute Y^{3+} in equivalent positions for effective concentrations $y = 0.06$ and $0 = 0.18$ respectively, with weak modifications in the lattice constants. Further details are given in [Massarotti 99].

Bibliography

[Affleck 87] I. Affleck, T. Kennedy, E. Lieb and H. Tasaki, Phys. Rev. Lett. **59**, 799 (1987).

[Affleck 89] I. Affleck, J. Phys. Condens. Matter **1**, 3047 (1989).

[Affleck 90a] I. Affleck, Phys. Rev. B **41**, 6697 (1990)[5].

[Affleck 90b] I. Affleck, *Fields, Strings and Critical Phenomena*, edited by E. Brezin and J. Zinn-Justin (North-Holland, 1990).

[Anderson 52] P. W. Anderson, Phys. Rev. **86**, 694 (1952).

[Anderson 59] P. W. Anderson, Phys. Rev. **115**, 2 (1959).

[Anderson 63] P. W. Anderson, Solid State Phys. **14**, 99 (1963).

[Auerbach] A. Auerbach, *Interacting Electrons and Quantum Magnetism* (Springer-Verlag, 1994).

[Azuma 94] M. Azuma, Z. Hiroi and M. Takano Phys. Rev. Lett. **73**, 3463 (1994).

[Azuma 97] M. Azuma *et al.*, Phys. Rev. B **55**, R8658 (1997).

[Batista 98a] C. D. Batista, K. Halberg, and A. A. Aligia, Phys. Rev. B **58**, 9248 (1998).

[Batista 98b] C. D. Batista, A. A. Aligia and J. Ercoles, Europhys. Lett. **43**, 71 (1998).

[Bethe 31] H. A. Bethe Z. Phys. **71**, 205 (1931).

[Bednorz 86] J.G. Bednorz and K.A. Muller, Z. Phys. B **64**, 189 (1986).

[Beeman 68] D. Beeman and P. Pincus, Phys. Rev. **166**, 359 (1968).

[5]Eq.(2.14) in Ref.[Affleck 90a] has an error (see private comun. by I. Affleck reported in [Takigawa 95]).

[Bini 99] M. Bini, D. Capsoni and V. Massarotti, *private comunication.*

[Bloembergen 48] N. Bloembergen, E. M. Purcell and R. V. Pound, Phys. Rev. **73**, 679 (1948).

[Bobroff 97] J. Bobroff *et al.*, Phys. Rev. Lett. **79**, 2117 (1997) and **80**, 3663 (1998).

[Botti 99] S. Botti, A. Rosso and F. Tedoldi, unpublished.

[Buttrey 90] D. J. Buttrey, J. D. Sullivan and A. L. Rheingold, J. Solid State Chem. **88**, 291 (1990).

[Buyers 86] W. J. L. Buyers *et al.*, Phys. Rev. Lett. **56**, 371 (1986).

[Chaboussant 97] G. Chaboussant *et al.*, Phys. Rev. Lett. **79**, 925 (1997).

[Chaboussant 98] G. Chaboussant *et al.*, Eur. Phys. J. B **6**, 167 (1998).

[Carretta98] P. Carretta *et al.*Phys. Rev. B **57**, R5606 (1998), and **56**, 14587 (1997).

[Carretta93] P. Carretta, M. corti and A. Rigamonti, Phys. Rev. B **48**, 3433 (1993).

[Carretta94] P. Carretta, F. Cintolesi and A. Rigamonti, Phys. Rev. B **49**. 7044 (1994).

[Corti 97] M. Corti, S. Marini, A. Rigamonti, F. Tedoldi, D. Capsoni and V. Massarotti, Phys. Rev. B **56**, 11056 (1997).

[Dagotto 92] E. Dagotto, J. Riera et D.J. Scalapino, Phys. Rev. B **45**, 5744 (1992).

[Dagotto 96] E. Dagotto, J. Riera, A. Sandvik and A. Moreo, Phys. Rev. Lett. **76**, 1731 (1996); see also C. D. Batista, A. A. Aligia and J. Ercoles Phys. Rev. Lett. **81**, 4027 (1998), and E. Dagotto and J. Riera, Phys. Rev. Lett. **81**, 4028 (1998).

[Darriet 93] J. Darriet and L. P. Regnault, Solid State Comm. **86**, 409 (1993).

[DiTusa 94] J. F. DiTusa *et al.*, Phys. Rev. Lett. **73**, 1857 (1994).

[Emery 97] V.J. Emery, S.A. Kivelson et O. Zachar, Phys. Rev. B **56**, 6120 (1997).

[Fabrizio 93] M. Fabrizio Phys. Rev. B **54**, 10054 (1996).

[Fabrizio 97] M. Fabrizio and R. Mélin, Phys. Rev. B **56**, 5996 (1997).

[Fabrizio 99] M. Fabrizio, R. Mélin and J. Souletie, Eur. Phys. J. B **10**, 607 (1999).

[Feng 92] Z. Feng and M. S. Seehra, Phys. Rev. B **45**, 2184 (1992).

[Fradkin] E. Fradkin, *Field Theories of Condensed Matter* (Addison-Weasley, 1991).

[Fujiwara 93] N. Fujiwara, T. Goto, S. Maegawa, and T. Kohmoto, Phys. Rev.B **47**, 11860 (1993).

[Fujiwara 98] N. Fujiwara *et al.*, Phys. Rev. Lett. **80**, 604 (1998).

[Fukuyama 96] H. Fukuyama, N. Nagaosa, M. Saito and T. Tanimoto, J. Phys. Soc. Jpn. **65**, 2377 (1996).

[Gaveau 90] P. Gaveau, J. P. Boucher, L. P. Regnault, and J. P. Renard, Europhys. Lett. **12**, 647(1990).

[Golinelli 92] O. Golinelli, T. Jolicœur and R. Lacaze, Phys. Rev. B **45**, 9798 (1992).

[Gómez 89] G. Gómez-Santos, Phys. Rev. Lett. **63**, 790 (1989).

[Goto 97] T. Goto, S. Satoh, Y. Matsumura and M. Hagiwara, Phys. Rev. B **55**, 2709 (1997).

[Granroth 98] G. E. Granroth *et al.*, Phys. Rev. B **58**, 9312 (1998).

[Hagiwara 90] M. Hagiwara *et al.*, Phys. Rev. Lett. **65**, 3181 (1990).

[Haldane 83] F. D. M. Haldane, Phys. Lett. **93A**, 464 (1983) and Phys. Rev. Lett. **50**, 1153 (1983).

[Hoenberg] P. C. Hoenberg, Phys. Rev. **158**, 383 (1967).

[Holstein 40] T. Holstein and H. Primakoff, Phys. Rev. **58**, 1908 (1940).

[Hubbard 64] J. Hubbard, Proc. Roy. Soc. London A **277**, 237 (1964) and **281**, 401 (1964).

[Imai 98] T. Imai *et al.*Phys. Rev. Lett. **81**, 220 (1998).

[Ivanov 99] D. A. Ivanov and P. A. Lee Phys. Rev. B **59**, 4803 (1999).

[Jolicœur 94] T. Jolicœur and O. Golinelli, Phys. Rev. B **50**, 9265 (1994).

[Julien 99] M. H. Julien *et al.*, preprint.

[Kennedy 90] T. Kennedy, J. Phys. Condens. Matter **2**, 5737 (1990).

[Kennedy 92] T. Kennedy and H. Tasaki, Commun. Math. Phys. **147**, 431 (1992).

[Kim 98] Y. J. Kim, M. Greven, U. J. Wiese, and R. J. Birgeneau, Eur. Phys. J. B **4**, 291 (1998).

[Kimura 98] S. Kimura *et al.*, J. Phys. Soc. Jpn. **67**, 2514 (1998).

[Kittel] C. Kittel, *Quantum Theory of Solids* (John Wiley & Sons, 1967).

[Kojima 95] K. Kojima *et al.*, Phys. Rev. Lett. **74**, 3471 (1995).

[Kosevich 86] Y. A. Kosevich and A. V. Chubukov, Sov. Phys. JEPT **64**, 654 (1986).

[Kubo 52] R. Kubo, Phys. Rev. **87**, 568 (1952).

[Laukamp 98] M. Laukamp *et al.*, Phys. Rev. B **57**, 10755 (1998).

[Lieb 61] E. Lieb, T. D. Schultz and D. C. Mattis, Ann. Phys. **16**, 407 (1961).

[Lieb 62] E. Lieb and D. C. Mattis, J. Math. Phys. **3**, 749 (1932).

[Massarotti 99] V. Massarotti, D. Capsoni, M. Bini, A. Altomare and A. G. G. Moliterni, Z. Kristallogr. **214**, 205 (1999).

[Mattis] D. C. Mattis, *The Theory of Magnetism I* (Springer-Verlag, 1988).

[Melzi 99] R. Melzi and P. Carretta, cond-mat/9904074.

[Mermin 66] N. D. Mermin and H. Wagner, Phys. Rev. Lett. **17**, 1133 (1966).

[Michel 82] C. Michel and B. Raveau, J. Solid State Chem. **43**, 73 (1982).

[Michel 84] C. Michel, L. Er-Rakho and B. Raveau, Rev. Chim. Min. **21**, 85 (1984).

[Miyashita93] S. Miyashita and S. Yamamoto, Phys. Rev. B **48**, 913 (1993).

[Moriya 56] T. Moriya, Prog. Theor. Phys. **16**, 23 (1956).

[Moriya 63] T. Moriya, J. Phys. Soc. Jap. **18**, 516 (1963).

[Mott] N. F. Mott, *Metal - Insulator Transitions*, (Taylor & Francis, 1990).

[Mott 49] N. F. Mott, Proc. Roy. Soc. London A **62**, 416 (1949).

[Muller 88] Hk. Muller-Buschbaum and C. Lang, J. Less Common. Met., **142**, L1 (1988).

[Muller 89] Hk. Muller-Buschbaum and I. Ruter, Z. Anorg. Allg. Chem., **572**, 181 (1989).

[Naef 99] F. Naef and X. Wang, cond-mat/9907117.

[Polizzi 98] E. Polizzi, F. Mila, and E. S. Sorensen, Phys. Rev. B **58**, 2407 (1998).

[Ramirez 94] A. P. Ramirez, S. W. Cheong, and M. L. Kaplan, Phys. Rev. Lett. **72**, 3108 (1994).

[Regnault 94] L. P. Regnault, I. Zaliznyak, J. P. Renard and C. Vettier, Phys. Rev. B **50**, 9174 (1994).

[Regnault 95] L. P. Regnault and J. P. Renard, Physica B **215**, 71 (1995).

[Renard 87] J. P. Renard *et al.*, Europhys. Lett., **3**, 945 (1987).

[Renard 88] J. P. Renard *et al.*, J. Appl. Phys., **63**, 3538 (1988).

[Reyes 97] A. P. Reyes *et al.*, Phys. Rev. B **55**, 8079 (1997).

[Rigamonti 98] A. Rigamonti, F. Borsa and P. Carretta, Rep. Prog. Phys. **61**, 1367 (1998).

[Sagi 96] J. Sagi et I. Affleck, Phys. Rev. B **53**, 9188 (1996).

[Sakaguchi 96] T. Sakaguchi, K. Kakurai, T. Yokoo, and J. Akimitsu, J. Phys. Soc. Jpn. **65**, 3025 (1996).

[Sakai 90] T. Sakai and M. Takahashi, Phys. Rev. B **42**, 1090 (1990) and Phys. Rev. B **42**, 4537 (1990).

[Sandvik 96] A. W. Sandvik. E. Dagotto and D. J. Scalapino, Phys. Rev. B **53**, R2934 (1996).

[Santachiara 99] R. Santachiara, Thesis, University of Pavia (1999).

[Sawatzky 90] G.A. Sawatzky, in *Early and Recent Aspects of Superconductivity*, edited by J.G. Bednorz and K.A. Muller (Springer-Verlag, 1990), p.345.

[Shender 91] E. F. Shenderand S. A. Kivelson, Phys. Rev. Lett. **66**, 2384 (1991).

[Schiffler 86a] S. Schiffler and Hk. Muller-Buschbaum, Z. Anorg. Allg. Chem., **532**, 10 (1986).

[Schiffler 86b] S. Schiffler and Hk. Muller-Buschbaum, Z. Anorg. Allg. Chem., **540/541**, 243 (1986).

[Schiffler 87] S. Schiffler and Hk. Muller-Buschbaum, Monatsh. Chem., **118**, 741 (1987).

[Shimizu 95] T. Shimizu *et al.*, Phys. Rev. B **52**, R9835 (1995).

[Slichter] C.P. Slichter, *Principles of Magnetic Resonance* (Springer-Verlag, 1990).

[Sorensen 94] E. S. Sorensen and I. Affleck, Phys. Rev. B **49**, 15771 (1994).

[Takahashi 88] M. Takahashi, Phys. Rev. B **38**, 5188 (1988).

[Takahashi 89] M. Takahashi, Phys. Rev. Lett. **62**, 2313 (1989).

[Takigawa 95] M. Takigawa, T. Asano, Y. Ajiro, and M. Mekata, Phys. Rev. B **52**, R13807 (1995).

[Takigawa 96] M. Takigawa, T. Asano, Y. Ajiro, and M. Mekata, Y. J. Uemura, Phys. Rev. Lett. **76**, 2173 (1996).

[Takigawa 97] M. Takigawa, M.Motoyama. H.Eisaki and S. Uchida, Phys. Rev. B **55**, 14129 (1997).

[Tedoldi 98] F. Tedoldi *et al.*, J. Appl. Phys. **11**, 6605 (1998).

[Tedoldi 99a] F. Tedoldi, A. Campana and P. Carretta, Eur. Phys. J. B **7**, 219 (1999).

[Tedoldi 99b] F. Tedoldi and A. Rigamonti, Physica B **259-261**, 995 (1999).

[Tedoldi 99c] F. Tedoldi, R. Santachiara and M. Horvatić, Phys. Rev. Lett. **83**, 412 (1999).

[Troyer 94] M. Troyer, H. Tsunetsugu et D. Wurtz, Phys. Rev. B **50**, 13515 (1994).

[Uchiyama 99] Y. Uchiyama *et al.*, Phys. Rev. Lett. **83**, 632 (1999).

[van Elp 92] J. van Elp *et al.*, Phys. Rev. B **45**, 1612 (1992).

[White 92] S. R. White, Phys. Rev. Lett. **69**, 2863 (1992).

[White 93] S. R. White and D. A. Huse, Phys. Rev. B **48**, 3844 (1993).

[Xu 96] G. Xu *et al.*, Phys. Rev. B **54**, R6827 (1996).

[Yokoo 95] T. Yokoo *et al.*, J. Phys. Soc. Jpn. **64**, 3651 (1995).

[Zaanen 85] J. Zaanen, G. A. Sawatzky and J. W. Allen, Phys. Rev. Lett. **55**, 418 (1985).

[Zaanen 87] J. Zaanen and G. A. Sawatzky Can. J. Phys. **65**, 1262 (1987).

[Zhang 88] F. Zhang and T. M. Rice, Phys. Rev. B **37**, 3759 (1988).

[Zinn-Justin] J. Zinn-Justin, *Quantum Field Theory and Critical Phenomena* (Oxford Science, 1989).

Acknowledgements

Many colleagues and friends have contributed in several ways to this work. Thanks are due to: Attilio Rigamonti, Sergio Aldrovandi, Maurizio Corti, Pietro Carretta, Alessandro Lascialfari, Ferdinando Borsa, Roberto Sala, Andrea Campana, Roberto Melzi, Alberto Rosso, Silvana Botti, Raoul Santachiara, Carlo Brugna, Marc H. Julien, Stefania Marini, Cristina Mozzati, Vittorio Massarotti, Doretta Capsoni, Marcella Bini, Carlo B. Azzoni, Daniela Di Martino, Michele Fabrizio, Claude Berthier, Mladen Horvatić, Jean Paul Boucher, Frederic Mila, Erik Sorensen and Paola Verrucchi.

A facility for the study of particle-induced infrared emission in noble gases

Davide Iannuzzi
Dipartimento di Fisica Nucleare e Teorica
Università di Pavia

1st March 2001

1 Introduction

The aim of our research is to investigate the properties of a new kind of particle detectors based on particle induced infrared emission rather than visible or ultraviolet scintillation[1]-[11]. The first step in this direction is to identify materials that efficiently convert the energy of an ionizing particle into infrared photons (light yield[†] larger than 20000 photons/MeV).

Among the samples investigated so far, gaseous Xenon at room temperature and nearly atmospheric pressure is an interesting candidate. In the wavelength region between 0.8 and 1.7 μm, its light yield is 21000±3000 photons/MeV[4]. The emission was initially ascribed to radiative decays of highly excited Xenon atoms[4] because in the visible to near infrared region (up to 0.9 μm) the spectrum is dominated by atomic transitions [12]-[14], and a similar behaviour is expected at higher wavelength (see [15] and references therein). Furthermore, our preliminary measurements of proton-induced infrared spectra in gaseous Argon are not in contraddiction with this hypothesis[6], although the signal-to-noise ratio of the spectra is too small for a clear identification of the atomic transitions involved.

However, atomic transitions are not expected to be so intense[15]. The infrared light yield in gaseous Xenon is of the same order of magnitude of the well known vacuum-ultraviolet scintillation light yield ($\simeq$20000 photons/MeV[16]). This emission (called *second continuum*) is ascribed to the radiative transitions from the bound excimer states $^{1,3}\Sigma_u^+$ to the dissociative excimer state $^1\Sigma_g^+$[17] and dominates over atomic decays. Since during the passage of an ionizing particle higher excimer levels are populated as well[17, 18], it is reasonable to rise the question if the infrared emission might be the result of a radiative transition among these higher excimer states.

In order to clarify the phenomenology observed, we realized an experimental facility for systematic measurements of the emission

[†]The light yield is defined as the number of photons emitted per unit of energy released by the particle.

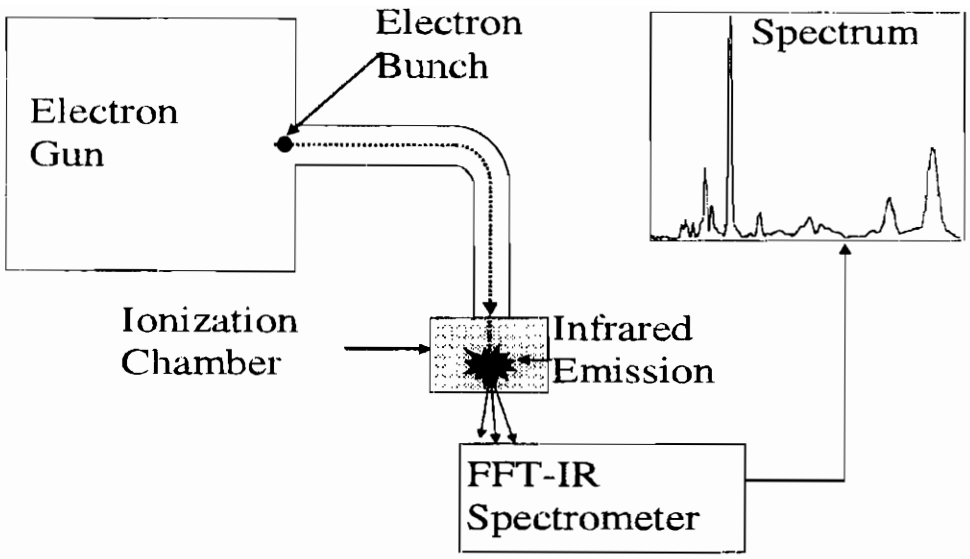

Figure 1: A scheme of the experimental apparatus.

spectra induced by ionizing particles in noble gases. In this paper we describe the technical details of this instrumentation.

2 Experimental details

A simplified lay-out of the experimental apparatus is shown in figure 1. A pulsed electron beam, produced by an homemade electron gun, enters an ionization chamber filled with the gaseous sample. A Fast-Fourier-Transform Michelson spectrometer (FFT-IR) analyzes the infrared light at the exit of the chamber. The experimental apparatus can be divided into three main devices: (i) the electron gun, (ii) the ionization chamber, and (iii) the FFT-IR spectrometer (see also figures 2 and 3).

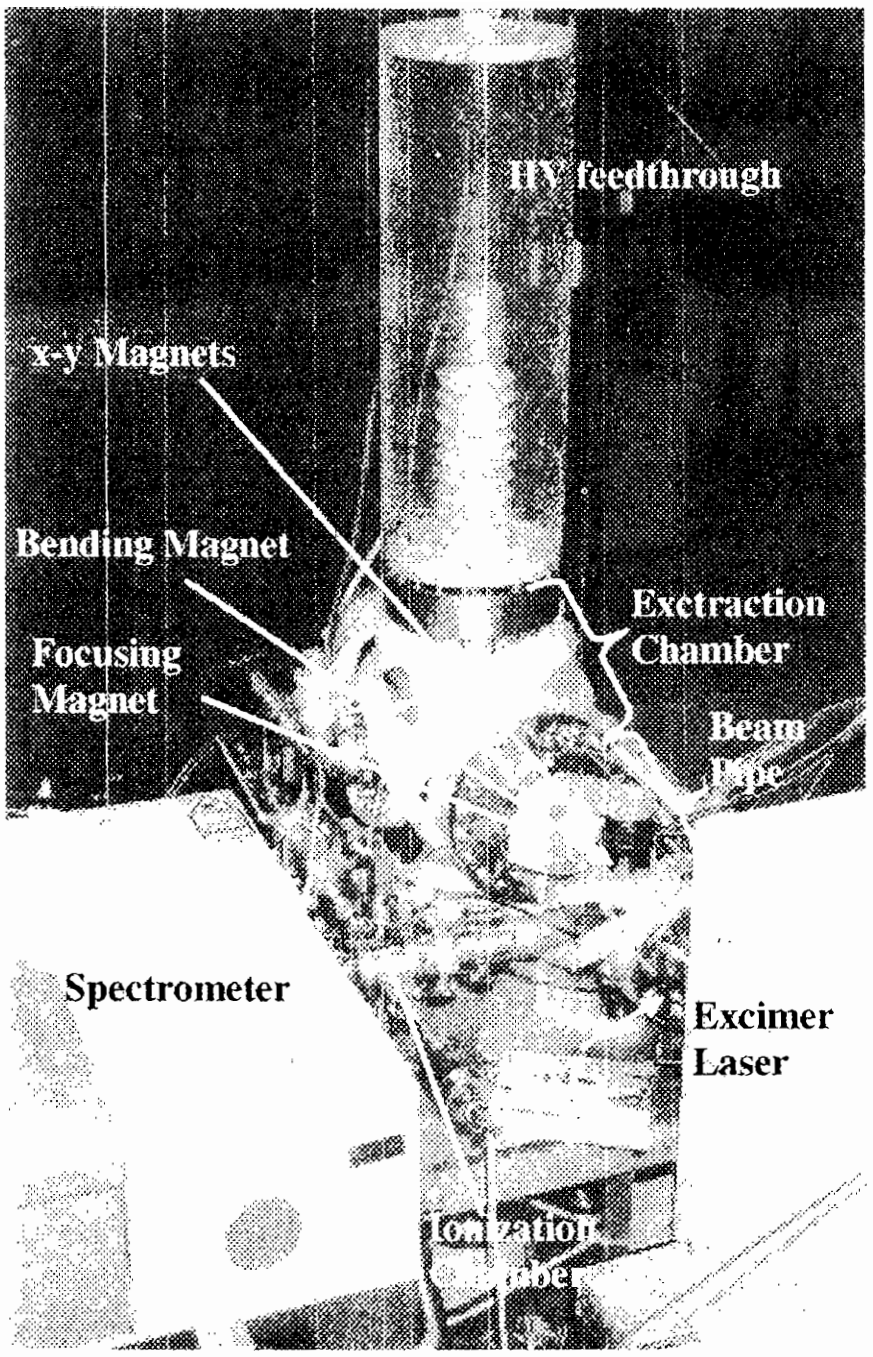

Figure 2: A picture of the experimental apparatus.

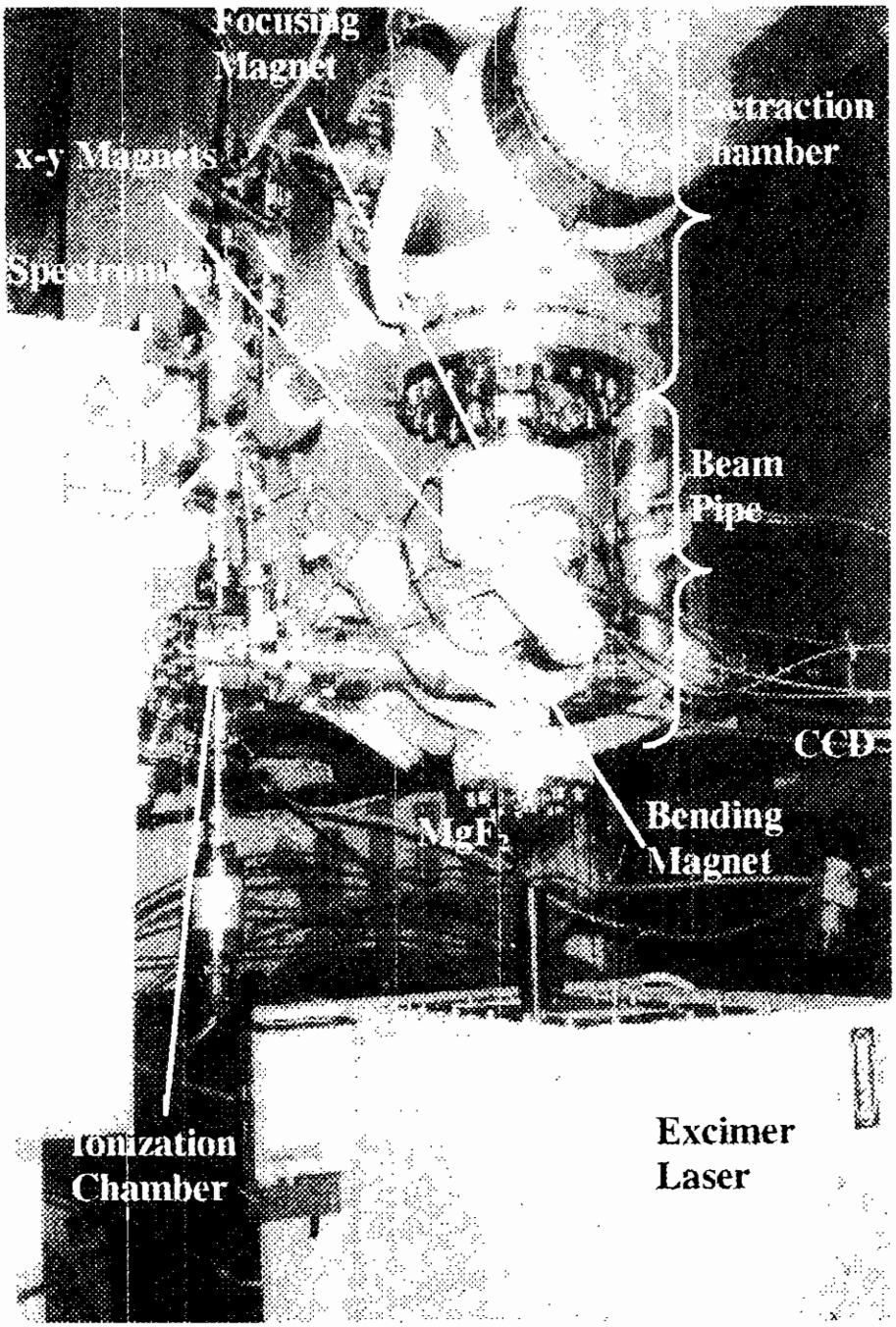

Figure 3: A picture of the experimental apparatus (top view).

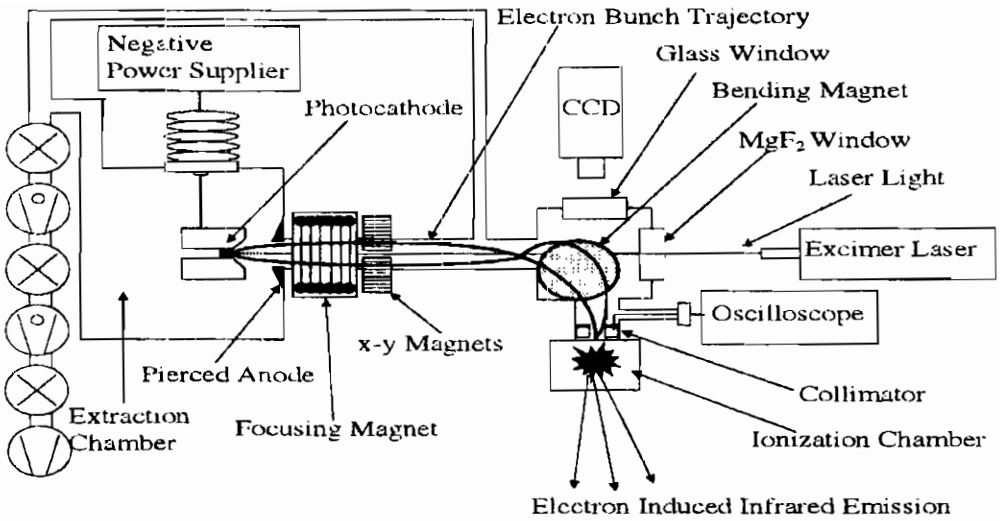

Figure 4: A schematic view of the electron gun.

2.1 The electron gun

The homemade pulsed electron gun is represented in figure 4. Electron bunches are produced in a high vacuum stainless steel chamber (hereafter called *extraction chamber*) by means of photoelectric extraction from a metallic cathode. The cathode is kept at negative voltage with respect to a centrally pierced metallic anode, set in front of it and kept to ground. The photoelectrons are therefore accelerated by the electric field towards the anode, exit the extraction chamber passing through the anode hall, and enter an high vacuum stainless steel beam pipe. In the beam pipe, the bunches are magnetically focused and bent towards the entrance of the gas chamber.

The extraction chamber and the beam pipe are kept at a vacuum level of the order of 10^{-6} mbar or less by means of two consecutive turbo-molecular pumps coupled with a rotatory pump. This avoids high voltage discharges in the extraction chamber and beam losses in the beam pipe.

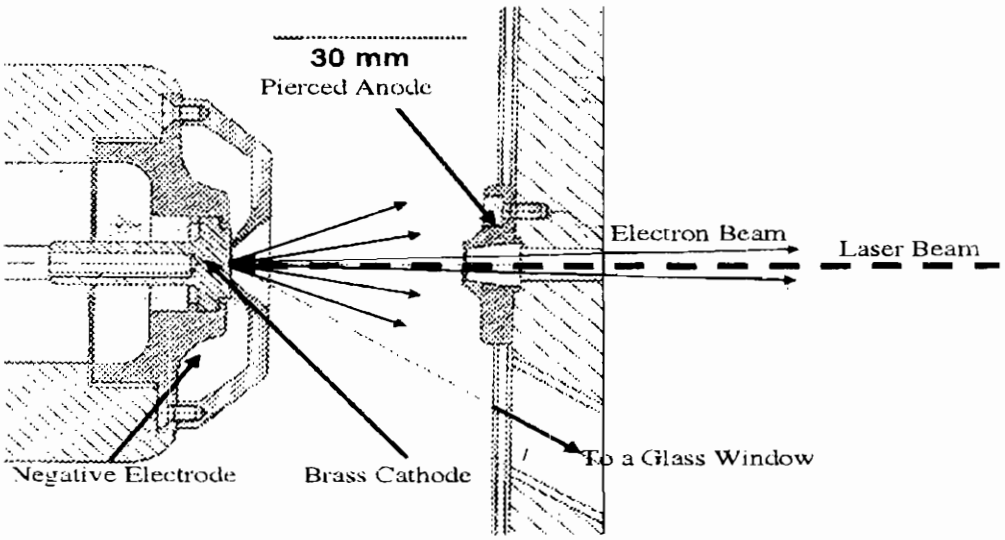

Figure 5: A drawing of the electrodes of the electron gun.

Photoelectric extraction is realized with a Ne-Ar-F excimer laser (Lambda Physik) that emits 192 nm wavelength photons in 50 ns long bunches at a maximum rate of 100 Hz, with an emission power of 10 mJ. The photons enter the beam pipe through a MgF_2 window, pass through the anode hall, and hit frontally the photocathode (see figure 4).

The photocathode is a brass plate, polished with a 0.25 μm diamond paste and fixed onto a stainless steel electrode. The pierced anode is also of stainless steel. The shapes and the dimensions of the electrodes, reported in figure 5, are designed for maximizing the charge output of the electron gun. The cathode is connected to a power supply (RHR120W Spellman) that provides a negative voltage up to -100 kV, while the anode is kept to ground.

Near the anode, at the beginning of the beam pipe, a coil magnetic lens focuses the electrons. Other two couples of smaller coil magnets correct the trajectory of the electrons in the plane orthogonal to the beam pipe direction. Finally, a coil bending magnet

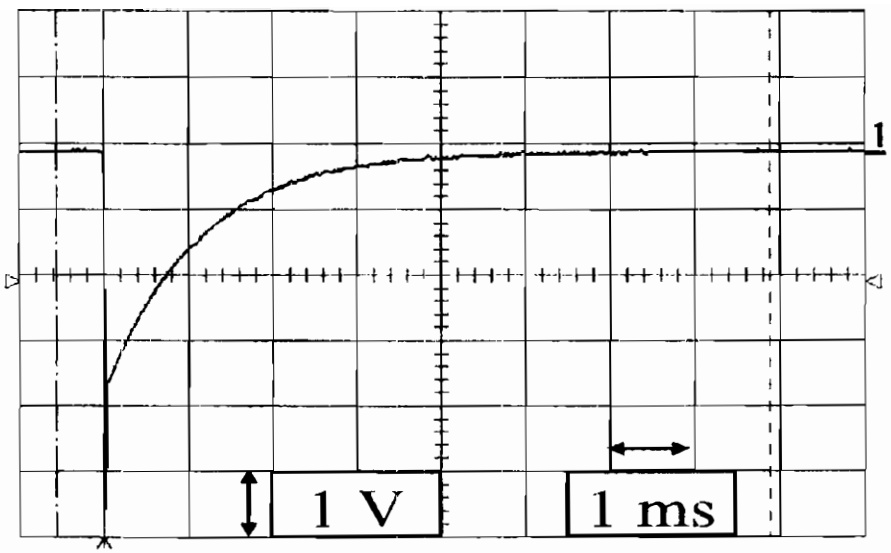

Figure 6: Typical signal for the measurement of the number of electrons per bunch.

accomplishes a 90° rotation of the beam direction, towards the gas chamber entrance. All the magnet currents can be adjusted in order to optimize the direction and spot-size of the electron bunches.

Before entering the chamber, the electrons pass a collimator made by a centrally pierced metallic plate. The hall is aligned with the entrance window of the gas chamber, and its diameter is equal to the entrance window diameter. The plate is connected to an high impedance (1 MΩ) channel of a digital oscilloscope. This collimator is used to periodically measure the mean number of electrons per bunch. Adjusting the current on the coils of the two deflection magnets or of the bending magnet, we make the bunches collide against the metal. A typical signal corresponding to a collision of an electron bunch is shown in figure 6.

Integrating this signal by means of the oscilloscope computational options, we obtain a direct measure of the charge per bunch at the end of the beam pipe. Values up to 10 nC/bunch can be

Electron energy	Pulse duration	Pulse frequency	Charge per bunch	Spot size
up to 100 keV	50 ns	1 to 100 Hz	up to 10 nC	3 mm

Table 1: Electron gun properties

reached.

The collimator can be also used as a monitor for the beam direction and divergence. Its metallic surface faced to the beam pipe is covered with a thin film of fluorescent material. In front of it, in the position reported in figure 4, a CCD-camera detects the fluorescence light induced by the electrons that collide against the collimator. The minimum spot size that can be obtained is about 3 mm.

In table 1 a summary of the electron gun properties is reported.

2.2 The ionization chamber

A schematic view of the ionization chamber is reported in figure 7 (see also figure 8). It consists of a stainless steel cylindrical chamber, mounted with the basis orthogonal to the beam direction.

The electrons enter the chamber passing a 3 mm diameter Kapton window on the center of one of the two basis of the cylinder. The thickness of the Kapton foil is 13 μm. Using the National Institute of Standards and Technology data for the energy-loss of electrons in Kapton[19], it can be estimated that a 100 keV beam looses approximately 7.1 keV passing of the entrance window. For lower energies, we refer the reader to figure 9. At room temperature, the pressure inside the chamber can be set up to nearly 20 bar before breaking the Kapton foil. Thus, measurements of gaseous samples at pressure up to 20 bar can be performed.

The infrared light exits the chamber passing through a quartz window opposite to the entrance window. The transparency of the

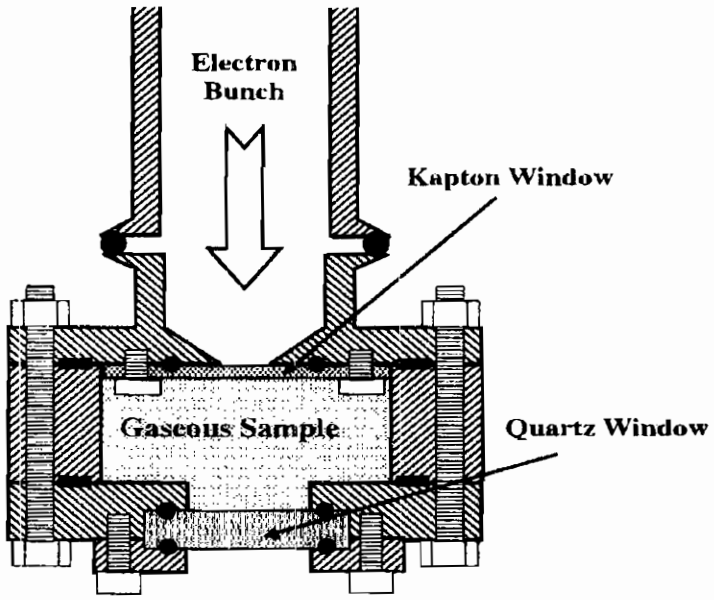

Figure 7: A schematic drawing of the ionization chamber.

quartz window in the infrared range is given in figure 10. The thickness of the window is 1 cm. The aperture diameter is also 1 cm, while its distance from the entrance window is 5 cm. In table 2, the range of 100 keV electrons in Ne, Ar, Kr and Xe at room temperature is given as a function of the gas pressure. It can be seen that, except for Ne, and for pressure higher than $\simeq$ 2 bar, almost all the electrons are stopped before hitting the quartz window.

The chamber is connected to a bottle containing the gas with a nominal purity of about 10 ppm, to a vacuum pump and to a recirculation system equipped with an 0.1 l purifier cartridge (Oxisorb, Messer) (see figure 11 and 12). The chamber is evacuated down to 10^{-5} mbar before each gas filling by means of a turbomolecular pump coupled with a rotatory pump. After the filling, a recirculation pump forces the gas to flow continously through the purifier cartridge during all the measurement time with a flow rate of the order of 1 l/min. This technique allows to keep the gas purity

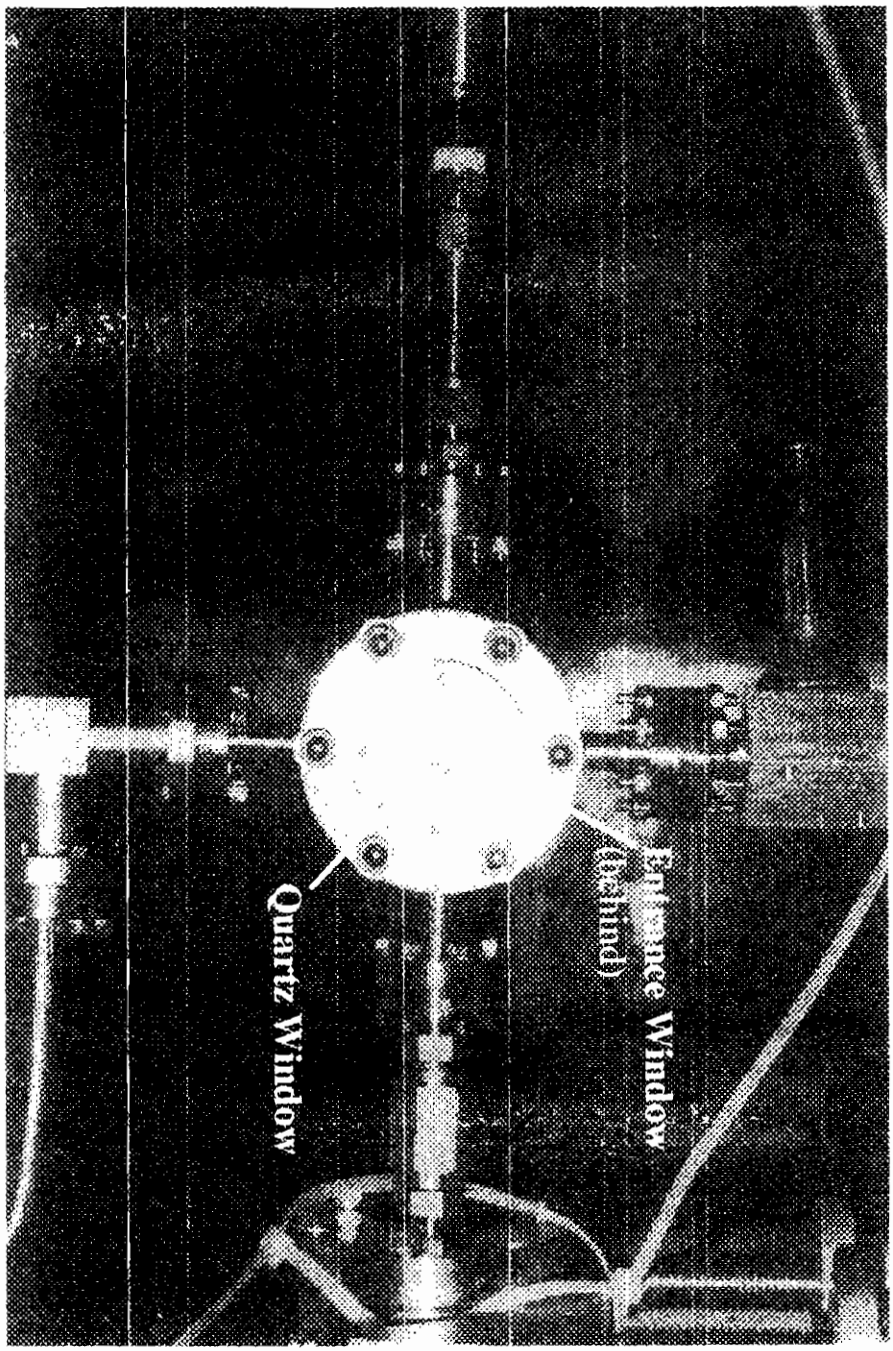

Figure 8: A frontal picture of the ionization chamber.

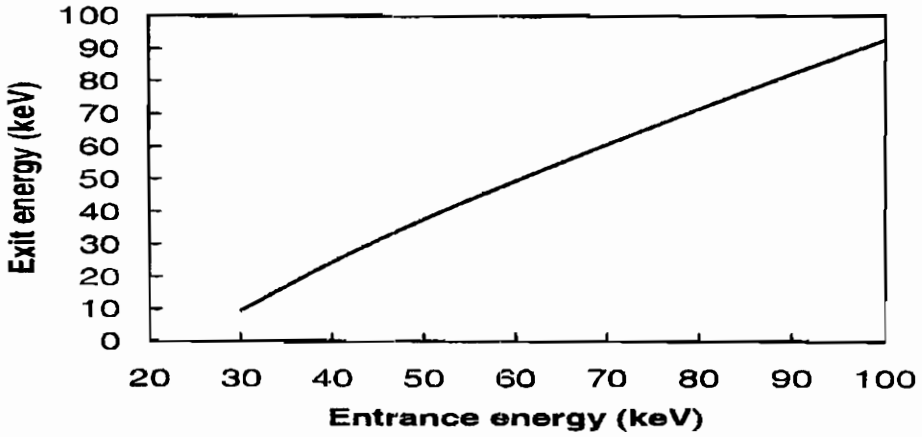

Figure 9: Energy of the electrons after the passage of the entrance window.

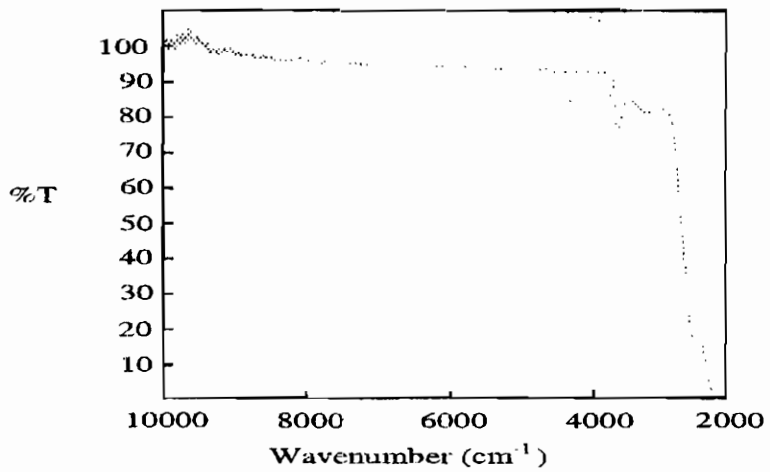

Figure 10: Transparency of the quartz window. In the opinion of the authors of the measurements, values higher than 100% are due to systematic errors and must be considered as 100% value.

	1 bar	2 bar	3 bar	4 bar	5 bar	10 bar	20 bar
Ne	21.0	10.5	7.0	5.2	4.2	2.1	1.0
Ar	12.3	6.1	4.1	3.1	2.5	1.2	0.6
Kr	6.9	3.4	2.3	1.7	1.4	0.7	0.3
Xe	4.9	2.4	1.6	1.2	1.0	0.5	0.2

Table 2: Range of 100keV electrons in rare gases (in cm)

higher than 1 ppm, so that spectra features induced by impurities can be neglected.

2.3 The FFT-IR spectrometer

The infrared spectrum is performed by means of a FFT-IR spectrometer (Bruker Equinox55) whose entrance faces the light exit window of the ionization chamber. A schematic view of its most important optical hardware is shown in figure 13. The infrared light produced inside the ionization chamber is focused onto the KBr beam splitter of a Michelson interferometer. The beam splitter allows half light to pass through while it reflects the other half. The two splitted beams are reflected back to the beam splitter by two different mirrors. One of the two mirror is located at a fixed distance L from the beam splitter. The distance of the other mirror (hereafter called *moving mirror*) from the beam splitter is $L + x$, where x is an adjustable distance. Thus the two parts of the splitted beam pass again through the beam splitter after a total path length of $2L$ and $2(L+x)$. When the two halves of the beam recombine on the beam splitter, they have an optical delay of $2x$. The recombined beam is finally focused on an infrared detector that measures the intensity I of the light as a function of the moving mirror displacement x. The function $I(x)$ is usually called interferogram. For example, in an ideally monochromatic emission at wavelength λ, the interferogram is:

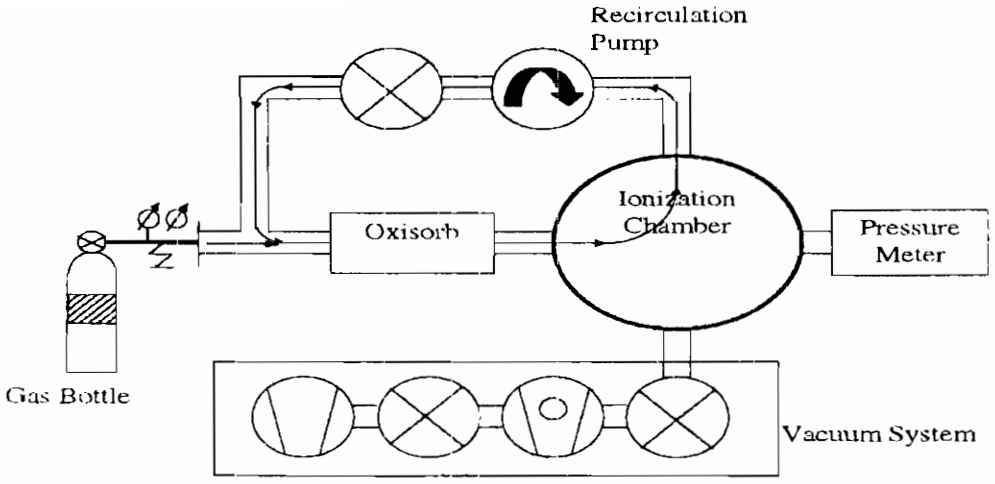

Figure 11: Scheme of the recirculation system.

$$I(x) = S(\nu)\cos(2\pi\nu x) \tag{1}$$

where $S(\nu)$ is the intensity of the monochromatic line located at the wavenumber $\nu = \lambda^{-1}$. In a more general case, when the emitted light is not monochromatic, the interferogram is given by

$$I(x) = \Re\left\{\int S(\nu)e^{-2\pi i\nu x}d\nu\right\} \tag{2}$$

To obtain the spectrum, it is necessary to measure I in correspondance of several values of x and calculate the real part of its Fourier Transform:

$$S(\nu) \propto \Re\left\{\int I(x)e^{2\pi i\nu x}dx\right\} \tag{3}$$

It is important to have a precise measurement of x before measuring $I(x)$. For this reason, the moving mirror is mounted on a step-motor controlled by an electronic board (TC-20, Bruker Optics) (hereafter called *mirror-board*). The monochromatic light of

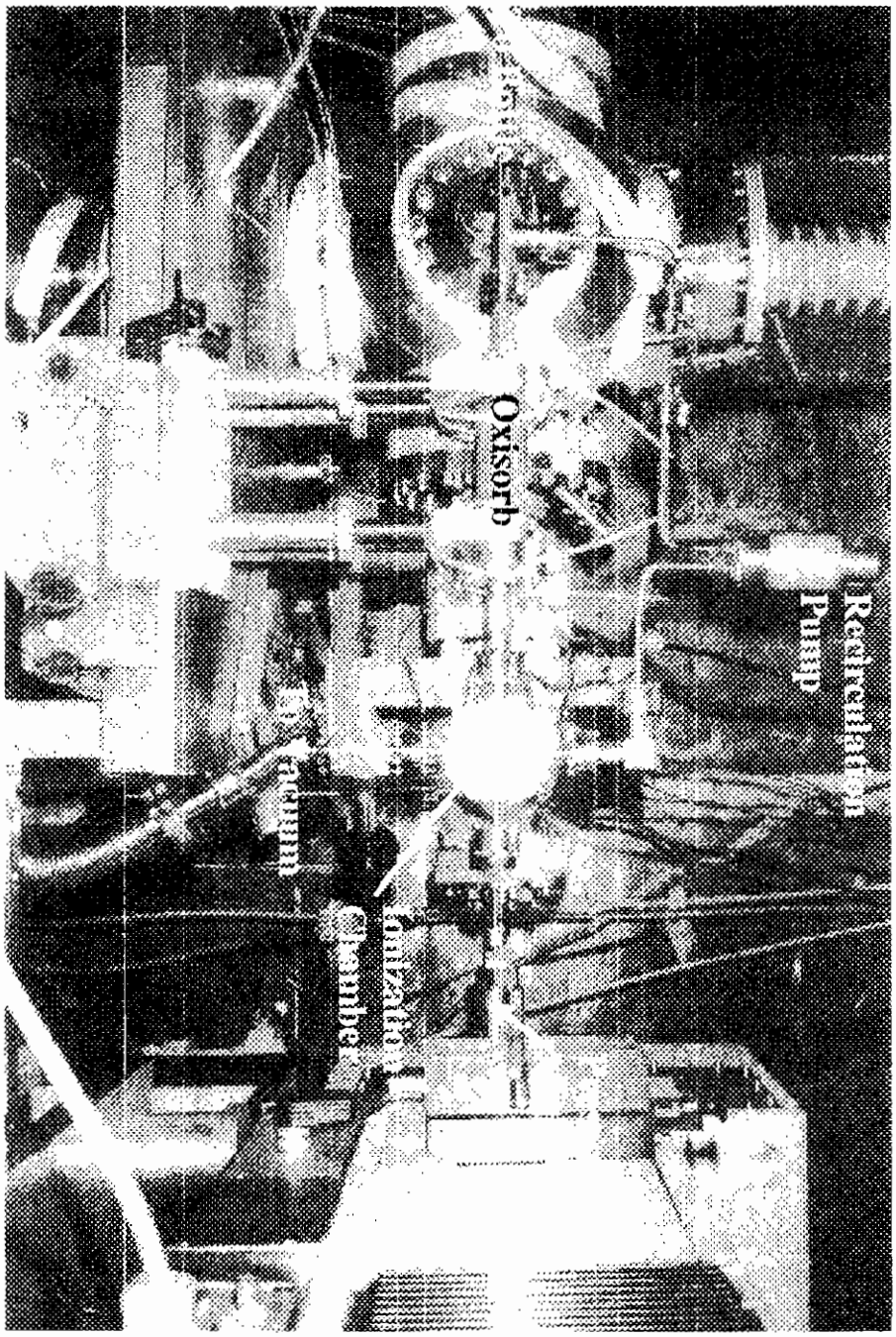

Figure 12: A picture of the recirculation system.

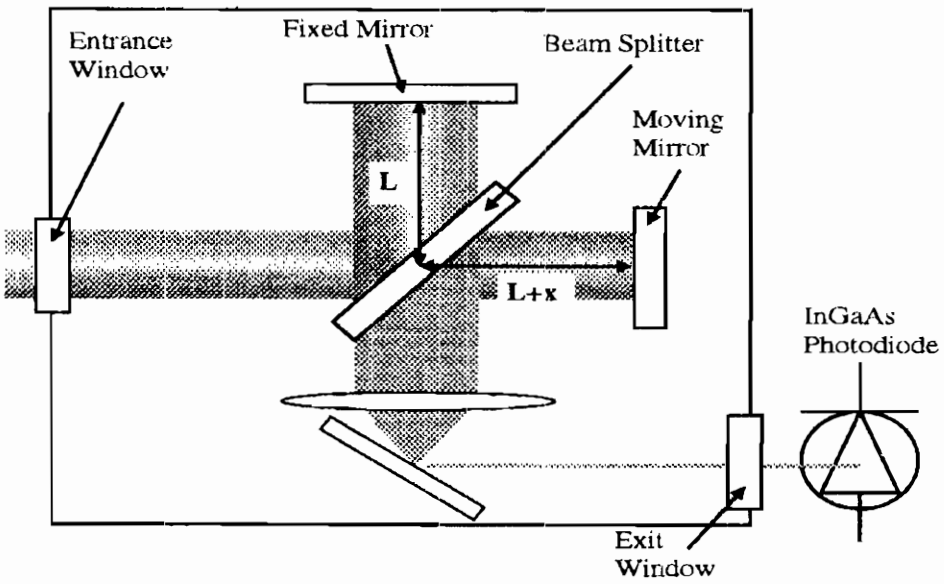

Figure 13: A schematic view of the spectrometer's optics.

a He-Ne laser enters continuosly into the interferometer. The interference of the He-Ne laser light at the exit of the interferometer is read by a photodiode sensitive in the visible region. The output of the photodiode is sent to the mirror-board that stops the mirror only in the positions for which a maximum or a minimum of interference is measured, i.e. for $2x = \frac{\lambda^*}{2}$, where $\lambda^* = 633$ nm is the emission wavelength of the He-Ne laser. The positions x at which the intensity I can be measured are

$$\ldots, L - n \cdot \frac{\lambda^*}{4}, L - (n-1) \cdot \frac{\lambda^*}{4}, \ldots, L - \frac{\lambda^*}{4}, L, L + \frac{\lambda^*}{4}, \ldots,$$
$$\ldots, L + (n-1) \cdot \frac{\lambda^*}{4}, L + n \cdot \frac{\lambda^*}{4}, \ldots$$

where n is a natural number.

For these values of x, the intensity I of the infrared light at the exit of the interferometer is measured by an InGaAs photodiode

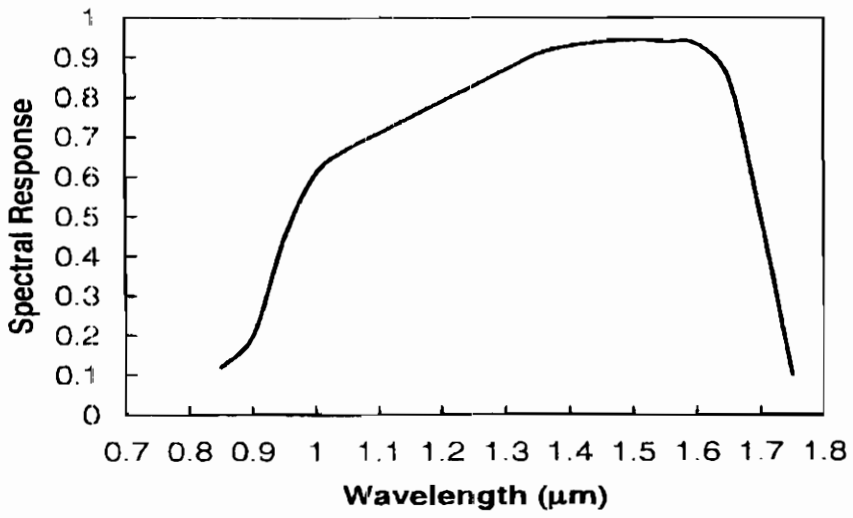

Figure 14: Spectral response of the InGaAs photodiode.

(G5832-05, EG&G). kept at room temperature. The diameter of the photodiode is 5 mm. Its spectral response is given in figure 14. In figure 15, we report the electronic configuration of the read out system. The photodiode is biased by means of a reverse voltage of +1.5 V and of a 10 MΩ resistance (nominal value). With this set up, the nominal dark current is of the order of 10 nA and the nominal capacitance is approximatelly 3.5 nF.

The output of the photodiode passes through a 4.7 nF capacitance (nominal value) and enters into a charge amplifier[20]. The integration factor of the charge amplifier is equal to 0.25 mV/fC and its decay constant is 400 μs. The charge amplifier is connected to a shaper amplifier (EG&G. Ortec 575A), whose shaping time is 3 μs. Its gain can be adjusted from 2 to 100. In figure 15 we show a typical signal obtained in correspondence of an electron bunch. This signal is sent to an electronic board (PAD82a, Bruker Optics) (hereafter called *mother-board*) installed into a personal computer and connected to the mirror-board. The mother-board performs

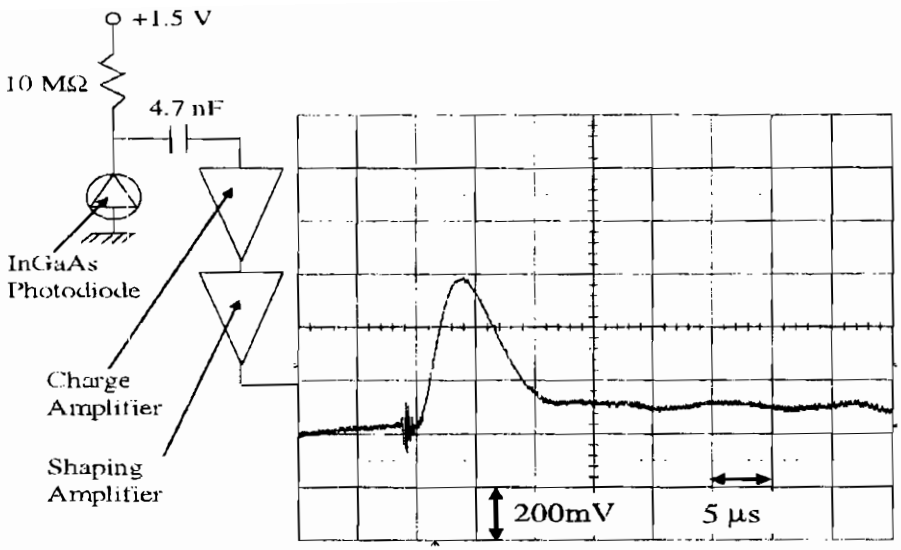

Figure 15: Scheme of the electronic read-out system of the InGaAs photodiode.

a fast analog-to-digital conversion of the signal and stores on the computer the value of x (sent by the mirror-board) and the digital value of $I(x)$[††].

For the measurement of the complete interferogram, we use the so-called *Step Scan Technique*. that proceeds according to the following scheme.

1. The mother-board orders the mirror-board to put the moving mirror in its innermost position $x = L - x_m$.

2. The electron gun shoots one electron bunch.

3. The mother-board performs the AD conversion of the signal coming from the infrared photodiode.

[††]The AD conversion is quite complicated. In this contest, however, we just underline that the digital number $I(x)$ is proportional to the maximum of the signal $I(t; x)$ reported in figure 15

4. Steps 2 and 3 are repeated for N_m times to increase the signal-to-noise ratio. N_m is given by the user before starting the spectrum measurement.

5. The mother-board stores on the computer x and the average of $I_1(x), \ldots . I_{N_m}(x)$.

6. The mother-board orders the mirror-board to put the moving mirror one step forward $x = x + s$, where s is a multiple of $\frac{\lambda^*}{4}$ depending on the resolution and on the spectral range required by the user. The better the resolution required or the larger the spectral range spanned, the smaller is s.

7. Steps 2 to 6 are repeated until the moving mirror arrives to its outermost position $x = L + x_m$. For $x = L + x_m$, only steps 2 to 5 are repeated.

In this way, at the end of the acquisition, the user has a discrete interferogram:

$$I(L - x_m), I(L - x_m + s), \ldots, I(L), \ldots, I(L + x_m - s), I(L + x_m)$$

The choice of N_m, of the resolution and of the spectral range deserves a comment. In principle, the maximum resolution is 0.1 cm^{-1} and the spectral range is between 5000 cm^{-1} and 15000 cm^{-1}. In this case, even with $N_m = 1$, the acquisition of the spectrum would take several hours because the number of steps is equal to $N_{step} = 568000$. This is not realistic not only for practical reasons, but also for technical problems. If the acquisition is too long, in fact, long term instabilities of the electron beam intensity introduce a fluctuation of the infrared signal amplitude not connected to the interferogram features. Usually, a compromise is reached for $N_m \simeq 50$ and $N_{step} \simeq 568$. For these values, one obtains a low noise spectrum in ten minutes. For $N_{step} = 568$ and spectral range between 5000 cm^{-1} and 15000 cm^{-1}, the resolution is 100 cm^{-1}. Without changing N_m and N_{step}, hence without increasing

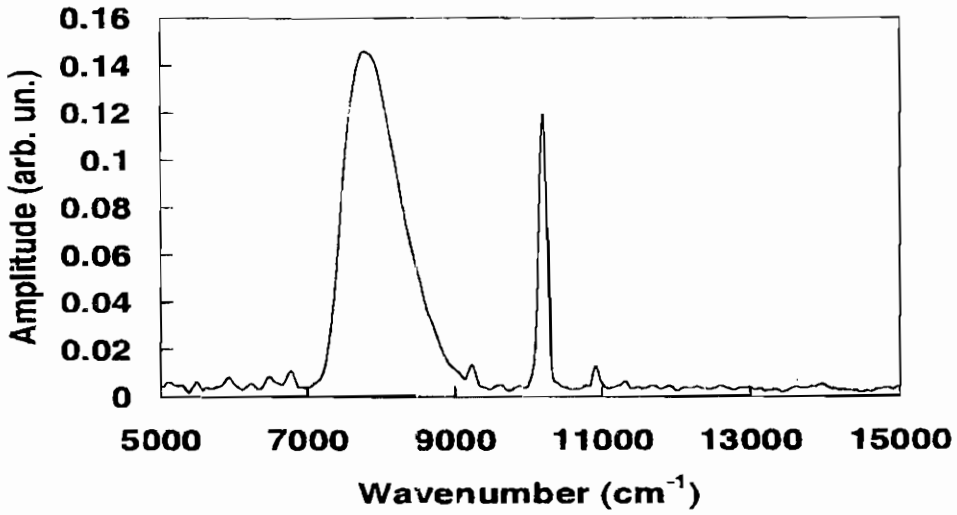

Figure 16: Fluorescent spectrum in Ar-Xe mixture excited by the electron beam.

the measuring time, better resolutions can be achieved in a spectral region of interest by reducing the spectral range.

The deconvolution of the interferogram to the spectrum is performed by a commercial software (Opus 3.3). A typical spectrum of an Argon-Xenon mixture is shown in figure 16. The spectra can be fitted with a Gaussian or a Lorentzian curve plus a baseline by means of the same commercial software, that uses the Levenberg-Marquardt algorithm for the minimization of the χ^2 estimator[21]. However, this program does not calculate the error on the fitting parameters. In the next chapter we describe what we have done in order to give an error estimate.

3 Calibrations and Tests

The experimental apparatus has been tested with infrared scintillating crystals. We have irradiated a Al_2O_3(Ti) crystal, a YAG(Nd)

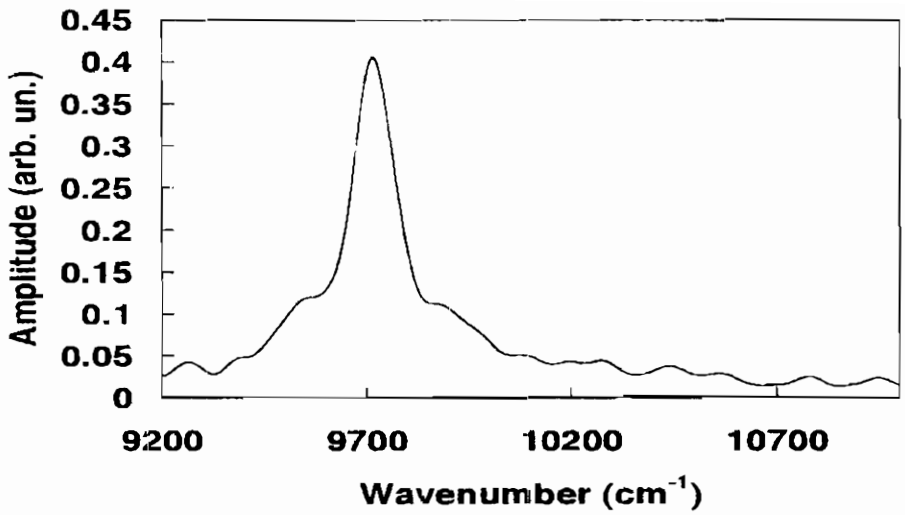

Figure 17: Fluorescent spectrum of YAG(Yb) excited by the electron beam.

and a YAG(Yb) crystal in this experimental set-up, and their well-known laser emission spectrum has been obtained. In figure 17 we report, by way of example, the result obtained with a YAG(Yb) sample.

We have also tested and extended the fitting software in order to give an error estimate. We have written a Fortran77 program that performs the fit with the same algorithm of Opus 3.3. A complete agreement of the results of the two programs has been obtained. But in the homemade program an algorithm has been developed with the aim to calculate the statistical errors on the fitting parameters. Since the standard deviation of each point of the spectrum is not known (because the commercial program does not estimate it during the Fourier Transform procedure), we used an unweighted algorithm[22, 23] that proceeds according to the following scheme:

1. The program minimizes, respect to the fitting parameters ξ_1,

$\ldots,\xi_m$, the unweighted χ^2 estimator, defined by:

$$\chi^2 = \sum_i \left(y_i - f(x_i;\xi_1,\ldots,\xi_m)\right)^2 \qquad (4)$$

where y_i are the experimental values of the spectrum in correspondance of the wavelength number x_i, and f is the fitting function. The minimizing procedure is performed according to the Levenberg-Marquardt algorithm*.

2. Once the program has found the minimizing parameters $\tilde{\xi}_1$, $\ldots,\tilde{\xi}_m$, it calculates the standard deviation (assumed to be the same for all the points of the spectrum) by means of:

$$\sigma = \sqrt{\frac{\sum_i \left(y_i - f(x_i;\tilde{\xi}_1,\ldots,\tilde{\xi}_m)\right)^2}{(N-m)}} \qquad (5)$$

where N is the number of the spectrum points.

3. Using this estimate for σ, the program calculates the covariance matrix in correspondance of $\tilde{\xi}_1,\ldots,\tilde{\xi}_m$.

The method is rigorously correct if two assumptions are satisfied: (i) the probability distribution of each spectrum point is Gaussian, and (ii) all the spectrum points have the same standard deviation. The first hypothesis is normally assumed by the users of the χ^2 estimator, but the second one is not always satisfied. However, we have no other means to estimate errors.

References

[1] G. Carugno, Nucl. Instr. and Meth. **A419** (1998) 617

[2] G. Bressi, G. Carugno, E. Conti, D. Iannuzzi, and A. T. Meneguzzo, Nucl. Instr. and Meth. **A440** (2000) 254

*Up to this point, the homemade program is equal to the commercial one

[3] S. Belogurov, G. Bressi, G. Carugno, E. Conti, D. Iannuzzi, and A. T. Meneguzzo, Nucl. Instr. and Meth. **A449** (2000) 254

[4] S. Belogurov, G. Bressi, G. Carugno, E. Conti, D. Iannuzzi, and A. T. Meneguzzo, Nucl. Instr. and Meth. **A452** (2000) 167

[5] S. Belogurov, G. Bressi, G. Carugno, E. Conti, D. Iannuzzi, and A. T. Meneguzzo, Nucl. Instr. and Meth. **A452** (2000) 381

[6] G. Bressi, G. Carugno, E. Conti, D. Iannuzzi, and A. T. Meneguzzo, Phys. Lett. **A278** (2001) 280

[7] S. Belogurov, G. Bressi, G. Carugno, E. Conti, D. Iannuzzi, and A. T. Meneguzzo, IEEE Trans. Nucl. Sci., accepted for publication

[8] G. Bressi, G. Carugno, E. Conti, C. Del Noce, and D. Iannuzzi, Nucl. Instr. and Meth., accepted for publication

[9] G. Bressi, G. Carugno, E. Conti, C. Del Noce, and D. Iannuzzi, Nucl. Instr. and Meth., accepted for publication

[10] G. Bressi, G. Carugno, E. Conti, C. Del Noce, and D. Iannuzzi, Nucl. Instr. and Meth., accepted for publication

[11] A. F. Borghesani, G. Bressi, G. Carugno, E. Conti, and D. Iannuzzi, submitted to Chem. Phys. Lett.

[12] P. Lindblom, O. Solin, Nucl. Instr. and Meth. **A268** (1988) 204

[13] O. Solin, P. Lindblom, D. Kronman, U. Rosengard, K. Vuorinen, Nucl. Instr. and Meth. **A268** (1988) 209

[14] P. Lindblom, O. Solin, Nucl. Instr. and Meth. **A268** (1988) 215

[15] A.J.P.L.Policarpo, Phys. Scripta **23**, 539 (1981)

[16] M. Miyajima, S. Sasaki, E. Shibamura, Nucl. Instr. and Meth. **B63** (1992) 297

[17] *Excimer Lasers*, in *Topics in Applied Physics, vol. 30*, Ch. K. Rhodes Editor (Springer. Berlin, 1979)

[18] R. S. Mulliken, J. Chem. Phys. **52** (1970) 5170

[19] M. J. Berger. J. S. Coursey, and M. A. Zucker, NIST Physical Reference Data.

[20] C. Bacci *et al.*. CERN UA1, Technical Note, TN 86-112 (1986)

[21] W.H.Press, S.A.Teukolsky, W.T.Vetterling, and B.P.Flannery, *Numerical recipes. The art of scientific computing.* (Cambridge University Press, Cambridge, 1992)

[22] P. R. Bevington and D. K. Robinson, *Data reduction and error analysis for the physical sciences.* (McGraw-Hill, Boston, 1992)

[23] A. Rotondi. P. Pedroni, and A. Pievatolo, *Probabilità, Statistica e Simulazione* (Springer Verlag Italia, Milano, 2001)

Volume I - n. 1 4/3/1986	CINQUANTA ANNI DI INTERAZIONI DEBOLI: DALLA TEORIA DI FERMI ALLA SCOPERTA DEI BOSONI PESANTI - Marcello Conversi	pag. 1
Volume I - n. 2 1/7/1986	EFFECTS OF DIOXINS ON NATURE AND SOCIETY - Opening talk, Sergio P. Ratti	pag. 3
	DIOXIN IN MISSOURI - Armon F. Yanders	pag. 11
	DEMONSTRATION OF INNOVATIVE REMEDIAL ACTION TECHNOLOGIES AT UNITED STATES MILITARY DIOXIN CONTAMINATED SITES - Terry L. Stoddard	pag. 23
	TIMES BEACH DIOXIN RESEARCH FACITLY - Robert J. Schreiber	pag. 41
	E.P.A. RISK ASSESSMENT OF CHLORINATED DIBENZO-P-DIOXIN AND DIBENZOFURANS (CCDs/CDFs) - Donald G. Barnes, Patricia Roberts	pag. 51
	RECENT INTERNATIONAL COOPERATION IN EXCHANGE OF INFORMATION ON DIOXIN - Donald G. Barnes	pag. 63
	CHLORACNE AND THE AGENT ORAGE PROBLEM IN THE U.S.A. - B.Fischmann	pag. 69
Volume II - n. 1 15/9/1987	CONVEGNO SU "LA CONOSCENZA ATTUALE DELLA INTERAZIONE GRAVITAZIONALE" - MOTIVAZIONI DEL CONVEGNO - Sergio P. Ratti	pag. 3
	LA CONOSCENZA ATTUALE DELLA INTERAZIONE GRAVITAZIONALE: UN PROBLEMA APERTO - Sergio P. Ratti, Roberto Silvotti	pag. 5
	SVILUPPI RECENTI SULLA CONOSCENZA DELLA COSTANTE DI GRAVITAZIONE UNIVERSALE - Anna Grassi, Giuliano Strini	pag. 19
	LIMITI SPERIMENTALI SULLA MISURA DELL'ACCELERAZIONE DI GRAVITA' - Roberto Cassinis	pag. 31
	CONSEGUENZE SPERIMENTALI DELLA IPOTESI DI ESISTENZA DI UNA QUINTA INTERAZIONE - Fabrizio Massa	pag. 43
	VERIFICA DEL PRINCIPIO DI EQUIVALENZA E FORZE TRA PARTICELLE ELEMENTARI - Bruno Bertotti	pag. 81
Volume II - n. 2 10/12/1987	TRANSIZIONE LIQUIDO SOLIDO - Mario Tosi	pag. 3
	EQUAZIONI DI MAXWELL NEL VUOTO ED ELETTRODINAMICA QUANTISTICA - Emilio Zavattini	pag. 27
Volume III - n. 1 6/6/1988	METODI DI DILATAZIONE ANALITICA E RISONANZE IN SISTEMI QUANTISTICI NON RELATIVISTICI - Fausto Borgonovi	pag. 1
	CAMPO ELETTRICO ED EMISSIONI DA CARICHE IN UN MEZZO - Michele Spada	pag. 13
	SPETTROSCOPIA VIBRAZIONALE DI SUPERRETICOLI SEMICONDUTTORI - Luciano Colombo	pag. 29
	SOLITONI IN FISICA NUCLEARE - Marco Radici	pag. 51
	ASPETTI NON LOCALI DEL COMPORTAMENTO QUANTISTICO - Oreste Nicrosini	pag. 83
Volume III - n. 2 4/7/1988	CARATTERIZZAZIONE OTTICA IN SITU DI FILMS SOTTILI - Alessandra Piaggi	pag. 1
	TRANSIZIONI DI WETTING - Tommaso Bellini	pag. 23
	FORZE A TRE CORPI NEI GAS RARI - Silvia Celi	pag. 49
Volume III - n. 3 15/12/1988	FLAVOUR PHYSICS - Luciano Maiani	pag. 1
	THE STANDARD ELECTROWEAK MODEL: PRESENT EXPERIMENTAL STATUS - Pierre Darriulat	pag. 27
	WHY BE EVEN-HANDED? - Martin M. Block	pag. 47
Volume IV - n. 1 6/4/1989	LA FISICA DEI COLLIDER - Paolo Bagnaia, Fernanda Pastore	pag. 1
Volume IV - n. 2 15/6/1989	SOLAR WIND AND PHYSICS OF THE HELIOSPHERE - Bruno Coppi	pag. 2
	THE IGNITOR PROJECT - Bruno Coppi, Francesco Pegoraro	pag. 32
Volume IV - n. 3 15/9/1989	SPETTROSCOPIA ELLISSOMETRICA NEI SOLIDI - Alessandra Piaggi	pag. 3
	UNA INTRODUZIONE AL SUPERCONDUCTING SUPERCOLLIDER - R. Diaferia	pag. 23
	FENOMENI DI TRASPORTO IN SISTEMI HAMILTONIANI - Fausto Borgonovi	pag. 49
Volume V - n. 1 15/3/1990	MULTI-BODIED PHASE SPACE - A NEW APPROACH - Martin M. Bloch	pag. 1
	SCATTERING BRILLOUIN RISONANTE - Cristina Bosio	pag. 20
	METODO DI RINORMALIZZAZIONE PER LO STUDIO DELLA STRUTTURA ELETTRONICA DI SUPPERRETICOLI - Saverio Moroni	pag. 40
	MECCANISMI DI CONDUCIBILITA' IONICA MEDIATI DA DIFETTI ESTRINSECI - IL CASO DEL QUARZO - Alberto Paleari	pag. 57
	STATISTICHE QUANTISTICHE ED INDISTINGUIBILITA' - Gianluca Introzzi	pag. 69
Volume V - n. 2 15/6/1990	FISICA DELLE ALTE ENERGIE ALLE KOAN FACTORIES - Renato Diaferia	pag. 1
	NEUTRONI FREDDI E NEUTRONI ULTRAFREDDI - Gianluca Raselli	pag. 15
	TRANSIZIONI ORDINE-DISORDINE NELLE DISPERSIONI COLLOIDALI - Paolo Di Trapani	pag. 51

Volume VI - n. 1 p. I - 11/10/1991	LE UNITA' DI MISURA DELLA RADIOPROTEZIONE - Sergio P. Ratti	pag. 1
	L'INCIDENTE NUCLEARE DI CHERNOBYL - Giuseppe Belli	pag. 7
	NORMATIVA E PRINCIPI DI RADIOPROTEZIONE - Argeo Benco	pag. 17
	APPENDICE 1 - Pubblicazioni I.C.R.P. - Argeo Benco	pag. 56
	APPENDICE 2a) - Il regime giuridico dell'impiego pacifico dell'energia nucleare	pag. 59
	APPENDICE 2b) - Elenco di provvedimenti di interesse per le attività di impiego pacifico dell'energia nucleare e delle radiazioni ionizzanti	pag. 64
	APPENDICE 2c) - Raccolta di Circolari Ministeriali relative all'utilizzazione delle sostanze radioattive e delle macchine radiogene	pag. 78
	APPENDICE 2d) - Raccolta di Circolari Ministeriali relative al trasporto delle sostanze radioattive	pag. 85
	RADIOATTIVITA' AMBIENTALE E RADIOECOLOGICA - Arrigo Cigna	pag. 87
	EFFETTI BIOLOGICI DELLE RADIAZIONI IONIZZANTI - Marco Caprotti	pag. 107
Volume VI - n. 1 p. II - 11/10/1991	MODELLO PREVISIONALE DELLA CONCENTRAZIONE DI ^{90}Sr, ^{134}Cs E ^{137}CS NELLA CATENA ALIMENTARE - Arrigo Cigna	pag. 117
	L'AMBIENTE E LA RADIOPROTEZIONE IN RELAZIONE AD INCIDENTI NUCLEARI - Arrigo Cigna	pag. 131
	INCIDENTE NUCLEARE "CHERNOBYL" E SUE RIPERCUSSIONI SULLA CATENA ALIMENTARE - R. Cazzaniga, G. Dominici, A. Malvicini, E. Sangalli	pag. 157
	PRIMA VALUTAZIONE DELL'IMPATTO RADIOLOGICO AMBIENTALE NELLA ZONA DI ISPRA IN RELAZIONE ALL'INCIDENTE NUCLEARE DI CHERNOBYL - Argeo Benco	pag. 177
	APPROCCIO FRATTALE ALLA DESCRIZIONE DELLA RADIOATTIVITA' IN ARIA IN ITALIA DOPO CHERNOBYL - Gianfausto Salvadori	pag. 201
Volume VII - n. 1 15/3/1992	ELECTRON ENERGY LOSS SPECTROSCOPY - Marco Amiotti	pag. 1
	LIVELLI ELETTRONICI PROFONDI IN SEMICONDUTTORI E LORO CARATTERIZZAZIONE - Adele Sassella	pag. 35
	LA RICERCA DEL BOSONE DI HIGGS AI FUTURI ACCELERATORI - G.Montagna	pag. 57
	SIMMETRIA CHIRALE E TEOREMA DI GOLDBERGER-TREIMAN - Carlo Gobbi	pag. 81
Volume VII - n. 2 15/10/1992	CRESCITA, CARATTERIZZAZIONE ED APPLICAZIONI DEI LANGMUIR-BLODGETT FILMS - Marco Amiotti	pag. 1
	LA CATODOLUMINESCENZA - Vittorio Bellani	pag. 35
	CORRELAZIONI ELETTRONICHE IN OSSIDI DI METALLI DI TRANSIZIONE - Luigi Sangaletti	pag. 63
Volume VIII - n. 1 15/1/1993	TEORIA DELLE STRINGHE IN DIMENSIONE NON CRITICA- Alberto Vancheri	pag. 1
	ROTTURA ESPLICITA E SPONTANEA DI SIMMETRIE CONTINUE GLOBALI NEL MODELLO STANDARD - Antonio Defendi	pag. 25
	APPLICAZIONI DELLA μ^+SR NELLA STRUTTURA DELLA MATERIA - P.Carretta	pag. 39
	EFFETTI FOTORIFRATTIVI IN CRISTTALLI IONICI - Enrico Giulotto	pag. 75
Volume VIII - n. 2 15/4/1993	L'UNITA' DELLA SCIENZA. IL CASO DELLA FISICA, OGGI - G. Salvini	pag. 1
	APPLICAZIONI DELLA μ^+SR NELLA STRUTTURA DELLA MATERIA - P. Carretta	pag. 37
	MODELLO A TETRAEDRI PER LA FUNZIONE DIELETTRICA DI SOLIDI AMORFI - A. Sassella	pag. 73
	INTRODUZIONE ALLE RETI NEURALI - C Macchiavello	pag. 93
Volume VIII - n. 3 15/6/93	RPC: STATUS AND PERSPECTIVES - R. Santonico	pag. 1
	PERFORMANCE OF E771 RPC MUON DETECTOR - E. Gorini (E771 Coll.)	pag. 13
	THE MUON TRIGGER HODOSCOPE OF THE BEAUTY HADRO-PRODUCTION EXPERIMENT WA92; PERFORMANCES AND PRELIMINARY RESULTS ON BEUTY MUONIC DECAYS - G. Martellotti. D. Orestano (Beatrice Coll.)	pag. 29
	THE RPC TRIGGER SYSTEM FOR THE L3 FORWARD BACKWARD MUON DETECTOR - S. Patricelli	pag. 37
	RESULTS FROM THE RD5 EXPERIMENT AT CERN - A. Di Ciaccio (RD5 Coll.)	pag. 45
	LEVEL 1 MUON TRIGGER IN THE ATLAS EXPERIMENT AT THE LARGE HADRON COLLIDER - A. Nisati (ATLAS Coll.)	pag. 61
	RPC BASED MUON TRIGGER FOR THE CMS DETECTOR AT LHC - G. Wrochna (CMS Coll.)	pag. 73
	AN RPC MUON SYSTEM FOR SDC AT SSCL - G. Introzzi (Pavia SDC Group)	pag. 83
	A MUON TRIGGER FOR LHB - R. Santacesaria	pag. 103
	MINI: A HORIZONTAL MUON TELESCOPE IMPLEMENTED WITH RESISTIVE PLATE CHAMBERS - G. Iaselli	pag. 115
	T&T: A NEW DESIGN FOR A FRONT-END TIME DIGITIZER ELECTRONICS M. Ambrosio, G.C. Barbarino, A. Lauro, G. Osteria, G. Agnetta, O. Catalano, L. Scarsi, A. Lanza, G. Liguori, P. Torre	pag. 123
	ATMOSPHERIC AND ACCELERATOR NEUTRINO PHYSICS WITH RPCS IN THE SOUDAN 2 CAVERN - D.J.A. Cockeril.	pag. 133

	STUDY OF THE CHARACTERISTICS OF RESISTIVE PLATE CHAMBERS IN THE RD5 EXPERIMENT - L. Pontecorvo (RD5 Coll.)	pag. 145
	OPERATION OF RESISTIVE PLATE CHAMBERS WITH PURE CF_3BR - R. Cardarelli	pag. 159
	WLDC: A DRIFT CHAMBER WITH A PAD RPC FOR MUON DETECTION AT LHC H. Faissner, Th. Moers, R. Priem, B. Razen. D. Rein, H. Reithler, D. Samm, R. Schleichert, H. Schwarthoff, H. Tuchscherer, H. Wagner	pag. 167
	GLASS ELECTRODE SPARK COUNTER - G. Bencivenni, G. Felici, E. Iacuessa, C. Gustavino, M. D'Incecco	pag. 181
	RPC READOUT FOR PARTICLE ASTROPHYSICS - M. Bonori, U. Contino, F. Massa	pag. 193
	RESULTS OF TESTS OF PROTOTYPE RESISTIVE PLATE CHAMBERS - I. Crotty, J. Lamas Valverde, G. Laurenti, M.C.S. Williams, A. Zichichi	pag. 199
	GLASS ELECTRODES RPC: PERFORMANCE AND WORKING MODEL - M. Bonori, U. Contino, F. Massa	pag. 207
	FAST PARALLEL RPC READOUT SYSTEM - A. Lanza, G. Liguori, P. Torre, M. Ambrosio, G.C. Barbarino, M. Iacovacci, A. Lauro, G. Osteria, G. Agnetti, O. Catalano, L. Scarsi	pag. 219
	DATA ACQUISITION SYSTEMS DEVELOPED AT CAEN - F. Catarsi, C. Landi, G. Franchi, M. Lippi	pag. 225
Volume IX - n. 1 15/4/1994	RETICOLI DISORDINATI: IL MODELLO DI ANDERSON - R. Farchioni	pag. 1
	BREVE INTRODUZIONE ALLA TEORIA QUANTISTICA DELLA STIMA - M. Paris	pag. 23
	SUSY - M. Cacciari	pag. 36
	MASSE DEL QUARK TOP E DEL BOSONE DI HIGGS NEL MODELLO STANDARD - F. Piccinini	pag. 79
	DIELETTROFORESI: LIEVITAZIONE A CONTROLLO REAZIONATO - L. Laboranti	pag. 97
Volume IX - n. 2 15/11/94	PROPRIETÀ FISICHE DI CLUSTER METALLICI - V. Bellani	pag. 1
	APPLICAZIONI DI RETI NEURALI ALLA FISICA DELLE ALTE ENERGIE - P. Vitulo	pag. 18
	CRITTOGRAFIA QUANTISTICA - C. Macchiavello	pag. 47
	IL "PARADOSSO" DEI GEMELLI - M. Cacciari	pag. 64
	TRANSIZIONI DI FASE NEL PRIMO UNIVERSO - S. Rolli	pag. 77
	SULLA STABILITÀ DINAMICA DELLA BICICLETTA - M. Paris	pag. 102
Volume X - n. 1 15/3/95	FISICA DELLE INTERAZIONI FONDAMENTALI CON NEUTRONI FREDDI A. Guglielmi	pag. 1
	EFFETTO DELLA DISPERSIONE SPAZIALE SULL'ASSORBIMENTO ECCITONICO DEI CRISTALLI - G. Panzarini	pag. 79
	IL CAMPO ELETTRICO GENERATO DA UNA CARICA PUNTIFORME IN MOVIMENTO IN UN MEZZO ISOTROPO - U. Bellotti	pag. 105
Volume X - n. 2 15/6/95	SPETTROSCOPIA VIBRAZIONALE A RISOLUZIONE TEMPORALE - P. Calvi	pag. 1
	IL CONTROLLO DEI SISTEMI CAOTICI - M. Maris	pag. 25
	ASPETTI SPERIMENTALI DELLA FISICA DEI MESONI *B* A LEP - L. Viola	pag. 59
	AN INTRODUCTION TO THE PERTURBATIVE QCD POMERON AND TO JET PHYSICS AT LARGE RAPIDITIES - V. Del Duca	pag. 91
Volume X - n. 3 15/12/95	DIFFUSIONE DI LUCE DA SUPERFICI RUGOSE - M. Patrini	pag. 1
	PRINCIPI E APPLICAZIONI DELLE SPETTROSCOPIE A DIFFRAZIONE DI ELETTRONI - L. Rossi	pag. 25
	IONI DI TERRE RARE IN SEMICONDUTTORI - E. Pavarini	pag. 49
	PERDITA DI ENERGIA PER IONIZZAZIONE - P. Montagna	pag. 85
Volume XI - n. 1 15/6/96	TOPICS IN RESISTIVE PLATE CHAMBERS - R. Santonico	pag. 1
	THE AVALANCHE TO STREAMER TRANSITION IN RPC'S - R. Cardarelli, R. Santonico, V. Makeev	pag. 11
	A MODEL OF AVALANCHE TO STREAMER TRANSITION IN PPC/RPC DETECTORS - P. Fonte	pag. 25
	NEW DEVELOPMENTS OF RPC: SECONDARY ELECTRON EMISSION AND MICROSTRIP READOUT - E. Cerron Zeballos, I. Crotty, P. Fonte, D. Hatzifotiadou, J. Lamas Valverde, V. Peskov, M.C.S. Williams, A. Zichichi	pag. 45
	THE RPC SYSTEM FOR THE CMS EXPERIMENT AT LHC- G. Wrochna	pag. 63
	RPC TRIGGER DESIGN FOR THE FUTURE EXPERIMENT CMS - G. De Robertis, M. Gorski, M. Konecki, J. Krolikowski, I.M. Kudla, M. Lewandowski, F. Loddo, K. Pozniak, A. Ranieri, G. Wrochna	pag. 79
	THE LEVEL-1 MUON TRIGGER ALGORITHM OF THE ATLAS EXPERIMENT - A. Nisati	pag. 91
	RESISTIVE PLATE COUNTERS FOR THE BELLE DETECTOR AT KEKB - N. Morgan	pag. 101
	PRELIMINARY DESIGN OF THE BABAR DETECTOR FOR MUONS AND NEUTRAL HADRONS AT PEP II - N. Cavallo	pag. 115
	THE RPC FORWARD-BACKWARD TRIGGER SYSTEM OF THE L3 EXPERIMENT - P. Paolucci	pag. 129
	PERFORMANCES OF THE RPC TRIGGER SYSTEM IN THE L3	

	EXPERIMENT - R. De Asmundis	pag. 139
	USE OF RPC IN THE COVER PLASTEX EXPERIMENT - C. Agnetta, M. Ambrosio, C. Aramo, G.C. Barbarino, B. Biondo, O. Catalano, L. Colesanti, A. Erlykin, A. Lauro, A. Mangano	pag. 157
	A TEST OF THE ATLAS FIRST LEVEL MUON TRIGGER LOGIC - S. Veneziano	pag. 177
	CAEN ELECTRONICS FOR RESISTIVE PLATE CHAMBERS - A. Bigongiari, G. Franchi, G. Grieco, C. Landi, M. Lippi, F. Vivaldi	pag. 187
	TESTS OF RPC PROTOTYPES IN RD5 DURING 1994 RUNS - H. Czyrkowski, W. Dominik, J. Krolikowski, M. Lewandowski, Z. Mazur, M. Gorski, M. Szeptycka	pag. 197
	A TEST ON RESISTIVE PLATE CHAMBERS WITH NON OZONE DEPLETING FREON - M. Abbrescia, A. Colaleo, G. Iaselli, M. Maggi, B. Marangelli, S. Natali, S. Nuzzo, A. Ranieri, F. Romano, G. Gianini, G. Liguori, S.P. Ratti, P. Vitulo, M. Gorski	pag. 217
	STUDY OF ELECTRODE SURFACE TREATMENT EFFECTS ON BAKELITE RPC'S PERFORMANCES - M. Abbrescia, A. Colaleo, G. Iaselli, M. Maggi, B. Marangelli, S. Natali, S. Nuzzo, A. Ranieri, F. Romano, V. Arena, G. Boca, G. Bonomi, G. Gianini, G. Liguori, M. Marchesotti, M. Merlo, C. Riccardi, L. Viola, P. Vitulo	pag. 229
	RESISTIVE PLATE CHAMBER PERFORMANCES AT GREAT ALTITUDES - M. Abbrescia, E. Bisceglie, G. Iaselli, S. Natali, F. Romano	pag. 245
	EFFECTS INDUCED BY DIFFERENT KINDS OF FREON ON THE RPC CHARGE ACCUMULATION - V. Arena, G. Boca, G. Bonomi, G. Gianini, G. Liguori, C. Riccardi, L. Viola, P. Vitulo	pag. 255
	TEST OF LOW GAS GAIN RPCs WITH OZONE AND NON OZONE DEPLETING GAS MIXTURES - A. Di Ciaccio	pag. 263
	POSITION MEASUREMENT IN RPCs BY TOF - G.H. Grayer	pag. 273
	POSSIBLE USE OF RPCs IN THE MINOS EXPERIMENT - G.H. Grayer	pag. 279
	RESISTIVITY MEASUREMENTS ON RPC MATERIALS - G.H. Grayer	pag. 285
	WHAT HAVE WE LEARNED FROM A COMPARISON BETWEEN THE WIDE GAP AND NARROW GAP RESISTIVE PLATE CHAMBER - E. Cerron Zeballos, I. Crotty, D. Hatzifotiadou, J. Lamas Valverde, S. Neupane, V. Peskov, S. Singh, M.C.S. Williams, A. Zichichi	pag. 295
	LATEST RESULTS ON THE PERFORMANCE OF THE WIDE GAP RPC - E. Cerron Zeballos, I. Crotty, D. Hatzifotiadou, J. Lamas Valverde, S. Neupane, V. Peskov, S. Singh, M.C.S. Williams, A. Zichichi	pag. 317
	DEVELOPMENT OF RESISTIVE PLATE COUNTERS FOR THE PIERRE AUGER COSMIC RAY OBSERVATORY - P.O. Mazur	pag. 331
	THIN GAP CHAMBER: PERFORMANCE AS A TIME AND POSITION MEASURING DEVICE - Y. Ari, E. Barberio, T. Emura, J. Goldberg, K. Homma, M. Ikeno, M. Imori, K. Ishii, H. Ishiwaki, T. Kawamoto, T. Kobayashi, D. Lelloch, L. Levinson, N. Lupu, G. Mikenberg, M. Miyake, K. Nagai, T. Nagano, I. Nakamura, M. Nomachi, M. Nozaki, S. Odaka, T.K. Ohska, O. Sasaki, H. Shirasu, H. Takeda, T. Takeshida, S. Tanaka, C. Yokoyama	pag. 349
	RECENT STUDIES OF PARALLEL PLATE CHAMBERS FOR LHC EXPERIMENTS - A. Arefiev, G.L. Bencze, A. Bizzeti, E. Choumilov, C. Civinini, G. Dajkó, R. D'Alessandro, M.I. Josa, A. Malinin, M. Meschini, J. Molnár, V. Pojidaev, J.M. Salicio, F. Siklér, G. Vesztergombi	pag. 359
	ABS PLASTIC RPCs - E. Ables, R. Bionta, H. Olson, L. Ott, E. Parker, D. Wright, C. Wuest	pag. 373
	PERFORMANCES AND SIMULATION OF GLASS SPARK CHAMBERS - M. De Deo, M. D'Incecco, C. Gustavino, G. Bencivenni, G. Felici	pag. 387
	R&D OF GLASS RPCs FOR THE BELLE DETECTOR - Y. Teramoto, A. Yamaguchi and Y. Hoshi	pag. 401
	SOME RESULTS OF RESISTIVE PLATE COUNTER AND THE PROPOSAL TO TAU-CHARM FACTORY OF BEIJING - J.G. Bian, Y.B. Chen, H.G. Han, K.L. He, Y.Y. Jiang, X.L. Wang, Y.G. Xie, Y. Xu, C.S. Yang, G.A. Yang, Y. Yang, Z.T. Yu, J.Q. Zhang, Q.J. Zhang	pag. 419
	THE FOCUS EXPERIMENT RPC MUON IDENTIFICATION ARRAY - P.D. Sheldon	pag. 437
Volume XI - n. 2 15/7/96	ANTIGRAVITÀ E VIOLAZIONE DI CP - A. Filippi	pag. 1
	MICROCAVITÀ A SEMICONDUTTORE - R. Seno	pag. 19
	BANDE FOTONICHE E LA LOCALIZZAZIONE DELLA LUCE - R. Farchioni	pag. 59
	CORRELAZIONE DIPOLARE IN CATENE POLIMERICHE DI TIPO VINILICO - P. Montagna	pag. 83
	IL LASER AD ELETTRONI LIBERI E LE SUE APPLICAZIONI NELLA FISICA DELLO STATO SOLIDO - S. Bocelli	pag. 99
Volume XII - n. 1 15/6/97	IL CONTENUTO DI STRANEZZA DEL NUCLEONE - A. Filippi	pag. 1
	SEZIONE D'URTO DI BREMSSTRAHLUNG - B. Pasquini	pag. 33
	TECNICHE DI SVILUPPO IN 1/N PER SISTEMI ELETTRONICI FORTEMENTE CORRELATI - E. Pavarini	pag. 55
	GREGOR WENTZEL E I CAMMINI DI FEYNMAN - E. Lunati	pag. 1
	LA MICROSCOPIA A SCANSIONE A EFFETTO TUNNEL - P. Tognini	pag. 105

Volume XIII - n. 1	I BUCHI NERI: OSSERVAZIONE NEI SISTEMI STELLARI BINARI - G. Bonomi	pag. 1
15/4/98	SPETTROMETRIA DI MASSA A IONI SECONDARI - R. Rolli	pag. 17
	FUNZIONI DI STRUTTURA IN ELETTRODINAMICA QUANTISTICA - E. Poli	pag. 45
	CALORIMETRIA CON FIBRE AL QUARZO - N. Moggi	pag. 71
	LA FRIZIONE DINAMICA IN SCENARI DI INTERESSE ASTROFISICO - A. Pallavicini	pag. 93
Volume XIII - n. 2	IV International Workshop on : RESISTIVE PLATE CHAMBERS AND	pag. 1
15/5/98	RELATED DETECTORS - Sergio P. Ratti, Riccardo De Asmundis	pag.393
Volume XIV - n. 1	CORRELAZIONI NELLA PRODUZIONE MULTIPLA DI PARTICELLE	
15/5/99	A $\sqrt{s}$ = 630 E 1800 GeV - Niccolò Moggi	pag. 1
	FUNZIONI DI STRUTTURA IN QCD PERTURBATIVA – Fabrizio Gangemi	pag. 23
	I BUCHI NERI: OSSERVAZIONE NEI SISTEMI STELLARI BINARI - G. Bonomi	pag. 51
	QUANTIZZAZIONE BRS DELLE TEORIE DI GAUGE – Andrea Pallavicini	pag. 85
	CP VIOLATION IN THE Bo SECTOR – Amedeo Perazzo	pag. 101
Volume XV - n. 1	PROVE SPERIMENTALI DELLA QUANTIZZAZIONE DELLA CARICA	
15/10/00	ELETTRICA – D. Iannuzzi	pag. 1
	SURVIVAL PROBABILITY OF LARGE RAPIDITY GAPS IN $\bar{p}p$	
	COLLISION – M.M. Block, F. Halzen	pag. 35
	SPIN SUSCEPTIBILITY AND DIAMAGNETIC SUSCEPTIBILITY AT THE	
	SUPERCONDUCTING TRANSITION. EFFECTS OF MAGNETIC FIELD AND	
	DOPING-DEPENDENCE IN YBCO COMPOUNDS – A. Rigamonti, P. Tedesco	pag. 49
	RECENTI SVILUPPI SULLA REGOLA DI SOMMA	
	DI COULOMB NEI NUCLEI – A Meucci	pag. 87
Volume XVI - n. 1	MAGNETIC CORRELATIONS AND SPIN DYNAMICS IN PURE	
15/03/01	AND DOPED HALDANE CHAINS: ^{89}Y NMR IN $Y_{2-y}Ca_yBaNi_{1-x}Mg_xO_5$ – F. Tedoldi	pag. 1
	A FACILITY FOR THE STUDY OF PARTICLE-INDUCED	
	INFRARED EMISSION IN NOBLE GASES – D. Iannuzzi	pag. 93